

Electrical double layer interactions with surface charge heterogeneities

by
Christian Pick

A dissertation submitted to Johns Hopkins University in conformity with the requirements for the degree of Doctor of Philosophy

Baltimore, Maryland
October 2015

© 2015 Christian Pick
All rights reserved

Abstract

Particle deposition at solid-liquid interfaces is a critical process in a diverse number of technological systems. The surface forces governing particle deposition are typically treated within the framework of the well-known DLVO (Derjaguin-Landau-Verwey-Overbeek) theory. DLVO theory assumes of a uniform surface charge density but real surfaces often contain chemical heterogeneities that can introduce variations in surface charge density. While numerous studies have revealed a great deal on the role of charge heterogeneities in particle deposition, direct force measurement of heterogeneously charged surfaces has remained a largely unexplored area of research. Force measurements would allow for systematic investigation into the effects of charge heterogeneities on surface forces. A significant challenge with employing force measurements of heterogeneously charged surfaces is the size of the interaction area, referred to in literature as the electrostatic zone of influence. For microparticles, the size of the zone of influence is, at most, a few hundred nanometers across. Creating a surface with well-defined patterned heterogeneities within this area is out of reach of most conventional photolithographic techniques.

Here, we present a means of simultaneously scaling up the electrostatic zone of influence and performing direct force measurements with micropatterned heterogeneously charged surfaces by employing the surface forces apparatus (SFA). A technique is developed here based on the vapor deposition of an aminosilane (3-aminopropyltriethoxysilane, APTES) through elastomeric membranes to create surfaces for force measurement experiments. This vapor deposition technique produces surfaces

with well-defined micropatterned charge heterogeneities consisting of APTES monolayers on both flat and curved mica substrates. Characterization of these surfaces reveals highly charged APTES patches with minimal topographical variations. Force measurements between these micropatterned surfaces and mica results in interaction force profiles intermediate between mica-mica and APTES-mica. These force profiles are compared to a simple linear approximation for calculating forces with charge heterogeneities, expanded here to account for arbitrary charge heterogeneities. Our findings indicate a simple additive contribution between the APTES patches and surrounding mica to the measured force profile and suggest surface forces with charge heterogeneities can be predicted from a simple linear approximation based on the surface coverage of heterogeneities within the zone of influence.

Primary Advisor: Dr. Joelle Frechette (Associate Professor, Johns Hopkins University - Chemical and Biomolecular Engineering)

Reader 1: Dr. German Drazer (Associate Professor, Rutgers University - Mechanical and Aerospace Engineering)

Reader 2: Dr. Michael A. Bevan (Professor, Johns Hopkins University - Chemical and Biomolecular Engineering)

Acknowledgements

This thesis represents the culmination of many years of work that would not have been possible without my family. The support and encouragement of my father, Robert Pick, mother, Diana Pick, and my sister, Nicole Pick was my inspiration for completing this thesis. No words could truly express how grateful I am to my parents and sister and how much they mean to me. My grandfather Roy Kouns and grandmother Cleo Kouns were also an important part of my life. Sadly, both my grandparents passed away during my time at Johns Hopkins, but I'll never forget their words of encouragement and everything they taught me. I'm also extremely grateful for my friend David See. David is like a brother to me, and I'm truly lucky to have him as a friend.

I'd really like to thank my advisors Dr. Joelle Frechette and Dr. German Drazer for their valuable guidance in this very long process. I learned tremendously from them both during my time at Johns Hopkins and consider myself extremely fortunate to have had the opportunity to work with them. This thesis would have never come to fruition without their continued guidance, feedback, and encouragement.

I'd like to thank my thesis committee members: Dr. Michael Bevan, Dr. Howard Fairbrother, and Dr. Zachary Gagnon. Additionally, I'd like to thank Dr. Chao Wang and Dr. Patricia McGuiggan who were the alternates for my committee. I also appreciate Dr. McGuiggan's help with AFM imaging and her valuable feedback on my vapor deposition work.

I'd like to thank the following members of the Frechette Lab, both past and current: Dr. Rohini Gupta, Dr. David Broesch, Dr. Georgia Pilkington, Charles Dhong, Yumo Wang, Xiaoqing Hua, Dr. Mingxiang Luo, Dr. Gloria Olivier, Tianyu Yan, Brian Ryu, Sylvia Sohn, and Natasha Seelam. They have all been great colleagues and I consider myself extremely fortunate to have had the chance to work with them. Dave, Rohini, Charles, Georgia, Yumo, Xiaoqing, and Mingxiang in particular were extremely helpful throughout the struggles of research and I couldn't have done it without them

I'd like to thank the following undergraduate students for their help: Christopher Argento, Eric Ong, and Zachary Bentley.

I'd also like to thank Dr. Lise Dahuron. The time I spent as a teaching assistant for her ChemE Car class was enjoyable and as much of a learning experience for me as it was for the students. I'm also grateful for her words of encouragement during the course of my research.

Finally, I'd like to acknowledge Mr. Victor Martin. Victor used to work in Maryland Hall but passed away one month before the completion of my thesis. Victor always had great advice, and the stories he told about his days in the Army were a welcomed break from the struggles of research.

To my parents, Robert and Diana Pick, my sister Nicole, and my grandparents Roy and

Cleo Kouns

Table of Contents

Abstract	ii
Acknowledgements	iv
Table of Contents	vii
List of Tables	xi
List of Figures	xiii
Chapter 1 Introduction	1
1.1 Motivation.....	1
1.2 Thesis Overview	3
Chapter 2 Background	6
2.2 Electrostatic interactions	6
2.2.1 The origin of surface charge and the electrical double layer	6
2.2.2 The Poisson-Boltzmann Equation.....	9
2.2.2 Relating surface charge density and surface potential for an isolated surface.....	13
2.2.3 Interacting double layers.....	14
2.4 The Derjaguin Approximation.....	16
2.4 Calculating electrostatic interaction forces.....	19
2.3 Van der Waals Interactions.....	22
2.1 DLVO Theory.....	25
2.5 Non-DLVO forces	27
Chapter 3 Overview of Experimental Techniques	28

3.1 Surface Forces Apparatus (SFA)	28
3.2 Atomic Force Microscopy (AFM)	34
3.3 Fluorescence Microscopy	37
Chapter 4 Chemical vapor deposition of patterned aminosilane (APTES) monolayers.....	40
4.1 Introduction.....	40
4.2 Materials and Methods.....	44
4.2.1 Materials.	44
4.2.2 Fabrication.	44
4.2.3 Characterization.	47
4.3 Results and Discussion.	51
4.3.1 CVD deposition of patterned APTES monolayers.	51
4.3.2 Charge density of APTES monolayers.	63
4.4 Conclusions.....	69
Chapter 5 Estimating particle-patchy surface interactions for with variable boundary conditions	70
5.1 Introduction.....	70
5.2 Existing methods of calculating interactions with heterogeneous surfaces	73
5.2.1 Idealized model of a chemically heterogeneous surface.....	73
5.2.2 Review of the grid surface integration (GSI) technique	74
5.3.3 The electrostatic zone of influence (ZOI).....	78
5.3.3 Simplified method of predicting colloidal interactions: linear mixing approximation (LA).....	82
5.3.3 Homogeneous surface interactions	85
5.4 Results and discussion	87

5.4.1 Zone of influence modification for out-of-contact positions..	87
5.4.2 Linear mixing approximation versus GSI technique – many patches in the ZOI.....	91
5.4.3 Linear mixing approximation versus GSI technique – single patch in the ZOI	93
5.4.6 Transitioning from many patches in the ZOI to a single patch – effects of ionic strength.....	100
5.4.7 The effects of boundary conditions and variable surface potentials.....	104
5.4.8 Estimating critical patch coverage for arbitrary surface potential and boundary conditions	108
5.5 Conclusions.....	112
Chapter 6 Direct force measurement with patterned surface charge heterogeneities	116
6.1 Introduction.....	116
6.2 Materials and Methods.....	121
6.2.1 Materials	121
6.3 Results and Discussion	127
6.3.1 Homogeneous surface interactions	127
6.3.2 Single patch in the zone of influence	130
6.3.3 Many patches in the zone of influence	139
6.4 Conclusions.....	141
Chapter 7 Conclusions.....	144
7.1 Concluding remarks.....	144
7.2 Impact and Contributions.....	146
7.3 Future Directions	148
References	152

Appendix: Fabrication of elastomeric membranes.....	165
A.1 Overview of membrane fabrication	165
A.2 Template fabrication	166
A.2.1 Wafer preparation	167
A.2.2 SU-8 Spin-coating.....	167
A.2.3 Soft Bake.....	168
A.2.4 Exposure.....	168
A.2.5 Post-exposure Bake.....	169
A.2.6 Development	169
A.2.7 Hard bake	170
A.2.8 Mold Characterization.....	170
A.2.9 Mold release agent	172
A.3 Elastomeric membrane fabrication	172
A.3.1 Spin-coating PDMS elastomer.....	172
A.3.1 Curing membranes	174
A.3.2 Membranes extraction.....	175
Curriculum Vitæ.....	176

List of Tables

Table 4-1. Measured pattern dimensions from image analysis and comparison to predicted values.	59
Table 4-2 AFM height data for patterned surfaces.	62
Table 4-3 Fitted values for DLVO theory for the forces curves in Fig. 2 and Fig. 5. The expected Debye length at 10 ⁻⁴ M and 23°C = 30.6 nm.....	67
Table 5-1: Parameters for DLVO interaction energy estimates from Shen et al. ⁴⁴	94
Table 5-2: Critical patch coverage and single patch size estimates for particles of different radii and surface potentials ($\kappa^{-1} = 9.6$ nm, $\psi_{\text{Particle}} = \psi_{\text{Bulk}} = - \psi $, $\psi_{\text{Patch}} = \psi $) with CP and CC boundary conditions.....	112
Table 6-1 Fitted APTES and mica surface potentials, surface charge densities, and measured adhesive forces obtained from homogeneous surface interactions.	130
Table 6-2 Fits for an effective potential for the patterned surface for different boundary conditions ($\psi_{\text{mica}} = -120$ mV, $\kappa^{-1} = 31$ nm) Plots of fitted values shown in Fig. 6.2B. ..	133
Table 6-3 Measured average, maximum, and minimum patch coverage within ZOI from image analysis of figure 6.3D and corresponding calculated net surface potentials	135
Table A-1 Recommended SU-8 2025 spin-coating parameters for a final film thickness of 22 μm	168

Table A-2 Spin-coating parameters for a final elastomer film thickness of 20 μm with a membrane template dimensions 6.5x6.5 μm and micropillar height 22 μm 174

List of Figures

Figure 2.1. The electrical double layer showing the inner Helmholtz plane of adsorbed counter-ions and the outer Helmholtz plane (which corresponds to outer edge of the Stern layer). The diffuse layer extended beyond the outer Helmholtz plane. 8

Figure 2.2 Two charged flat surfaces (1 and 2) at separation, D where the position between the surfaces is equal to x . $x = 0$ at surface 1 and $x = D/2$ at the midplane halfway between the surfaces. ψ_1, ψ_2 are the surface potentials of surface 1 and 2. σ_1 and σ_2 are the surface charge densities..... 14

Figure 2.3. Electrostatic interaction force between a particle and a surface normalized by particle radius of curvature. The electrolyte solution is a 10^{-3} M 1:1 electrolyte solution. Particle and surface interaction plotted for 50mV (A, B) and 100mV(C, D) and symmetric surfaces (same potential) in A,C and asymmetric surfaces (opposite sign but same magnitude of surface potential (B, D). Solid black line represent numerical solution with constant charge boundary conditions, dashed black line represent numerical solution with constant potential boundary condition, and dotted green line is the result from HHF. 22

Figure 2.4 Illustration of pairwise molecular interaction assumption used in Hamaker theory. A single atom of surface 1 interacts with all the atoms of surface 2 across the intervening medium, 3. The separation between the surfaces is denoted as D . The sum of all the net pairwise interactions between the surfaces give the total van der Waals interaction. 24

Figure 2.5: Example plot of electrostatic (blue), van der Waal (red), and DLVO (black) energy as a function of separation. Positive values denote repulsive interactions and negative values denote attractive interactions..... 26

Figure 3.1. Illustration of a single silica support disk with a glued piece of mica. The backside of the mica is coated with 50nm of silver via thermal evaporation. 29

Figure 3.2. Illustration of internal mechanism of the SFA Mk II 30

Figure 3.3 Example of FECO for mica surfaces taken with a CCD camera. A) Two symmetrical mica surfaces immersed in aqueous solution. Line shows tip of parabolic fringes corresponding to point of closest approach (PCA) between the surfaces. Fringes appear as doublets because of birefringent properties of mica. B) Same mica surfaces as in A now in contact. Note flattening at the tip of the parabolic fringes. Additionally, the vertical lines are spectral emission lines from a mercury arc lamp (wavelengths: $\lambda = 546\text{nm}, 577\text{nm}, 579\text{nm}$) used to calibrate the image by converting pixel position into a wavelength from the fringes. 31

Figure 3.4 Example of motor calibration to calculate interaction force for SFA data. Points correspond to measured surface separation in SFA and line corresponds to motor calibration which provides the expected surface separation in the absense of any interaction force (zero force regime). Comparison of actual surface separation to expected separation with zero force allows calculation of the interaction force. 33

Figure 3.5 Basic components of an atomic force microscope. Sample is shown attached to piezo transducer. 35

Figure 3.6 Fluorescence microscope image of 110nm diameter fluorescent polystyrene nanoparticles deposited onto micropatterned aminosilane (3-aminopropyltriethoxysilane, APTES) patches on a mica surface. The diameter of the patches is 4.6 μm with a center-to-center separation of 12.5 μm . Scale bar = 50 μm 38

Figure 3.7 Basic components of an upright epi-fluorescence microscope 39

Figure 4.1 Bright-field optical microscope images of the PDMS membranes. 46

Figure 4.2 Diagram of patterning CVD steps. A) A plasma treated and hexane extracted PDMS membrane is placed on a mica surface (plasma treated side facing up). B) the mica surface is placed in a partially evacuated desiccator in the presence of an APTES drop and left to react for 4-12 hours. C) After the deposition, the membrane is lifted from the surface to yield (D) patterned areas of APTES monolayers. 52

Figure 4.3 Images of APTES patterned surfaces tagged with fluorescent carboxylic acid functionalized particles. The patterned PDMS membrane used as a blocking is A) without barrier layer, and B) with barrier layer generated with 1 min oxygen plasma. The scale bar is 100 μm 53

Figure 4.4 Dark-field optical microscope image of PDMS surfaces after different oxygen plasma treatment of increasing duration, A) No plasma, B) 0.5 minutes, C) 1 minute, and D) 2.5 minutes, showing cracks in the barrier layer. The conditions for the plasma treatment are 300 mTorr of oxygen at 50W and the scale bar is 100 microns. 54

Figure 4.5 Measured force (normalized by the radius of curvature) in 10^{-4} M HCl solution between two mica surfaces as a function of surface separation. Prior to force measurements the mica surfaces were in contact with PDMS sheets with APTES vapor present. The PDMS sheet was A) unextracted with a barrier layer generated on the bottom, and B) extracted membrane with a plasma-generated barrier layer on the top. Solid lines represent DLVO fits with constant charge boundary conditions and dashed lines represent constant potential boundary condition. 55

Figure 4.6 Force normalized by radius of curvature measured between two freshly cleaved mica surfaces in 10^{-3} M $KClO_4$, pH 4.98. Dashed Line – Constant potential boundary condition, solid line – constant charge boundary condition. The fitted Debye Length is 9.2 ± 0.8 nm and the fitted surface potential is -93 ± 4 mV. 57

Figure 4.7 Optical micrographs of APTES patterned mica tagged with fluorescent particles. The following APTES deposition concentrations were used: A) $0.25 \mu\text{L/L}$, B) $1.25 \mu\text{L/L}$, C) $5 \mu\text{L/L}$, D) $1.25 \mu\text{L/L}$ (curved surface, ~ 2 cm radius). Scale bar = $100 \mu\text{m}$. Dimensions of the patterned features are given in Table 4-1. 58

Figure 4.8 AFM height images of patterns deposited at different APTES concentrations A) $0.25 \mu\text{L/L}$ B) $1.25 \mu\text{L/L}$ C) $5 \mu\text{L/L}$ 62

Figure 4.9 AFM height image of mica surface patterned with an array of APTES monolayer patches. The height profile on the left shows the height of the condensation rings and is taken along the line labeled as (1) on the right panel. 63

Figure 4.10 Force curves, normalized by the radius of curvature, as a function of separation measured between (A-C) APTES-APTES (symmetric), and (D-F) APTES-mica (asymmetric) surfaces in 10^{-4} M HCl. Each plot show multiple approach/retraction curves, each indicated by different symbols. The APTES concentration during the deposition are (A,D) $5 \mu\text{L/L}$, (B,E) $1.25 \mu\text{L/L}$, (C,F) $0.25 \mu\text{L/L}$. Solid lines represent DLVO fits with constant charge boundary conditions and dashed lines represent constant potential boundary condition. The sign of ψ_{APTES} in (A-C) is determined from the force measurements in (D-F). 68

Figure 5.1: a) Diagram of patterned surface, highlighting patch diameter(d), center-to-center spacing (l), edge-to-edge spacing ($s=l-d$), and the lattice angle (θ) b) larger image showing a single unit cell of the pattern. Red circles represent patches and the white background represents the bulk surface..... 73

Figure 5.2: Illustration of the grid-surface integration technique showing a discrete particle element interacting with a collector surface element..... 76

Figure 5.3: Diagram showing the derivations of the radius of the electrostatic zone of influence for a.) a single Debye length intersecting the surface (ZOI-1) b.) the intersection of the debye lengths on the particle and surface (ZOI-2). $\kappa - 1$ is the Debye length and a is the particle radius..... 79

Figure 5.4: Figure showing two different zones of influence on patterned surfaces. Both surfaces have the same patch diameter to patch spacing ratio (d/l) and consequently the

same patch surface coverage. a) Zone of influence much larger than patch spacing b) zone of influence of approaching same size as patch spacing 82

Figure 5.5: Diagram showing the modifications of the radius of the ZOI for out of contact positions a) a single Debye length shell intersecting the surface (ZOI-1) b) the intersection of the debye lengths on the particle and surface (ZOI-2). $\kappa - 1$ is the Debye length, a is the particle radius, and D is the particle-surface separation. 90

Figure 5.6: a) Particle of radius a and separation D interacting with surface containing circular heterogeneities arranged in a square array ($d=10\text{nm}$, $l=20\text{nm}$; $f_p=f_{p,zoi}=19.6\%$) . Inset shows relative size of ZOI-1 for different particle radii ($a = 0.5$ and $1.0 \mu\text{m}$). b) Comparison of GSI technique results of Bendersky and Davis¹¹⁹ (points) to the linear approximation method (LA) with the Derjaguin approximation (lines). The patch (red) and bulk (blue) homogeneous interactions are also shown. Values used for calculation: $\kappa^{-1} = 5\text{nm}$, $\psi_{\text{patch}} = +50.8\text{mV}$, $\psi_{\text{bulk}} = \psi_{\text{particle}} = -25.4\text{mV}$, and $A_H = 5 \times 10^{-21}\text{J}$ 92

Figure 5.7: Illustration of particle of radius a interacting with surface bearing a square chemical heterogeneity of side length, l_{patch} . Particle is centered over heterogeneity at a separation, D 94

Figure 5.8: Comparison between the GSI results of Shen et al.⁴⁴ (points) with estimates from the linear mixing approximation method (lines) for a $0.5 \mu\text{m}$ radius particle at 1, 10, and 100mM (1:1) electrolyte solutions using the ZOI-1 argument. Values for the Hamaker constant and surface potentials are given in Table (5.1). The relative size of the ZOI is shown for each patch and ionic strength is shown in the bottom right. Values are

plotted for the different sizes of the square patch (given as side length by side length in nm) 97

Figure 5.9: Interaction with a circular patch of radius 16.93nm and 9 square patches (from Shen et al.⁴⁴, points) each 10x10nm compared the linear approximation (line) in 10mM solution with a particle of radius 0.5 μm . The circular patch and 9 patches have the same equivalent area and should have the same interaction with the approximation method. Note how the 9 patch case match the approximation exactly due the patchy surface being distributed throughout the ZOI. 98

Figure 5.10: Comparison between the GSI techniques (points) from published results⁴⁴ (points) with estimates from the linear mixing approximation (lines) for a 0.5 μm radius particle at 1, 10, and 100mM (1:1) electrolyte solutions using the ZOI-2 argument. Values for the Hamaker constant and surface potentials are given in Table (5-1). The relative size of the ZOI is shown for each patch and ionic strength. 99

Figure 5.11: a) ZOI-1 ($a=0.5 \mu\text{m}$, $\kappa^{-1} = 30.7\text{nm}$) on square array of patches ($d=60\text{nm}$, $l=120\text{nm}$; $f_p = 19.6\%$) with $\kappa^{-1} = 30.7\text{nm}$ b) ZOI-1 ($\kappa^{-1} = 3.0 \text{nm}$) on same array (Scale bars in A and B = 500nm) c) DLVO interaction energy profile for low ionic strength case in “5.11a” d) DLVO interaction energy for high ionic strength case in “5.11d”. Surface potentials values: $\psi_{\text{patch}} = +25.4\text{mV}$, $\psi_{\text{particle}} = \psi_{\text{bulk}} = -25.4\text{mV}$ 101

Figure 5.12: a) DLVO interaction force normalized by particle radius ($a=0.5 \mu\text{m}$) and b) DLVO interaction potential for constant charge (solid lines) and constant potential (dashed line) boundary conditions for homogeneous surfaces given as percent patch. 0%

(blue) corresponds to only bulk surface and 100% (red) corresponds to only patch surface. The HHF expressions are also shown as dotted black lines for comparison.

$\Psi_{\text{bulk}} = \Psi_{\text{particle}} = -50\text{mV}$, $\Psi_{\text{patch}} = +50\text{mV}$, $\kappa^{-1} = 9.6 \text{ nm}$, $A_H = 0.5 \times 10^{-20} \text{ J}$ 106

Figure 5.13: a) DLVO Interaction potential and b) force normalized by particle radius of curvature for constant charge (solid lines) and constant potential (dashed line) boundary conditions. A,B) 25% coverage, C,D) 50% coverage, E,F) 75% coverage $\Psi_{\text{bulk}} = \Psi_{\text{particle}} = -50\text{mV}$, $\Psi_{\text{patch}} = +50\text{mV}$, $\kappa^{-1} = 9.6 \text{ nm}$ $A_H = 0.5 \times 10^{-20} \text{ J}$ 107

Figure 5.14 A) critical patch coverage versus the magnitude of the surface potential (at infinite separation) for the constant charge and constant potential boundary conditions ($\Psi_{\text{bulk}} = \Psi_{\text{particle}} = -\Psi_{\text{patch}}$) ($a=0.5$, $\kappa^{-1} = 9.6 \text{ nm}$ $A_H = 0.5 \times 10^{-20} \text{ J}$) B) Critical single patch diameter versus the magnitude of the surface potentials 110

Figure 6.1 Comparison of zone of influence radius (r_{zoi}) to the radius of curvature of the surface/probes used in the SFA and colloidal probe techniques for three different Debye lengths ($\kappa^{-1} = 3\text{nm}$, 10nm , and 30nm). The dark highlighted regions show the corresponding radii of curvature for the SFA (1-2cm) and colloidal probe (1-10 μm) techniques. The resolution limit of i-line lithography (365nm) is highlighted showing the regions accessible to microfabrication of heterogeneously charged features. 119

Figure 6.2 Force normalized by radius of curvature for A) mica-mica surfaces B) APTES-mica C) APTES-APTES surfaces in a 10^{-4} M HCl solution. Solid lines show fit with constant charge boundary conditions and dashed lines shows fit with constant potential boundary conditions applied to both surfaces..... 129

Figure 6.3 A) Force normalized by radius of curvature of between a APTES patterned mica surface (APTES patches $26.9 \pm 1.1 \mu\text{m}$ diameter, $48.6 \pm 2.6 \mu\text{m}$ edge-to-edge spacing) and mica in 10^{-4} hydrochloric acid ($\kappa^{-1} = 31 \text{ nm}$) over multiple approaches, indicated by different symbols. Blue shows expected mica-mica interaction and red APTES-mica interaction B) Fit through points for a nominal surface potential of patterned surface with CC-CP, CC-CC, and CP-CP boundary conditions for the patterned and mica surface respectively, C) fit for effective patch coverage based on linear mixing approximation, $f_{p,zoi} = 26\%$) Fluorescence image of twin surface showing expected ZOI ($r_{zoi} = 35.2 \mu\text{m}$) randomly distributed over surface. The patch surface coverage is $f_p = 11.5 \pm 0.8\%$ for the entire surface from image analysis. Scale bar = $100 \mu\text{m}$ 131

Figure 6.4 A) Force normalized by radius of curvature between a mica surface and patterned surface of Fig. 6.2 at pH 9.1. Black line is fitted force profile with $\kappa^{-1} = 18.6 \text{ nm}$ and $\Psi_{\text{patterns}} = -103 \text{ mV}$ with constant potential boundary conditions. B) Fluorescent image of tagged surface verifying APTES patch removal under alkaline conditions, Scale bar = $100 \mu\text{m}$ 138

Figure 6.5 A) Force normalized by radius of curvature for a mica surface interacting with small patterns in 10^{-4} M hydrochloric acid solution at two different locations (solid and empty symbols). Blue line shows mica-mica interaction, red shows APTES-mica, and black shows fit based on linear mixing approximation with $f_{p,zoi} = 66\%$ (based on fit for both locations) B) Surface tagged with fluorescent particles after SFA experiment ($f_p = 23.0 \pm 8.7 \%$ from image analysis), Scale bar = 100 microns , ZOI ($r_{zoi} = 35.2 \mu\text{m}$) shown as a circle above the scale bar. 140

Figure 7.1 40x12 μm array of 50nm high silver pillars on a curved mica surface (radius of curvature $\sim 2\text{cm}$) formed via thermal evaporation through an elastomeric membrane. Scale bar = 200 μm	150
Figure A.1 Elastomeric membrane with 10 μm through holes separated by 10 μm	165
Figure A.2 Overview of membrane fabrication procedure A) Micropillar template for membrane fabrication. Pillars are fabricated from SU-8 on a silicon wafer. B) Template coated with Sylgard 184 via spin-coating to form membranes. Sylgard 184 layer thinner than SU-8 pillar height C) Cured Sylgard 184 peeled from template forming elastomeric membrane with through-holes.	166
Figure A.3 Example micropillar arrays characterized by laser scanning microscope showing a 3D profile, binary image of the pillar dimensions, average pillar height, and pillar surface coverage.	171
Figure A.4 Laser microscope 3D profile images of the top-side of cured elastomeric membranes (6.5x6.5 μm) removed from mold A) Insufficient spin-coating parameters lead to film over holes. B) Sufficient spin-coating parameters showing though holes in membrane.....	173

Chapter 1 Introduction

1.1 Motivation

Particle deposition at solid-liquid interfaces is a fundamental process in many systems of technological importance. Perhaps the single most widespread example is colloidal transport through porous media, such as occurs in packed bed filtration^{1, 2, 3, 4, 5} or colloidal transport into groundwater reserves in the environment.^{6, 7, 8} Another common example is paints and coatings^{9, 10, 11}. Controlled particle deposition can also be exploited as a mechanism for “bottom-up” self-assembly.^{12, 13, 14, 15} For self-assembly processes, colloidal particles serve as the building blocks for a device by depositing on a surface containing well-defined patterns.^{14, 16, 17, 18} This can be accomplished by patterning surface domains where particle deposition is energetically favorable.^{14, 16, 19, 20, 21, 22, 23}

While particle deposition onto surfaces is fundamental to filtration, coating, and bottom-up colloidal assembly processes, in several systems particle deposition is undesirable and can present serious (and often costly)^{24, 25} consequences. In many industrial unit operations, particle deposition can lead to fouling of surfaces in process equipment, such as heat exchangers²⁴ and reverse osmosis membranes^{26, 27}, reducing equipment efficiency and potentially leading to complete failure. In microfluidics, unwanted particle deposition can lead to clogging of microchannels.²⁸ Surface fouling is also implicated as the primary cause of biosensor failure.²⁹

Whether particle deposition is a nuisance such as in surface fouling or the fundamental requirement in a process, a thorough understanding of colloidal interactions is necessary if one wishes to engineer systems dependent on particle deposition phenomena. Particle deposition onto a surface involves in interplay of both hydrodynamic and colloidal interaction forces.^{30, 31} Classically, colloidal interactions are described using the well-known DLVO theory (Derjaguin-Landau-Verwey-Overbeek).^{32, 33, 34} DLVO theory treats the net particle-surface interaction as arising from electrical double layer interactions and van der Waals (vdW) interactions.³⁵ DLVO theory has, without a doubt, proven itself time and again for predicting colloidal stability and deposition.³⁶ Yet, for all its success, there are many examples throughout literature of discrepancies of observed particle deposition rates compared to predictions based on DLVO theory^{10, 37, 38}. These discrepancies are often the result of applying DLVO theory in systems that violate one or more of the basic assumptions of DLVO theory, such as applying the theory to systems containing chemical heterogeneous surfaces where the surface charge density cannot be assumed to be uniform.^{37, 39} Such heterogeneities can cause variations in surface charge density and locally alter interaction forces between a particle and surface.^{19, 40} These charge heterogeneities introduce locally favorable regions for particle deposition on a surface that should otherwise be repulsive based on DLVO predictions from average surface properties.⁴¹ Further, surface charge heterogeneities can be intentionally introduced onto surfaces to facilitate controlled deposition of particles onto surfaces such as in bottom-up assembly processes.^{14, 16, 19, 20, 21, 22, 23}

Numerous investigations into the effects of charge heterogeneities on surface forces have been conducted based on computational methods^{39, 41, 42, 43, 44, 45} or experiments measuring particle deposition rates onto heterogeneously charged substrates in flow systems.^{16, 19, 20, 46, 47, 48, 49} However, investigations based on direct measurement of surface forces with heterogeneously charged surfaces has remained largely unexplored.^{41, 50} Such experiments would allow interrogation of the force-separation relationship between particle and a heterogeneously charged surface. Also, unlike particle deposition experiments, force measurement allows surface forces to be decoupled from hydrodynamic interactions and studied independently. Finally, if patterned heterogeneities are used force measurements provide a means to directly and systematically explore the effects of parameters such as the size and surface coverage of charge heterogeneity on surface forces.

1.2 Thesis Overview

This thesis summarizes a process for fabricating micropatterned heterogeneously charged surfaces and the experimental results from force measurement experiments with patterned charge heterogeneities in the surface forces apparatus (SFA). First, it will describe the technique developed to produce heterogeneous charged surfaces with minimal topographical variations tailored to match the requirements of the surface forces apparatus (SFA). Next, it will outline a simple method for estimating surface forces with heterogeneously charged surfaces and investigate the effects of boundary conditions on predicted interactions. Finally, it will present results from direct force measurement

experiments with micropatterned charge heterogeneities. The thesis chapters are organized as follows:

Chapter 2 is intended to provide a brief background on the electrical double layer and DLVO theory. It covers a derivation of the Poisson-Boltzmann equation, the Derjaguin approximation, and calculating electrostatic and van der Waals forces.

Chapter 3 will provide a brief overview of the primary experimental techniques used in this thesis. A review of the surface forces apparatus (SFA), atomic force microscopy (AFM) and fluorescence microscopy will be provided.

Chapter 4 (peer reviewed publication⁵¹, reprinted with permission) will discuss a method developed to generate high-quality micropatterned aminosilane (3-aminopropyltriethoxysilane, APTES) monolayers on both flat and curved mica substrates based on a chemical vapor deposition procedure through elastomeric membranes. In electrolyte solutions, these substrates create micropatterned heterogeneously charged surfaces. This chapter outlines the critical process parameters needed to generate monolayers with minimal topographical variation while leaving the surrounding mica surface free of residue. The surface potential of the APTES and mica substrates is characterized through direct force measurements in the SFA and compared to literature values from electrokinetic studies.

Chapter 5 presents a simple analytical method for estimating DLVO interaction potentials and forces for heterogeneously charged surfaces. This analytical method, referred to here as the linear mixing approximation, is based on previous work published

in literature on the grid-surface integration (GSI) method and expanded here to incorporate the effects of boundary conditions on electrostatic interactions for patchy heterogeneously charged surfaces.

Chapter 6 presents force measurements with patterned charge heterogeneities in the surface forces apparatus (SFA). The results of this chapter will be analyzed within the framework of linear mixing approximation outlined in chapter 5. It will be shown that for a heterogeneously charged surface, the net measured interaction falls between that of the heterogeneity and the surrounding bulk surface and a fractional patch coverage, as well as an effective surface potential can be calculated from the measured force profiles.

Chapter 7 summarizes the results of the thesis and my contributions to understanding the effects of charge heterogeneities on surface forces. It will also discuss future research directions that could be explored based on the work presented in this thesis.

Chapter 2 Background

Colloidal interactions are typically treated within the framework of DLVO theory^{32, 36, 37, 52}. DLVO theory assumes the net particle-particle or particle-surface interaction force or energy come from the superposition of two components: electrostatic interactions arising from electrical double layer overlap and van der Waals interactions^{32, 35, 52}. These contribution of these two components are assumed to act independently of each other and are calculated separately then added together to obtain the total net particle-particle or particle-surface interaction. The following chapter will provide a background on DLVO theory and the calculation of electrostatic and van der Waals interaction forces.

2.2 Electrostatic interactions

2.2.1 The origin of surface charge and the electrical double layer

Most interfaces in electrolyte solutions have a charge associated with them. This charge can arise from a few sources^{33, 34 52}:

- 1) Dissociation of ions from a surface into solution
- 2) Adsorption of ions from a solution onto a surface

Because the solid/liquid interface develops a surface charge, the distribution of ions in the electrolyte solution adjacent to the charge interface is altered. The ions in solution will reorient themselves in response to the surface charge present with co-ions (same sign as the surface) being repelled from the surface while counter-ions (opposite sign as the surface charge) are attracted to the interface. Simultaneously, these ions are still free to diffuse under thermal motion.³⁵ This arrangement of the charged surface and distribution of ions in the electrolyte solution set up a structure called the electrical double layer.

Several models exist for the structure of electrical double layer. An early, illustrative model for the electrical double layer is the Gouy-Chapman model.³⁴ In the Gouy-Chapman model of the double layer, the surface charge density is assumed to be uniform, which ignores the effects of discrete ion binding sites.³⁵ Further, the electrolyte is assumed to have a uniform electrical permittivity throughout and the ions in solution are assumed to be point charges that form a diffuse layer.³⁶

While the Gouy-Chapman model serves as the foundation for modeling the diffuse double layer and calculation of electrostatic interactions, some modifications to the model have been proposed to account for the finite size of ions adsorbed at the interface. Ions have a finite size and can only approach within an ionic radius of the surface. This region where the ions are adsorbed to the interface is known as the Stern layer.^{34, 52} (Figure 2.1) The Stern layer can be further divided into two regions known as the inner and outer Helmholtz planes. The inner Helmholtz plane represents the location of fully adsorbed ions bound to the surface. The outer Helmholtz plane corresponds to the location of fully hydrated ions associated with the surface. The outer Helmholtz plane

and the boundary of the Stern layer coincide.³⁴ The diffuse layer (described by the Gouy-Chapman model) lies outside the Stern layer.

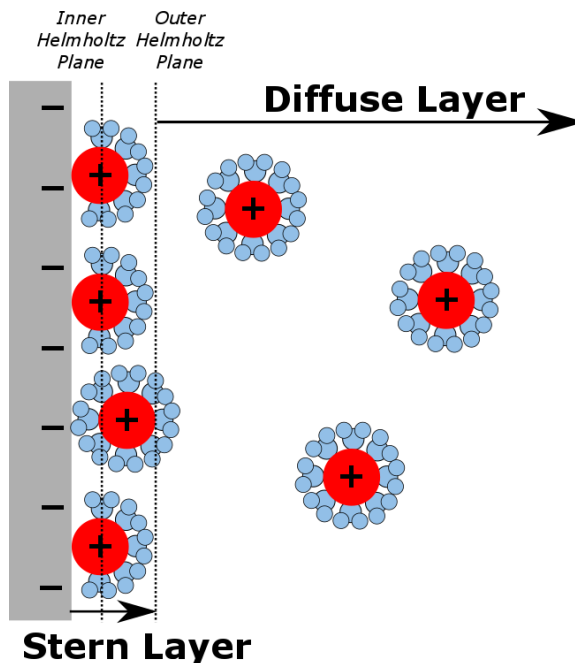


Figure 2.1. The electrical double layer showing the inner Helmholtz plane of adsorbed counter-ions and the outer Helmholtz plane (which corresponds to outer edge of the Stern layer). The diffuse layer extended beyond the outer Helmholtz plane.

For the purposes of analyzing electrostatic interactions in this chapter, the Gouy-Chapman model will be used where the charged surface is described by a single surface potential or surface charge density. The double layer consists of the plane of surface charge at the interface and the diffuse layer. Next, we derive an equation that described the electrical potential in the diffuse layer: the Poisson-Boltzmann Equation.

2.2.2 The Poisson-Boltzmann Equation

To describe the electrostatic double layer, we need to know the variation in the electrical potential away from the surface as a function of distance. This is obtained from solution of the Poisson-Boltzmann equation which relates the electrical potential at any point in the electrolyte to the concentration of ions at that point. Here we derive the Poisson-Boltzmann equation following along closely with the approach from Chapter 4 of Colloids and Interfaces with Surfactants and Polymers⁵². Deriving the Poisson-Boltzmann equation starts from Gauss' Law, which relates the divergence of the electric field at a point to the free charge density:

$$\nabla \cdot \vec{E} = \frac{\rho_f}{\varepsilon \varepsilon_0} \quad (2.1)$$

Where \vec{E} is the electric field, ρ_f is the free charge density, and ε is the dielectric constant of the medium and ε_0 is the permittivity of free space. Because the electric field is assumed to be constant with respect to time (an electrostatic field), which further implies the curl of the electric field is 0 ($\nabla \times \vec{E} = 0$), the electric field can be expressed as the gradient of the electrical potential ψ :

$$\vec{E} = -\nabla \psi \quad (2.2)$$

Substituting equation 2.2 into equation 2.1 yields:

$$\nabla \cdot (-\nabla\psi) = \frac{\rho_f}{\epsilon\epsilon_0} \quad (2.3)$$

Or:

$$\nabla^2\psi = -\frac{\rho_f}{\epsilon\epsilon_0} \quad (2.4)$$

Where $\nabla^2 = \partial^2/\partial x^2 + \partial^2/\partial y^2 + \partial^2/\partial z^2$ is the Laplace operator. Equation 2.4 is Poisson's equation and relates the gradient of the electrical potential to the free charge density at any point in the diffuse layer. The free charge density, ρ_f , comes from the ions in the diffuse layer. These ions are assumed to be described by a Boltzmann distribution:

$$n_i = n_{i0} \exp\left(\frac{-ze\psi}{kT}\right) \quad (2.5)$$

Where n_i is the number density of species i , n_{i0} is the number density of species i at location x where the potential, ψ , is assumed to be 0, z is the valence of species i , e is the elementary charge, k is the Boltzmann constant, and T is the temperature. The potential is assumed to be 0 far from the interface in the bulk electrolyte solution, therefore n_{i0} is the bulk concentration of species i in solution.

For a simple aqueous solution consisting of a symmetric electrolyte (where the valence, z , of cations and anions are of equal magnitude, such as in NaCl or KCl), the total free charge density is the sum of the number densities of the cationic and anionic species:

$$\rho_f = ze(n_+ - n_-) = -2zen_0 \sinh\left(\frac{ze\psi}{kT}\right) \quad (2.6)$$

n_0 is the number density of the bulk electrolyte. Substituting the free charge density (eqn. 2.6) into the Poisson equation (eqn. 2.5) yields the Poisson-Boltzmann equation for a symmetrical electrolyte:

$$\nabla^2 \psi = \frac{2ze n_0}{\epsilon \epsilon_0} \sinh\left(\frac{ze\psi}{kT}\right) \quad (2.7)$$

For a 1-D system, such as when the charged surface is an infinitely flat plate, we are only concerned with the variation of the potential normal to the surface (defined as the x direction). Therefore, eqn. 2.7 can be rewritten as⁵²:

$$\frac{d^2 \psi}{dx^2} = \frac{2ze n_0}{\epsilon \epsilon_0} \sinh\left(\frac{ze\psi(x)}{kT}\right) \quad (2.8)$$

Equation 2.8 can be rearranged to the following expression³⁴:

$$\frac{d^2 \left(\frac{ze\psi}{kT}\right)}{d(\kappa x)^2} = \sinh\left(\frac{ze\psi}{kT}\right) \quad (2.9)$$

Where κ is the Debye-Hückel parameter. The inverse of the Debye-Hückel parameter, κ^{-1} , has units of length and is known as the Debye length. The Debye length for a symmetrical electrolyte calculated as follows:

$$\kappa^{-1} = \sqrt{\frac{\epsilon\epsilon_0 kT}{2e^2 n_0 z^2}} \quad (2.10)$$

The Debye length is a decay length of the diffuse double layer and represents the characteristic length scale for double layer interactions. For a 1:1 electrolyte under standard conditions (T=20°C), the Debye length is equal to 3nm for a 10mM solution and 30.7nm for a 0.1mM solution.

The Poisson-Boltzmann equation is a non-linear second order differential equation and can only be solved analytically for the case of a single isolated flat interface in a symmetrical (z:z) electrolyte.⁵³ The analytical solution for a single isolated interface is⁵²:

$$\psi(x) = \frac{2kT}{ze} \ln \left[\frac{1 + e^{(-\kappa x)} \tanh\left(\frac{ze\psi_s}{4kT}\right)}{1 - e^{(-\kappa x)} \tanh\left(\frac{ze\psi_s}{4kT}\right)} \right] \quad (2.11)$$

Where ψ_s is the potential at the surface where $x = 0$. For values of the low surface potentials ($|\psi_s| < 25\text{mV}$), the electrical potential away from the surface can be approximated as⁵²:

$$\psi(x) \cong \psi_s e^{(-\kappa x)} \quad (2.12)$$

Eqn. 2.12 comes from solution of the *linearized* Poisson-Boltzmann equation. The Poisson-Boltzmann equation is linearized by assuming $\sinh\left(\frac{ze\Psi}{kT}\right) \sim \frac{ze\Psi}{kT}$. This approximation is known as the Debye-Hückel approximation.⁵²

2.2.2 Relating surface charge density and surface potential for an isolated surface

The surface charge density, σ_s , of an interface is related to the surface potential, ψ_s , by recognizing that electroneutrality must be maintained for the entire solid-liquid interface system. In other words, the total free charge in the diffuse layer must match the surface charge present on the surface³⁴:

$$\sigma_s = - \int_0^{\infty} \rho_f dx \quad (2.13)$$

The free charge density comes from eqn. 2.6 Performing this integration leads a relation between the surface charge density and surface potential. For a 1-1 electrolyte, the solution is known as the Grahame equation³³:

$$\sigma_s = \sqrt{8n_0 \epsilon \epsilon_0 k_B T} \sinh\left(\frac{e\psi_s}{2k_B T}\right) \quad (2.14)$$

For small surface potential values ($|\psi_s| < 25\text{mV}$) the surface charge density can be related to the surface potential through the following expression³⁴:

$$\sigma_s = \kappa \epsilon \epsilon_0 \psi_s \quad (2.15)$$

2.2.3 Interacting double layers

For problems involving particle-particle or particle-surface interactions, the electrical double layers of both particles or the particle and surface overlap upon approach. This overlap of double layers leads to a pressure, Π , in the gap between the two approaching surfaces³².

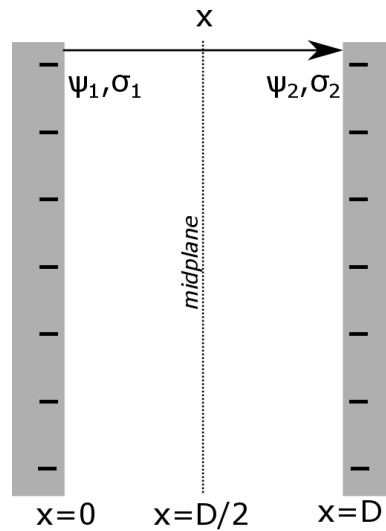


Figure 2.2 Two charged flat surfaces (1 and 2) at separation, D where the position between the surfaces is equal to x . $x = 0$ at surface 1 and $x = D/2$ at the midplane half-way between the surfaces. ψ_1 , ψ_2 are the surface potentials of surface 1 and 2. σ_1 and σ_2 are the surface charge densities.

Consider two flat plates, as shown in Figure 2.2. The net interaction energy per unit area due to double layer overlap can be obtained from integrating the gap pressure from when the surfaces are at infinite separation (i.e. sufficiently far so that double layer overlap is negligible) to a finite separation distance, D ³⁴:

$$U_{\text{edl}}(D) = \int_{\infty}^D \Pi(D') dD' \quad (2.16)$$

Eqn. 2.16 is essentially just the work required (per unit area) to bring the surfaces to their final separation distance D . The pressure at any location in the gap between the surfaces can be calculated from the following expression³²:

$$\Pi = 2n_b kT \left[\cosh\left(\frac{ze\psi(x)}{kT}\right) - 1 \right] - \frac{\epsilon_0 \epsilon_r}{2} \left(\frac{d\psi(x)}{dx} \right)^2 \quad (2.17)$$

The value of the potential, $\psi(x)$, comes from solving the Poisson-Boltzmann equation using appropriate boundary conditions to describe each surfaces. Two different boundary conditions are typically assumed: the constant potential (CP) boundary condition and the constant charge (CC) boundary condition⁵². When the constant potential boundary condition is used, the surface potentials of each surface (ψ_1, ψ_2) are assumed to remain constant as the two approach. When the constant charge boundary condition is used, the surface charge density of each surface (σ_1 and σ_2) is assumed to be constant as the surfaces approach each other.

The expressions thus far for the electrostatic interaction energy and gap pressure are for infinite flat plates. For particles with a large radius of curvature compared to the separation distance between them (or between a particle and a surface), the Derjaguin approximation can be used to relate flat plate interaction energies into forces.

2.4 The Derjaguin Approximation

The gap pressure in equation 2.17 and the electrostatic interaction energy in equation 2.16 as a consequence are for two infinite flat plates and flat plate interaction energy is per unit area. However, for particle deposition problems we are interested instead in obtaining the interaction between a sphere and a plane. The Derjaguin Approximation provides a method to relate the interaction energy per unit area between two flat plates to the interaction force between two spheres.³³ A sphere-plate interaction can be treated as a special case of the interaction between two spheres where the limit of one of the spherical radii is allowed to approach infinity.

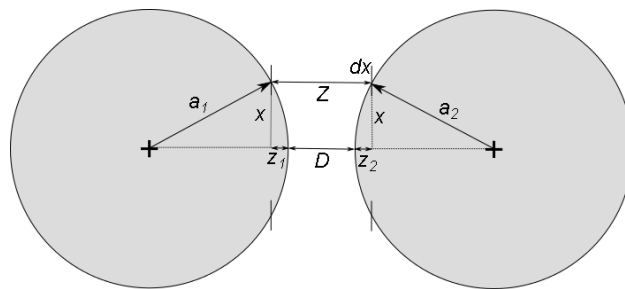


Figure 2.2 The Derjaguin Approximation relates flat plate interaction energy per unit area to the force of interaction between two spheres.

Following along closely with the derivation found in chapter 11 of Intermolecular and Surface Forces³³, consider two spheres of radii a_1 and a_2 with a separation D , as shown in Figure 2.2. Consider each sphere's surface as consisting of a series of concentric annular rings, each with radius x and a thickness dx . The separation between each ring is denoted as Z . The area of each of these concentric rings is $2\pi x dx$. The total force $F(D)$ on each sphere can be calculated by summing up the individual pairwise interaction forces $f(z)$ for each of these annular elements:

$$F(D) = \int_{Z=D}^{Z=\infty} 2\pi x dx f(z) \quad (2.18)$$

For a given separation D , Z is equal to the following:

$$Z = D + z_1 + z_2 = D + \frac{x^2}{2} \left(\frac{1}{a_1} + \frac{1}{a_2} \right) \quad (2.19)$$

And the derivative of Z is equal to:

$$dZ = \left(\frac{1}{a_1} + \frac{1}{a_2} \right) x dx \quad (2.20)$$

Equation 2.19 comes from applying the Chord Theorem³³, which states that $x^2 \sim 2a_1 z_1 = 2a_2 z_2$.

Substituting equations 2.19 and 2.20 into equation 2.18:

$$F(D) = 2\pi \left(\frac{a_1 a_2}{a_1 + a_2} \right) \int_{Z=D}^{Z=\infty} f(z) dZ \quad (2.21)$$

The integral on the right hand side of equation 2.21 is equal to the interaction energy per unit area for flat surfaces, thus:

$$\int_{Z=D}^{Z=\infty} f(z) dZ = U_{flats}(D) = \quad (2.22)$$

This implies that the interaction force between two spheres is:

$$F_{sphere-sphere}(D) = 2\pi \left(\frac{a_1 a_2}{a_1 + a_2} \right) U_{flats}(D) \quad (2.23)$$

The case of a single sphere of radius a interacting with a plate can be obtained by taking the limit as one sphere's radii goes to infinity:

$$F_{sphere-plate}(D) = 2\pi a U_{flats}(D) \quad (2.24)$$

Additionally, for two sphere of equal radii, a , equation 2.22 can be simplified to:

$$F_{sphere-sphere, equal radii}(D) = \pi a U_{flats}(D) \quad (2.25)$$

The Derjaguin approximation relates the interaction force between spheres or a sphere and a plate to flat plate interaction energies and can be used for different interaction forces such as electrostatic interactions or van der Waals interactions. However, the Derjaguin approximation is only valid in situations where the curvature of the spherical particle(s) is much larger than the interaction distances between them ($a/D \gg 1$). For electrostatic interactions, where the range of interactions is on the order of a Debye length, κ^{-1} , this would imply that ($a\kappa \gg 1$). In general, this condition is satisfied for micron scale particles but begins to break down for sub-micron particles.

2.4 Calculating electrostatic interaction forces

Equations 2.16 and 2.17 can be used together with the Derjaguin approximation to calculate the electrostatic force between a particle and surface. In general, to obtain the gap pressure, Π , from 2.17, numerical solutions must be used to solve the full Poisson-Boltzmann equation (equation 2.8) for the potential, $\psi(x)$. The potential must be solved at every surface separation distance, D . The two surfaces are assumed to obey either constant potential or constant charge boundary conditions. Once the potential is solved for, the gap pressure can be calculated. The pressure between the surfaces is equal at all points, x , so the gap pressure only needs to be solved for at one value of x . The midplane ($x = D/2$, see figure 2.2) is used here. A boundary value problem solver, such as the Matlab's `bvp5c` (used here) can solve the Poisson-Boltzmann equation with the appropriate boundary conditions. Once the pressure, Π , is known for all separations D , the pressure can be numerically integrated from equation 2.16 to obtain the flat plate

electrostatic interaction energy per unit area. This flat plate interaction energy can be used with the Derjaguin approximation for a sphere and a plate (equation 2.24) to obtain the electrostatic interaction force for a spherical particle and a surface.

Analytical approximations for the electrostatic interaction

Several approximate analytical expressions exist to calculate the electrostatic interaction force that avoid the need for solving the Poisson-Boltzmann equation numerically.^{33, 34} One widely used expression is that derived by Hogg, Healy, and Fusternau⁵⁴ (known as the Hogg-Healy-Fusternau or HHF expression). The HHF expression invokes the Debye-Hückel approximation to linearize the Poisson-Boltzmann equation and assumes constant potential boundary conditions. The flat plate interaction energy from the HHF expression is in a 1:1 electrolyte is³³:

$$U_{flats}(D) = \frac{\varepsilon\varepsilon_0\kappa[2\psi_1\psi_2 - (\psi_1^2 + \psi_2^2)e^{-\kappa D}]}{(e^{\kappa D} - e^{-\kappa D})} \quad (2.26)$$

Where κ is the Debye- Hückel parameter, ψ_1 and ψ_2 are the surface potential each of the surfaces, ε is the dielectric constant, ε_0 is the permittivity of free space, and D is the separation. Because the HHF expression is based on the Debye- Hückel approximation, it should only be applied to surfaces of low potential ($|\psi| < 25\text{mV}$). However, it has been found to agree reasonably well with numerical solutions up to about 50-60mV.⁵⁴

Figure 2.3 shows an example calculation of the electrostatic interaction forces for a particle interacting with a surface in a 10^{-3} M 1:1 electrolyte solution ($\kappa^{-1} = 9.6\text{nm}$ at

$T=22^{\circ}\text{C}$). The figure shows the electrostatic interaction for 4 separate combinations of surface potentials. Symmetric (A,C) denotes the particle and surface have identical surface potentials while asymmetric (B,D) denote that the particle and surface have surface potentials of the same magnitude but opposite sign. Figure 2.3 shows the results from numerical solutions using the constant charge (CC) and constant potential (CP) boundary conditions applied to the surfaces. For constant charge boundary conditions, the surface potential denotes the potential of the surface when they are far apart. Additionally, the results from the HHF expression are shown for comparison. At 50mV (A, B), the HHF results match the numerical solution with constant potential boundary conditions. However, this agreement breaks down at 100mV (C, D), due to the HHF expressions derivation using the Debye-Hückel approximation to derive the HHF expression.

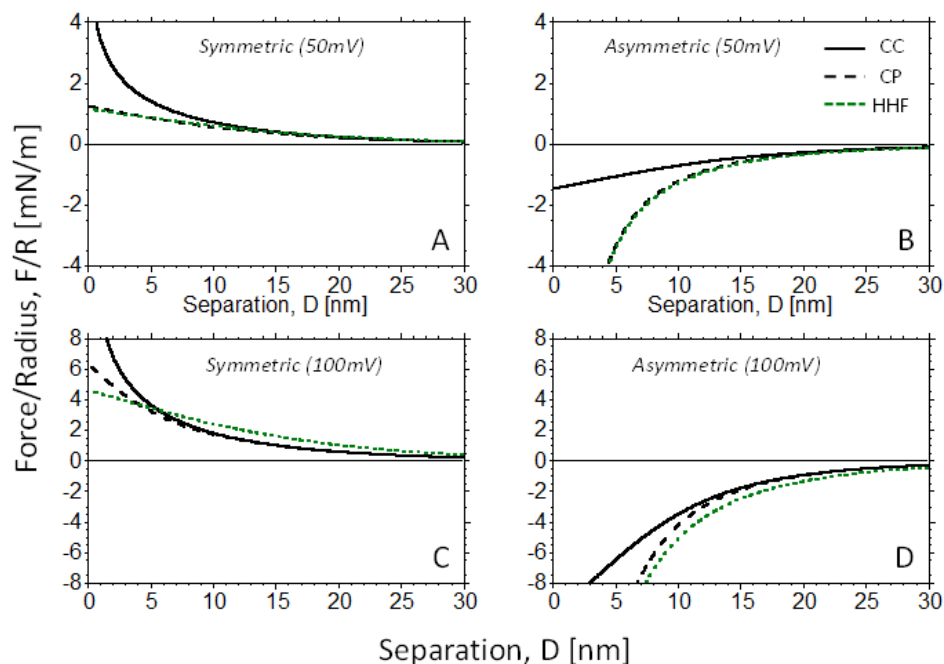


Figure 2.3. Electrostatic interaction force between a particle and a surface normalized by particle radius of curvature. The electrolyte solution is a 10^{-3} M 1:1 electrolyte solution. Particle and surface interaction plotted for 50mV (A, B) and 100mV(C, D) and symmetric surfaces (same potential) in A,C and asymmetric surfaces (opposite sign but same magnitude of surface potential (B, D). Solid black line represent numerical solution with constant charge boundary conditions, dashed black line represent numerical solution with constant potential boundary condition, and dotted green line is the result from HHF.

2.3 Van der Waals Interactions

London-van der Waals forces are a greater class of intermolecular forces that include interactions between dipoles-dipoles (Keesom Interaction), dipole-induced dipole (Debye interaction), and induced dipole- induced dipole (London interaction) interactions.⁵² Perhaps the most well-known example of van der Waals forces is the adhesion of the geckos onto surfaces.⁵⁵ For most colloidal systems, van der Waals forces

are attractive between particles or a particle and a surface, although repulsive van der Waals interactions are possible in a few special circumstances.³³

Two different theoretical approaches for calculating van der Waals interactions between surfaces are available.³⁴ These are Hamaker Theory⁵⁶ and Lifshitz theory⁵⁷. In Hamaker theory, the pairwise interaction between individual molecules at each surface is calculated to obtain a total interaction. This is illustrated in figure 2.4. Hamaker theory ignores multi-body interactions (the effects neighboring molecules have on each other). Lifshitz theory corrects for this by adopting a continuum approach where van der Waals interactions are calculated on the basis of the macroscopic electromagnetic properties of the surfaces and the medium between them. However, it is often difficult to apply Lifshitz theory due to a limited amount of information available on the full dielectric properties of a material.³⁴ As a consequence, Hamaker theory is often used for particle-surface interaction calculations.

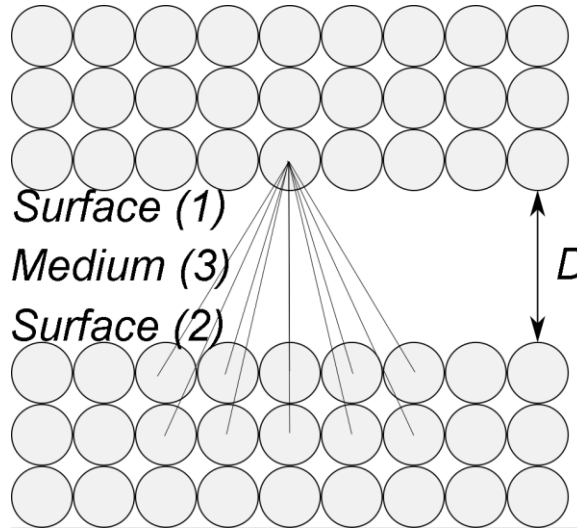


Figure 2.4 Illustration of pairwise molecular interaction assumption used in Hamaker theory. A single atom of surface 1 interacts with all the atoms of surface 2 across the intervening medium, 3. The separation between the surfaces is denoted as D . The sum of all the net pairwise interactions between the surfaces give the total van der Waals interaction.

The van der Waals interaction energy per unit area between two infinite flat surfaces can be calculated from the following equation:

$$U_{vdw,flats}(D) = -\frac{A_H}{12\pi D^2} \quad (2.27)$$

Where D is the surface separation and A_H is the Hamaker constant. The Hamaker constant is a material-dependent constant that depends on the surfaces and the medium between them. The Hamaker constant for most systems falls between 10^{-21} and 10^{-19} J.³⁴ Substituting equation 2.27 into the Derjaguin approximation (equation 2.24) provides the van der Waals interaction force between a sphere and a surface:

$$F_{vdw,sphere-plaene}(D) = -\frac{aA_H}{6D^2} \quad (2.28)$$

2.1 DLVO Theory

Derjaguin and Landau⁵⁸ and Verwey and Overbeek³⁵ independently developed a theory of colloidal stability based on the assumption that only electrostatic and van der Waals interaction contribute to colloidal interactions. This theory is known as DLVO (Derjaguin, Landau, Verwey, Overbeek) theory in honor of its founders. DLVO theory assumes that the net interaction energy for a system of two colloidal particles of a particle and a surface comes from the superposition of electrical double layer interactions and van der Waals interactions:

$$U_{DLVO}(D) = U_{edl}(D) + U_{vdW}(D) \quad (2.29)$$

Where $U_{DLVO}(D)$ is the DLVO potential energy as a function of either the particle-particle or particle-surface separation, D , $U_{edl}(D)$ is the electrostatic potential energy of interaction from electrical double layer overlap, and $U_{vdW}(D)$ is the van der Waals interaction energy. Figure 2.5 shows a plot of the electrostatic, van der Waals, and DLVO interaction energies (expressed in units of kT , the thermal energy of the system).

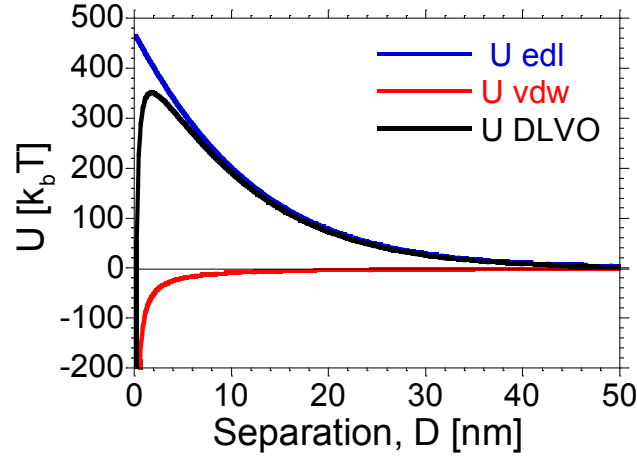


Figure 2.5: Example plot of electrostatic (blue), van der Waal (red), and DLVO (black) energy as a function of separation. Positive values denote repulsive interactions and negative values denote attractive interactions.

The DLVO interaction force can be obtained by recognizing $F = -dU/dD$.

$$F_{DLVO}(D) = F_{edl}(D) + F_{vdW}(D) \quad (2.30)$$

Where $F_{DLVO}(D)$ is the net DLVO interaction force, $F_{edl}(D)$ is the electrostatic force, and $F_{vdW}(D)$ is the van der Waals interaction force.

Particle stability (i.e. a particle’s “resistance” to aggregation with other particles or deposition onto a surface) is dependent upon the presence of a sufficiently large repulsive energy barrier. As shown in figure 2.1, the van der Waals energy is negative, indicating attractive interactions. Electrostatic forces are repulsive (positive interaction energies). The net interaction energy from DLVO theory is just the sum of these two interaction energies. At some small separation, the DLVO interaction energy changes from repulsive to attractive due van der Waals interactions at small separations. The

maximum repulsive DLVO energy is referred to as the energy barrier. In the example of figure 2.1, it is over $300kT$. A particle must have sufficient energy to overcome this energy barrier. Typically, an energy barrier of at least $10k_bT$ is considered sufficient to prevent particle deposition and aggregation.⁵⁹

2.5 Non-DLVO forces

DLVO theory has been extremely successful in describing colloidal interactions in several systems. However, there are systems where DLVO does not fully describe net particle-particle and particle-surface interactions due to additional contributions from sources not incorporated into DLVO theory.

Several forces not included in DLVO theory can arise in particle interactions. Such forces are often grouped together under the overall term non-DLVO forces.³⁶ Non-DLVO forces include steric forces due to the overlap of adsorbed polymer layers on surfaces, as well as hydration effects.³⁴ Hydration effects are the result of structural order of the solvent layer at a solid-liquid interface and generally produce an additional repulsion as the surfaces approach each other.

Often, these additional non-DLVO forces are added to DLVO theory to incorporate them into calculations of particle interactions.³⁶ This approach is sometimes referred to as “extended DLVO” or “xDLVO” in literature.^{44, 60}

Chapter 3 Overview of Experimental Techniques

The following chapter is intended to provide a brief overview of the three main experimental techniques used throughout this thesis. These techniques are the surface forces apparatus (SFA), atomic force microscopy (AFM), and fluorescence microscopy.

3.1 Surface Forces Apparatus (SFA)

The surface forces apparatus (SFA) is a direct force measurement technique capable of measuring a force between two surfaces as a function of separation with a force sensitivity of 10 nN and separation resolution of 0.1 nm.³³ The technique was developed by Tabor, Winterton, and Israelachvili for measurement of van der Waals forces between mica surfaces in air and vacuum.^{61, 62} Soon after, it was extended to work with liquids and used to measure double-layer forces in electrolyte solutions.⁶³ Since then, it has been used to study a wide range of forces such as hydrophobic interactions^{64, 65}, steric forces, hydrodynamic interactions^{66, 67}.

The substrates used for an SFA experiment consist of two mica surfaces arranged in a cross cylinder geometry. Mica is the ideal substrate for the SFA as it is optically transparent and can be cleaved into thin, molecularly smooth sheets and serves as the substrate of choice for nearly all SFA experiments. These mica surfaces are 2-5 microns thick and coated on one side with approximately 50nm of silver via either thermal evaporation or sputtering. Each mica surface is glued (silver side down) onto a fused

silica support disk that have a radius of curvature of 1-2 cm. Figure 3.1 shows an example of one of the disks with the glued and silvered mica substrate.



Figure 3.1. Illustration of a single silica support disk with a glued piece of mica. The backside of the mica is coated with 50nm of silver via thermal evaporation.

Inside the SFA, the surfaces are mounted opposed to one another in a crossed-cylinder configuration. This crossed-cylinder geometry is equivalent to a sphere interacting with a plane. One surface is fixed in place to a top mount and the other surface is mounted onto a leaf spring with a known spring constant. Figure 3.2 shows the mechanism of the Mk II SFA that was used in this thesis. The entire leaf spring assembly is movable and allows for control of the surfaces separation. The leaf spring assembly is movable via two independent microstepping drives. One microstepping drive (the upper drive in Figure 3.2) is rigidly attached to the mounted leaf-spring assembly and provides course movements for positioning the lower surface (mm to μm movements). Fine separation control is achieved through a system of two springs in connected in series: the helical spring and double cantilever spring. The leaf spring with mounted lower surface is connected directly to the double cantilever spring. This double cantilever spring has a very high spring constant, approximately 1000 times greater than the helical spring that

compresses it. The helical spring is connected directly to a shaft driven by a microstepper motor (lower drive in Fig 3.2). With this system, a small compression of the helical spring by the lower drive translates into an even smaller compression of the double cantilever spring (approximately 1000 times less). Because the lower surface (and the cantilever spring) are mounted directly on the double cantilever spring, this creates a small shift in the lower surface's position. In other words, a micron scale compression of the helical spring by the lower drive (driven by a microstepper motor) translates into a nanometer shift in the lower surface position.

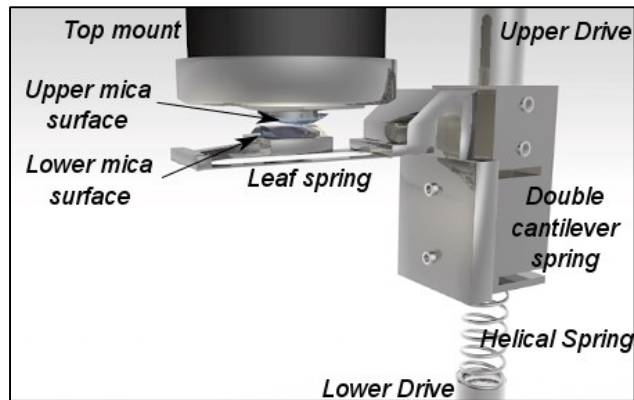


Figure 3.2. Illustration of internal mechanism of the SFA Mk II

One of the primary advantages to using the SFA for surface force measurement is that it provides data on absolute surface separations with sub-nanometer resolution. Because the mica pieces are silvered and optically transparent, they form an interferometer and multiple beam interferometry (MBI)⁶⁸ can be used to analyze the surface separation with angstrom-level precision⁶⁹. Light is conveyed from an external white light source through a window in the bottom of the SFA. This light is directed straight through the mica surfaces.

The silvered mica surfaces (and medium between them) form a three layer interferometer and only permit certain discrete wavelengths of light through them due to constructive and destructive interference.⁷⁰ These wavelengths form fringes of equal chromatic order (FECO)⁷⁰ that can be resolved with a spectrometer. An example of the FECO from an SFA experiment are shown in figure 3.3.

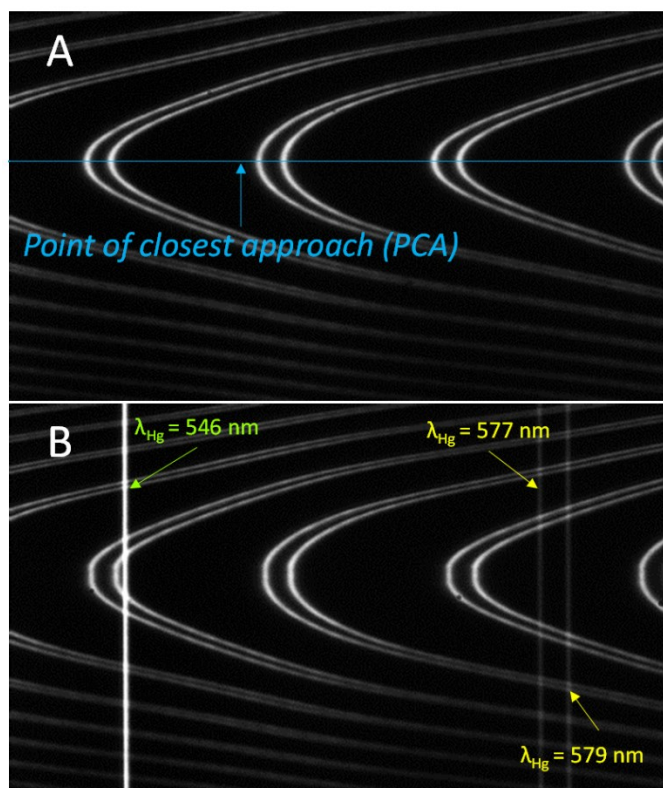


Figure 3.3 Example of FECO for mica surfaces taken with a CCD camera. A) Two symmetrical mica surfaces immersed in aqueous solution. Line shows tip of parabolic fringes corresponding to point of closest approach (PCA) between the surfaces. Fringes appear as doublets because of birefringent properties of mica. B) Same mica surfaces as in A now in contact. Note flattening at the tip of the parabolic fringes. Additionally, the vertical lines are spectral emission lines from a mercury arc lamp (wavelengths: $\lambda = 546\text{nm}$, 577nm , 579nm) used to calibrate the image by converting pixel position into a wavelength from the fringes.

The FECO appear parabolic in Fig. 3.3A because of the curvature of the mica surfaces and a slit in front of the spectrometer only allows a single cross-section of the surfaces to be viewed as a time. The tips of the parabolic fringes corresponds to the point of closest approach (PCA) between the surfaces. The wavelength of the FECO depend on the refractive index (n) of the surfaces and medium between them and the absolute surface separation (D). As the separation between the surfaces is changed, the FECO wavelengths will shift as well. Measuring the wavelengths of the FECO at the PCA allows for determination of the surface separation. Additionally, the radius of curvature (ROC) of the surfaces can also be obtained from analysis of the FECO. The lateral resolution is typically about $1\ \mu\text{m}$.

There is an analytical expression available to solve for the surface separation and refractive index for symmetrical three and five layer interferometers.^{70,71} For more complicated interferometers with asymmetric and several layers, the multi-layer matrix method can be is used to solve for the separation numerically. In this thesis, the fast spectral correlation algorithm developed by Heuberger⁷² is used to calculate the separation from the fringe positions. The algorithm was implemented in a LabVIEW script developed by Dr. Gloria Olivier (PhD 2010, Frechette lab) and further modified by Dr. Rohini Gupta (PhD 2013, Frechette lab).

The raw data obtained during an experiment is the absolute surface separation obtained from analyzing the FECO and the microstepping motor position (obtained from a rotary encoder attached to the motor). A motor calibration curve is fitted for each force measurement taken and along with the spring constant of the leaf spring, used to calculate

the interaction force between the surfaces. The motor calibration curve is obtained from a least squares fit of the motor position vs. separation data when the two surfaces are far enough apart that there is no interaction force between them. Under these conditions, there is a linear correlation between the movement of the microstepping motor and the change in separation of the surfaces (Fig. 3.4).

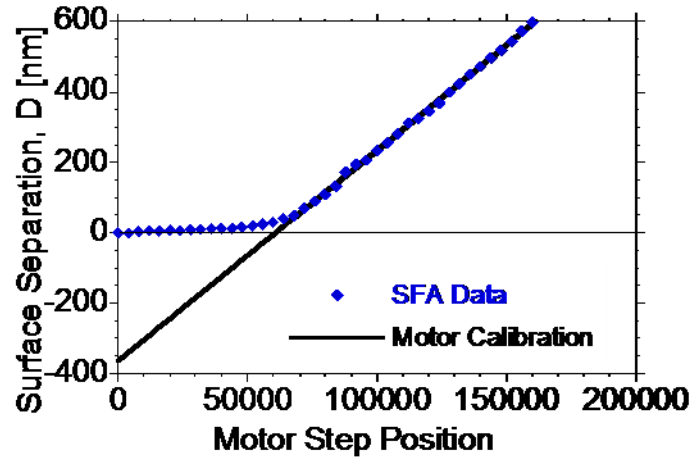


Figure 3.4 Example of motor calibration to calculate interaction force for SFA data. Points correspond to measured surface separation in SFA and line corresponds to motor calibration which provides the expected surface separation in the absence of any interaction force (zero force regime). Comparison of actual surface separation to expected separation with zero force allows calculation of the interaction force.

The interaction force (which is usually normalized by the radius of curvature of the surfaces) is obtained by taking the difference between the actual surface separation and the motor calibration, as shown in Eqn 3.1:

$$\frac{F}{R} = \frac{k_s}{ROC} (D_{SFA} - D_{F=0}) \quad (3.1)$$

Where k_s is the spring constant of the leaf spring, ROC is the geometrically averaged radius of curvature the surfaces ($ROC = \sqrt{R_1 R_2}$ where R_1 and R_2 are the radii of curvature of the upper and lower surfaces), D_{SFA} is the measured surface separation of the SFA data, and $D_{F=0}$ is the expected surface separation in the absence of any interaction forces between the surfaces and is obtained from a motor calibration. When F/R is positive, there is a net repulsive force between the surfaces (further apart than if there is no interaction force). When F/R is negative, there is a net attractive force (closer together than if there is no interaction force). For attractive forces, the interaction can only be measured as long as the gradient of the force does not exceed the spring constant, k_s , of the leaf spring. If the gradient of the forces is exceeded, a mechanical instability results and the surfaces will jump into contact.⁷³

3.2 Atomic Force Microscopy (AFM)

The atomic force microscope (AFM) is a versatile type of scanning probe microscope that has a wide number of uses from imaging surfaces to performing force measurements, such as in the colloidal probe technique. The AFM was used in this thesis as an imaging tool for characterizing the topography of micropatterned chemically heterogeneous surfaces. As such, the purpose of this section will be to provide a brief overview of the AFM as a surface imaging tool.

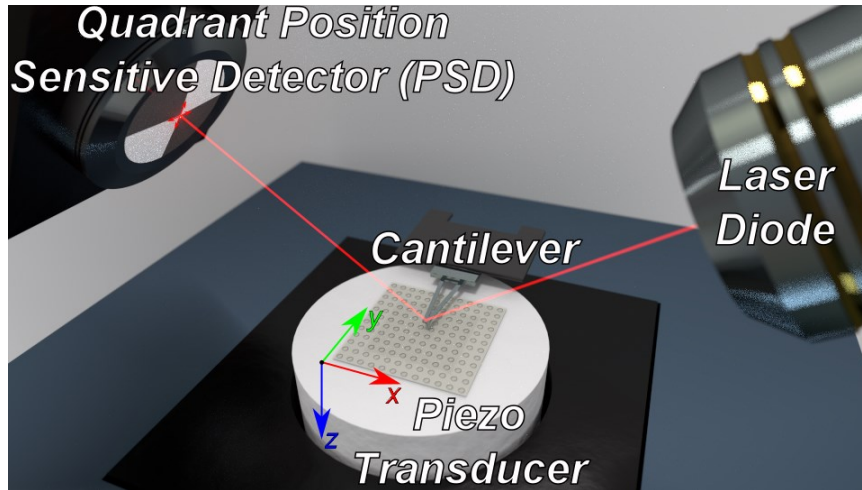


Figure 3.5 Basic components of an atomic force microscope. Sample is shown attached to piezo transducer.

Figure 3.5 shows the most basic components of an atomic force microscope. In the layout of figure 3.5, a microcantilever interacts with the surface of a sample. A laser from a laser diode is directed at the tip of the microcantilever and reflects off of it onto 4 quadrant position sensitive detector (PSD)³³. The purpose of the PSD is to measure the deflection of the microcantilever while the surface is scanned. The sample that is scanned sits on a piezo transducer that moves the sample in the x, y, and z directions. The piezo transducer expands or contracts in response to a voltage applied to it. In some systems, the sample is stationary and the microcantilever is instead attached to a piezo transducer.

The AFM can be operated in three different imaging modes: contact mode (C-AFM), non-contact mode (NC-AFM), and tapping mode (T-AFM).⁷⁴ In contact mode, as the name suggests, the tip of the microcantilever remains in contact with the sample surface during imaging. As the surface is shifted laterally, the cantilever tip will deflect in response to the surface topography. There are two variations on contact mode AFM:

constant height and constant force mode. In constant height mode, the position of the cantilever is kept fixed as the sample is scanned. When a change in the sample's surface topography causes the cantilever to deflect, the deflection is detected from movement of the reflected laser light on the PSD. This generates a feedback signal to adjust the sample height (via the piezo transducer) to restore the cantilever to its original position. In constant force mode, the force applied by the cantilever on the sample surface is kept constant by monitoring the cantilever's deflection and keeping a constant deflection during sample scanning.

In non-contact mode, the cantilever is driven to oscillate at or near its natural resonant frequency by a piezo-transducer attached to the cantilever (not shown in Fig. 3.5). The oscillating cantilever is brought near the sample surface. The typical separation between the tip and sample is approximately 5-15 nm.⁷⁴ As the tip is scanned over the surface, attractive interaction forces between the tip and sample causes changes in amplitude, phase, or frequency of the cantilever oscillation due to damping. These changes in the cantilever oscillation versus the lateral position on the surface provide data for imaging the surface topography.

In tapping mode AFM imaging, the AFM cantilever taps the sample surface during scanning but does not remain in contact. The AFM cantilever is made to oscillate like in non-contact mode, with an amplitude of 20-100 nm when the tip is far from the surface.⁷⁴ The oscillating tip is brought near the sample surface until it begins to lightly tap it. This tapping causes a change in the amplitude of the oscillations from a set-point value. The AFM is set to adjust the sample height during scanning to maintain a constant

amplitude oscillation. The required change in sample height (from the corresponding voltage applied to the piezo transducer) is used to map the surface topography at each lateral surface position. Tapping mode is considered the ideal imaging mode for samples that could be damaged from scanning in contact mode.

3.3 Fluorescence Microscopy

Fluorescence microscopy is an extremely common microscopy technique used in several fields, particularly cell and molecular biology.⁷⁵ Fluorescence microscopy is based on the imaging of a fluorescent chemical, known as a fluorophore, to generate high contrast images. Fluorophores absorb light at a characteristic wavelength, known as the excitation wavelength, and subsequently emits a portion of the absorbed energy back at a characteristic wavelength. Because a portion of the initial absorbed energy is lost through non-radiative processes, the emitted light is always at a longer wavelength (lower energy) than the excitation light. The difference between the excitation and emission wavelengths is known as the Stokes shift of the fluorescent material.

A variety of different fluorescence imaging techniques are used. However, in this thesis, basic epi-illumination fluorescence microscopy is used to characterize the quality of micropatterned charge heterogeneities. The charge heterogeneities are imaged by tagging them with commercially available fluorescent polystyrene nanoparticles. The nanoparticles, obtained from Bang's Laboratories (Fishers, IN) are internally dyed with a fluorophore and have a carboxylic acid surface functionality. In aqueous solution, the nanoparticles develop a negative surface charge and are deposited onto the positively

charged heterogeneities. The deposited particles are imaged with a fluorescence microscope to generate high contrast images (Fig. 3.6) that can be analyzed using image analysis software, such as ImageJ to characterize the pattern dimensions and quality.

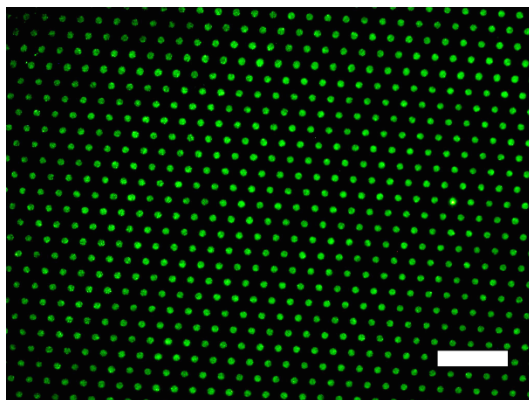


Figure 3.6 Fluorescence microscope image of 110nm diameter fluorescent polystyrene nanoparticles deposited onto micropatterned aminosilane (3-aminopropyltriethoxysilane, APTES) patches on a mica surface. The diameter of the patches is 4.6 μm with a center-to-center separation of 12.5 μm . Scale bar = 50 μm .

The basic components of an upright epi-illumination fluorescence microscope are shown in Figure 3.7. Epi-illumination means that the excitation light and emission light both go through the objective simultaneously. In many fluorescence microscopes, excitation light is generated by a mercury arc lamp. The light emitted from this lamp is passed through an excitation filter to remove wavelengths that do not excite the fluorophore. This also helps with removing wavelengths from the excitation light source that match the emission wavelengths of the sample improve image contrast. After passing through the excitation filter, the excitation light reflects off a dichroic mirror and is conveyed through the objective to excite the sample. The dichroic mirror is a special mirror, mounted at 45° in the light path, reflects shorter wavelength light and transmits

longer wavelength light.⁷⁵ The emission light is collected by the objective and passes through the dichroic mirror and an additional barrier filter that further excludes any light not at the emission wavelength. The excitation, dichroic mirror, and barrier filter are tailored for the fluorophore used to tag the sample. Then, the light passes through a beam splitter to either the eyepiece for direct viewing or a camera or photodetector.

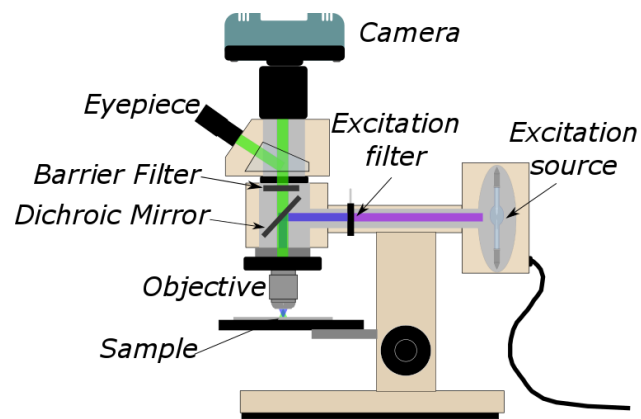


Figure 3.7 Basic components of an upright epi-fluorescence microscope

Chapter 4 Chemical vapor deposition of patterned aminosilane (APTES) monolayers

[Reprinted (with minor modifications) with permission from: C. Pick, C. Argento, G. Drazer, J. Frechette, “Micropatterned charge heterogeneities via vapor deposition of aminosilane” *Langmuir* **2015**, 31, 10725-10733 Copyright © 2015, American Chemical Society.]

4.1 Introduction

Spatial control of chemical functionality is critical in the development of platforms for bio-sensing technologies where the localization and immobilization of molecules or particles to surfaces is necessary.^{14, 22} Of particular interest is the deposition of 3-aminopropyltriethoxysilane (APTES) on oxide surfaces such as SiO₂^{76, 77} or sapphire⁷⁷, as well as on mica surfaces^{78, 79}. APTES contains two different reactive groups: on one end are three ethoxysilanes that can undergo a condensation reaction, covalently attach to surfaces, and crosslink. The other end is a primary amine group that is protonated in aqueous solutions ($pK_A = 9.6$)⁸⁰. Therefore, an APTES-covered surface will be positively charged, allowing for the reversal of the negative charge present on most surfaces in aqueous solutions. Additionally, the primary amine group can undergo further reactions with functional groups such as carboxylic acid, aldehydes, and epoxy groups.⁸¹ This allows APTES films to be used for the covalent attachment of

biomolecules onto surfaces⁸², making APTES monolayers the foundation layer on many devices.^{83, 84, 85}

Creating high quality APTES monolayers can be a challenge, even without the added difficulties associated with creating microscale patterns. In particular, precursors containing multiple reactive groups, e.g. trichloro- or trialkoxy- functionalities, have condensation reactions that are not self-limiting and therefore films can build up well beyond a monolayer⁸⁶. Control over the deposition conditions is particularly important for organosilanes with a primary amine functional group (such as APTES) because the amine group catalyzes the hydrolysis of alkoxy silane endgroups.⁸⁶ As a result, many solution-based deposition procedures of aminosilanes can lead to copolymerization of the precursor molecules in the solution prior to deposition, resulting in the formation of aggregates^{77, 87} or multi-layers on the surfaces⁸⁶. Conversely, unwanted sub-monolayer coverage of primary amine functional groups on a surface can prevent charge reversal and limit the number of binding sites for covalent attachment of target molecules. While multilayers (or sub-monolayers) may be acceptable in certain applications, they are often undesirable. For example, when used as a coupling layer in biosensing devices, non-uniformities in this coupling layer can adversely affect sensor performance.⁸² Similarly, interactions measured with the surface forces apparatus (SFA) are obtained with sub-nanometer resolution in the separation between relatively large surfaces ($\sim 1\text{cm}^2$) with mica as the substrate of choice. Therefore functionalization with high quality monolayers on mica⁸⁸ is particularly important and a surface patterned with well-defined charge heterogeneities with minimal topographical changes would open the door to study double

layer forces between patchy surfaces. The SFA brings about additional requirements for patterning that include the fact that the SFA relies on curved surfaces (radius of curvature of ~2cm).

Both solution and vapor-phase deposition have been employed to create organosilane monolayers.⁸⁹ In solution-based deposition, the organosilane precursor is dissolved in a solvent and the surface is subsequently immersed in this solution for a set period of time. One of the primary issues negatively affecting this approach is the undesired deposition of aggregates and multilayers due to the hydrolysis, and subsequent cross-linking of the precursor molecules in solution prior the deposition on the surface.⁹⁰ To minimize the formation of these aggregates it is necessary to optimize deposition time, temperature, and organosilane concentration.⁸⁶ To limit the amount of dissolved water, anhydrous organic solvents such as toluene⁹¹ or hexane⁹² are commonly used. This helps to minimize hydrolysis during silanization⁸⁹. For aminosilanes in particular, much of the previous work on solution-phase deposition has focused on generating high-quality monolayers without the added challenge of creating microscale patterns. Any patterning method should reproducibly yield regions with high-quality aminosilane monolayers while leaving the surrounding area free of any contamination resulting from the patterning process. Microcontact printing⁹³ is a common solution-based patterning method that has been used for organosilanes^{77, 94} and relies on the use of an elastomeric stamp to control the spatial transfer of an “ink” containing the desired species to a surface. While microcontact printing represents a fairly straightforward method of patterning organosilanes onto surfaces, it inherits all the challenges associated with solution-based

deposition along with additional ones. For example, variations in contact time and pressure applied to the stamp can result in variability in the patterned layers.⁹⁵

Chemical vapor deposition (CVD) is a practical alternative to create organosilane monolayers. In closed-system vapor deposition, the target surface is placed in an evacuated chamber together with a small dish containing a liquid drop of the organosilane. The organosilane first vaporizes and then condenses on all the surfaces, including the target surface. Some of the advantages of vapor deposition over liquid-based deposition protocols include the reduction in the amount of aggregates on the surface, the elimination of solvents, and a better control over excess humidity during the deposition process.^{76, 87, 89} To create a pattern, it is necessary to selectively expose parts of the surface to the vapor phase by using a blocking layer or mask. Alternatively, the deposited organosilane can be selectively desorbed from the surface following deposition. A typical mask consists of a film with open features that are patterned via either e-beam lithography⁹⁶ or photolithography⁹⁷. Once the silane deposition is complete, the blocking layer is removed via a lift-off step. It can be challenging, however, to fabricate such a blocking layer on curved surfaces.

Here we show how chemical vapor deposition of APTES monolayers through a PDMS mask can be used to create positively-charge patterns on mica with minimal topographical variations. The method, based on the work of Jackman et al.⁹⁸, is relatively simple, relies on the dry lift-off of the PDMS membrane after deposition, leaves the unpatterned surface free of residues, and works on curved surfaces. Our results identify key steps that are essential to yield patterns with good quality monolayers. These steps

include hexane extraction and plasma treatment of the membranes, as well as the necessary APTES concentration to minimize topographical variations on the patterned surfaces while maintaining local charge reversal.

4.2 Materials and Methods.

4.2.1 Materials.

Elastomer (Dow Corning Sylgard® 184) is purchased from Robert McKeown Inc. (Branchburg, NJ). SU-8 2025 photoresist and developer are purchased from MicroChem Corp. (Newton, MA). 3-aminopropyltriethoxysilane (APTES) 98% and tridecafluoro-1,1,2,2-tetrahydrooctyl trichlorosilane are purchased from Sigma-Aldrich (St. Louis, MO). Mica (Ruby, ASTM V-1/2) is purchased from S&J Trading (Glenn Oaks, NY), and hydrochloric acid (Fisher Chemical, OPTIMA grade) is diluted with deionized water to a concentration of 10^{-4} M. Fluorescent carboxylic acid-functionalized particles (diameter = 93nm) are purchased from Bang's Laboratories (Fishers, IN). Unless mentioned otherwise, all chemicals are used as received.

4.2.2 Fabrication.

PDMS membranes. Molds for the PDMS membranes are fabricated using conventional photolithography. Micropillar arrays, which serve as template for the

membrane holes, are fabricated on a silicon wafer using SU-8 2025. Following fabrication, the mold is silanized with tridecafluoro-1,1,2,2-tetrahydrooctyl trichlorosilane for 1 hr at room temperature in a vacuum desiccator. The elastomer base and curing agent are mixed in a 10:1 ratio and degassed under vacuum for 20 minutes. Following degassing, the elastomer mix is spin-coated onto the mold so that the layer deposited is thinner than the height of the micropillars, ensuring the membrane contains through-holes. The final membrane thickness used in this work is 20 μm . Following spin-coating, the elastomer is cured at 70°C for 48 hours to ensure complete cross-linking.⁹⁹ Once cured and peeled off the mold, the membranes are imaged under an optical microscope to verify that the pillars are not removed from the mold upon lift-off and that the holes are clean and go through the membrane (Figure 4.1). Shown in Figure 4.1 are optical images of the membranes. For the membrane on the left, the edge was cut to see that there was no PDMS film over the holes (Fig. 4.1A). The image on the right (Fig. 4.1B) is used to check pattern dimensions of the membrane. The photomask used to fabricate the membrane template creates 40 μm diameter pillars with a 12 μm spacing between the pillars. After fabricating and removing the membranes from the template, we image the membranes to verify they have the correct dimensions. The average diameter of the holes in the membrane shown in Fig. 4.1B is 39.8 μm and the average spacing is 11.9 μm . This matches the original specifications of the photomask.

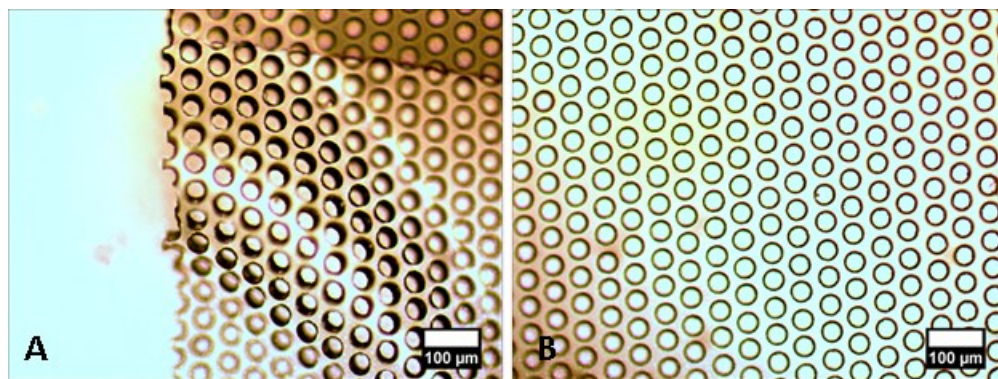


Figure 4.1 Bright-field optical microscope images of the PDMS membranes.

Any remaining unreacted PDMS oligomers in the membrane are removed via an overnight extraction in hexanes.¹⁰⁰ Following extraction, the membranes are dried in a vacuum oven overnight at 70 °C and cleaned in an ultrasonic bath in 200 proof ethanol 3 times for 5 minutes each. The membranes are then dried again in a vacuum oven at 70 °C overnight. Before APTES vapor deposition, the membranes are exposed to an oxygen plasma treatment (50W, 0.3 Torr, and 1 min) on their top surface to produce an oxide layer that acts as a barrier to the transport of small molecules through the membrane, using a home-built plasma reactor. This barrier layer is necessary to reduce the permeability of the membranes to APTES vapor.

Patterned APTES. Freshly cleaved mica surfaces are used as the substrates for APTES deposition. Prepared membranes are carefully applied to the mica with tweezers to ensure conformal contact. The mica surfaces covered with the PDMS membranes are placed in a plastic desiccator (Scienceware® vacuum desiccator) that is transferred to a glovebag (Aldrich® Atmosbag). The desiccator is evacuated for 30min with a mechanical vacuum pump, then sealed while the glovebag is purged. The glove bag is purged with high-purity

nitrogen 3-5 times to remove traces of moisture. Following purging, the desiccator is opened in the dry nitrogen atmosphere inside the glovebag and a small dish of APTES with a known volume is placed inside. The APTES concentrations reported throughout this work are defined as the APTES drop volume used for the deposition (in microliters) per the internal desiccator volume (in liters). The desiccator is evacuated for 1 min and then sealed to allow silane deposition to occur over a period of 4-12 hours at room temperature (22 °C). We found that 4 hours was the minimum time required for the formation of complete patterns. Following this deposition period, the desiccator is purged with nitrogen and the samples are removed. The PDMS membranes are then lifted off the mica surfaces with tweezers and the surfaces are rinsed with 200 proof ethanol. After the ethanol rinse, the surfaces are dried with filtered nitrogen and ready for subsequent characterization.

4.2.3 Characterization.

Surface Forces Apparatus (SFA) experiments. The MK II SFA⁶⁹ equipped with microstepping motors is employed to measure the interaction forces between APTES-APTES, APTES-Mica, and Mica-Mica surfaces in aqueous electrolyte solutions. In the SFA, the surface separation is estimated from the position of the fringes of equal chromatic order (FECO)⁷¹ resulting from multiple beam interferometry (MBI).⁶⁸ The wavelengths at the vertex of the parabolic fringes are used to estimate the surface separation at the point of closest approach for a sphere-plane configuration. To determine surface separation we use the multilayer matrix method¹⁰¹ combined with the fast spectral

correlation algorithm.^{72, 102} The interaction between the two crossed-cylinders is calculated from the deflection of a soft cantilever spring ($k = 118.3\text{N/m}$). The radius of curvature, $R = \sqrt{R_1 R_2}$ is determined from the geometric mean of two spatially resolved FECO profiles coming from perpendicular cross-sections.

Cleaning. All stainless steel parts that come into contact with electrolyte (spring, upper, and lower disk holder) are cleaned in an RBS 35 (Pierce, Rockford, IL) detergent solution, passivated in 50% nitric acid, rinsed thoroughly with ethanol, and dried immediately before use. All of the Teflon parts (bath, tubing assembly) are cleaned in a detergent solution, rinsed thoroughly with water, and dried with nitrogen immediately before use. All glassware is cleaned with detergent, and rinsed with water.

Surface preparation. For the surfaces used in in the SFA, 3-5 μm thick mica pieces are cleaved in a laminar hood and placed on a larger backing sheet. The cleaved mica pieces are coated with 50 nm of silver (99.999% purity, Alfa Aesar) via thermal evaporation (Kurt J. Lesker Nano 38) at a rate of 2-3 $\text{\AA}/\text{s}$. The mica pieces are then glued (on the silvered side) onto a silica support disk for the SFA. For the APTES deposition, the entire disk/silvered mica combination is placed inside the vacuum desiccator and transferred to a glove bag. The APTES deposition procedure follows the same protocol for the patterned surfaces.

Procedure. A Teflon bath is employed inside the SFA chamber and 25 mL of the electrolyte solution is injected while the surfaces are separated using a syringe equipped with all Teflon tubing and valves. The solution is left in the apparatus for 1-2 h for

equilibration prior to force measurements. Each force profile (approach and retraction) is repeated at least 5 times. All experiments were performed at 23 °C.

Double layer interactions. Measurement of double layer forces and their comparison with DLVO (Derjaguin-Landau-Verwey-Overbeck) theory is employed to determine the surface potential and surface charge density of the APTES-covered surfaces. DLVO theory^{32, 35, 58} describes the interaction between two flat surfaces in an electrolyte solution as the superposition of the van der Waals and electrostatic interaction energies. We calculate the electrostatic interaction energy from the excess pressure in the gap, calculated by solving numerically the full Poisson-Boltzmann equation for both constant potential and constant charge boundary conditions using MATLAB's boundary value problem solver (bvp5c), and the electrostatic interaction energy is obtained from a numerical integration of the pressure. Hamaker theory is used for the non-retarded van der Waals interactions with a Hamaker constant of $2.2 \times 10^{-20} \text{J}^{103}$ for the interactions between mica surfaces in aqueous solutions. Finally, we employ the Derjaguin approximation to convert the interaction energy between flat surfaces to the forces normalized by the radius of curvature between crossed-cylinders. In comparing to DLVO theory, the measured forces were fitted for both a Debye length and surface potentials. The fitted Debye length was obtained from a least-squares fit of the force data to an exponential function at separations greater than 1 expected Debye length, κ^{-1} . The Debye length is calculated for a 1-1 electrolyte using: $\kappa^{-1} = \sqrt{\epsilon_0 \epsilon_r kT / 2e^2 n_b}$, where n_b is the bulk ion concentration, k is Boltzmann constant, T is temperature, ϵ_0 is the permittivity of free space, ϵ_r is the relative permittivity of the solution. The surface potential and charge

density of the surfaces were obtained from a least squares fit of the data to predictions for both the constant charge and constant potential boundary conditions.

Fluorescence Imaging. Surfaces are tagged by soaking them for 30-45 minutes in a 10^{-5} volume fraction solution of carboxyl-functionalized fluorescent particles dispersed in deionized water (18.2 M Ω ·cm). Following soaking, the surfaces are rinsed with deionized water and dried with nitrogen. Fluorescence images of the tagged surfaces are taken with an Olympus BH-2 microscope equipped with a Tucsen 3.3MP CCD camera. TSview version 6 is used for image capture. Pattern dimensions and area coverage are measured using ImageJ 1.46r. Coverage is determined by converting the fluorescent images to binary format in ImageJ and measuring the area coverage using the built-in particle analyzer.

Atomic force microscopy (AFM) imaging. Topographical and phase images of the patterned APTES monolayers are taken with a Bruker Dimension 3100 AFM in tapping mode with a scan rate of 1.5 Hz and a scan area of 50x50 μ m. The height of the APTES layers is measured in Bruker Nanoscope Analysis version 1.40 after performing a third order flattening of the raw height images. Figures 4.8 and 4.9 are made in Gwyddion 2.35.

4.3 Results and Discussion.

4.3.1 CVD deposition of patterned APTES monolayers.

The patterning procedure extends the work of Jackman et al.⁹⁸ to aminosilane monolayers. The chemical vapor deposition of APTES relies on the condensation of the molecules from the vapor phase on the accessible areas of a mica surface. Arrays of APTES monolayers are formed by blocking part of the mica substrate with a PDMS membrane that has been patterned with a hexagonal array of through-holes (see Fig. 4.1 for optical micrographs of the membranes and Fig. 4.2).

In principle, APTES deposition only occurs through the membrane holes, and the PDMS membrane acts as a mask (Fig. 4.2B-D). The APTES vapor comes from a droplet of APTES of known volume allowed to evaporate in a partially evacuated desiccator (Fig. 4.2B). The volume of the drop controls the concentration (partial pressure) of APTES in the vapor phase, and needs to be optimized to yield high quality monolayers. The APTES concentration is defined as the APTES drop volume (in microliters) per internal desiccator volume (in liters). Advantages of this method for patterning APTES are the dry lift-off, i.e. it is resist-free (does not require the chemical removal of a sacrificial layer), and the mechanical flexibility of the membrane allowing for the patterning on curved surfaces. In developing the process we faced two important challenges unique to working with a PDMS membrane as a mask: 1) the inherent

permeability of PDMS to small molecules⁹⁵, and 2) the transfer of PDMS oligomers from the membrane to the mica surface^{99, 100, 104}. Additional challenges associated with the deposition process include achieving a good pattern fidelity over large areas and making high quality monolayers with minimal topographical heterogeneities.

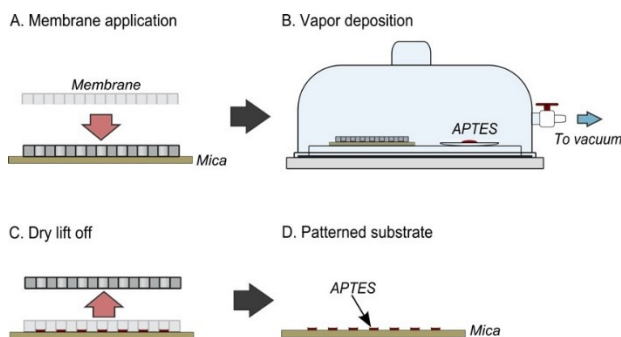


Figure 4.2 Diagram of patterning CVD steps. A) A plasma treated and hexane extracted PDMS membrane is placed on a mica surface (plasma treated side facing up). B) the mica surface is placed in a partially evacuated desiccator in the presence of an APTES drop and left to react for 4-12 hours. C) After the deposition, the membrane is lifted from the surface to yield (D) patterned areas of APTES monolayers.

Transport of APTES through the PDMS membranes can lead to its deposition outside of the desired patterns (in the areas blocked by the membrane). Using thicker membranes and shorter deposition times can help reduce some of the APTES transport through the membrane material. However, we found that plasma treatment of the membranes, prior to their contact with the mica substrates, blocks the diffusion of APTES through the membranes and prevents deposition outside of the open areas. Plasma treatment of PDMS is known to form a silica-like oxide layer on the PDMS surface^{105, 106}, which has been reported to hinder the diffusive transport of small molecules through bulk PDMS¹⁰⁷. To characterize the effectiveness of the plasma treatment, we tagged patterned mica

surfaces with negatively charged fluorescent particles to determine the extent of APTES deposition outside of the patterned areas (Fig. 4.3). In the absence of plasma treatment we observe particle deposition everywhere on the mica surface (Fig. 4.3A). In contrast, we do not observe particle deposition outside of the patterned areas when the top of the PDMS surface has been exposed to oxygen plasma (Fig 4.3B).

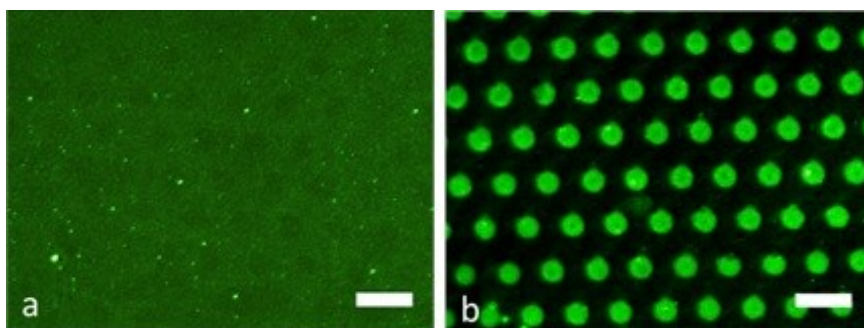


Figure 4.3 Images of APTES patterned surfaces tagged with fluorescent carboxylic acid functionalized particles. The patterned PDMS membrane used as a blocking is A) without barrier layer, and B) with barrier layer generated with 1 min oxygen plasma. The scale bar is 100 μ m.

The right conditions for the plasma treatment are critical to its success in blocking APTES diffusion. To block the transport of the APTES through the membrane it is important to optimize the duration of the plasma treatment. We imaged the surface of the PDMS sheets (without holes) after plasma treatment (see Fig. 4.4). We observed cracks on the PDMS surfaces for plasma treatments longer than a minute (Fig. 4.4D). The presence of cracks increases the permeability of the PDMS to the APTES molecules and leads to deposition outside of the desired areas. On the other hand, if the plasma

treatment is too short, the barrier layer is not sufficient to prevent APTES diffusion either.

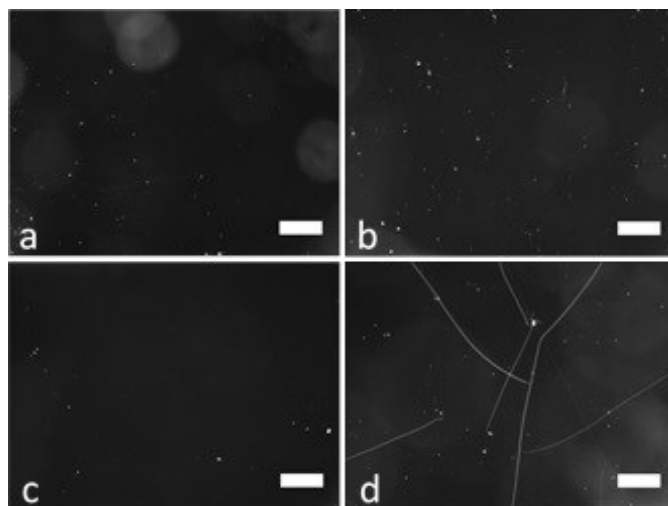


Figure 4.4 Dark-field optical microscope image of PDMS surfaces after different oxygen plasma treatment of increasing duration, A) No plasma, B) 0.5 minutes, C) 1 minute, and D) 2.5 minutes, showing cracks in the barrier layer. The conditions for the plasma treatment are 300 mTorr of oxygen at 50W and the scale bar is 100 microns.

We found that a 300 mTorr and 50W oxygen plasma treatment for 1 minute worked best. Although plasma treatment performed on the side of the PDMS membrane that is in contact with the mica surface was also found to prevent diffusion of APTES through the membrane, it significantly increases the adhesion between the mica and the PDMS membrane. This increase in adhesion makes lift-off difficult and can even leave pieces of PDMS on the mica. Therefore, we opted to perform the plasma treatment on the top-side of the PDMS membranes (the side exposed to the APTES vapor).

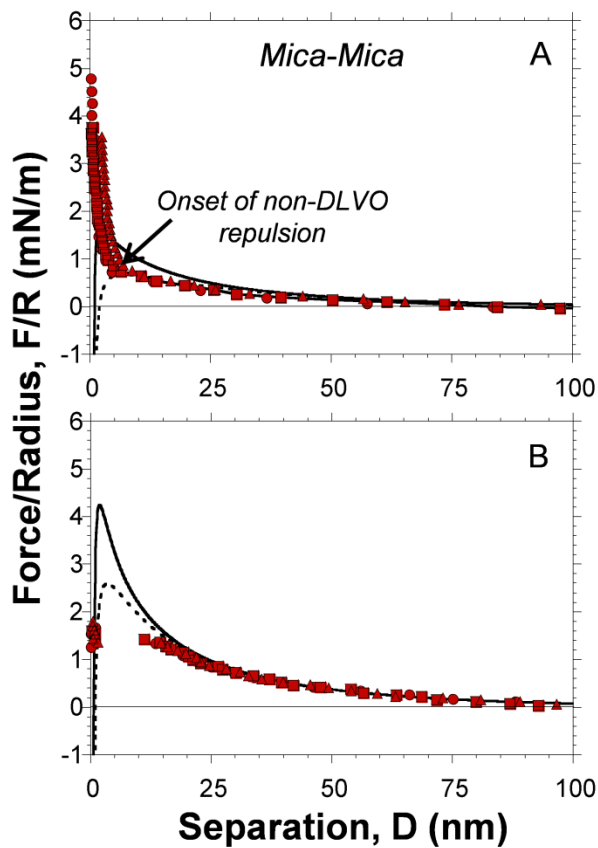


Figure 4.5 Measured force (normalized by the radius of curvature) in 10^{-4} M HCl solution between two mica surfaces as a function of surface separation. Prior to force measurements the mica surfaces were in contact with PDMS sheets with APTES vapor present. The PDMS sheet was A) unextracted with a barrier layer generated on the bottom, and B) extracted membrane with a plasma-generated barrier layer on the top. Solid lines represent DLVO fits with constant charge boundary conditions and dashed lines represent constant potential boundary condition.

Cured PDMS is known to contain traces of unreacted oligomers¹⁰⁰ that can be transferred to the underlying mica substrate, leaving unwanted residues on the surface after the membrane is lifted-off. We investigated if extended curing of the PDMS membrane⁹⁹ followed by hexane extraction¹⁰⁰ (see methods section) could significantly

reduce transfer of oligomers to the mica surface. We performed complete APTES deposition procedures on mica surfaces covered with PDMS sheets of the same thickness as the patterned membranes. We considered both *extracted* and *unextracted* PDMS sheets. After the APTES deposition and membrane lift-off we measured the double layer forces in 10^{-4} M HCl (pH 4.0) using the SFA, see Fig. 4.5. Mica surfaces that have been in contact with unextracted PDMS sheets show strong short-range repulsive forces that cannot be described by DLVO theory alone. We attribute these forces to the transfer of reacted and unreacted PDMS to the mica (Figure 4.5A). In contrast, no short range steric forces are observed for the mica surfaces that have been in contact with the extracted PDMS sheets (Figure 4.5B). In this case, the surfaces jump into van der Waals contact. In addition, the surface forces between these mica surfaces are well-described by DLVO theory with surface potentials in agreement with those obtained for fresh mica surface in 1 mM KClO_4 adjusted to pH 4.98 (with perchloric acid) (Fig. 4.6). The solid line corresponds to a constant charge boundary condition and the dashed line is for the constant potential boundary condition. The forces are well-described by DLVO theory and fit best with the constant potential boundary condition. The fitted surface potential (at infinite separation), Ψ_{mica} , is -93 ± 4 mV and the fitted Debye length is 9.2 ± 0.8 nm, for comparison based on the ionic strength the expected Debye length is 9.7nm. Although the solution conditions are not exactly the same as in Figure 4.5, the fitted surface potential is very close to the one obtained for forces measured mica surfaces after they have been in contact with a PDMS membrane that has gone through the hexane extraction detailed in the methods section.

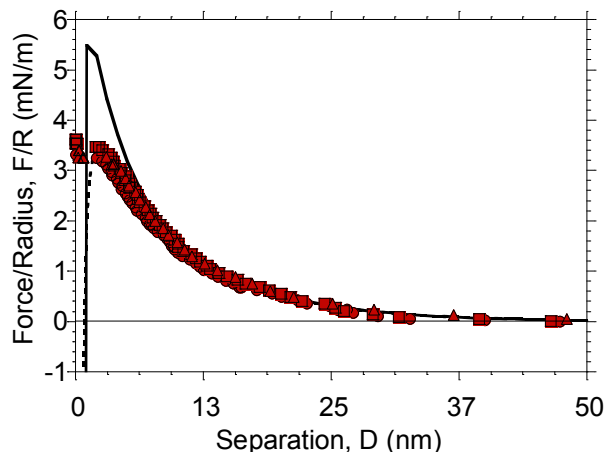


Figure 4.6 Force normalized by radius of curvature measured between two freshly cleaved mica surfaces in 10^{-3} M KClO_4 , pH 4.98. Dashed Line – Constant potential boundary condition, solid line – constant charge boundary condition. The fitted Debye Length is $9.2 \pm 0.8\text{nm}$ and the fitted surface potential is $-93 \pm 4\text{ mV}$.

Therefore based on these results we find that hexane extraction reduces unwanted transfer of the membrane material to the mica surface. Note here that to act as a true control experiment the PDMS sheets remained in contact with the mica surface for as long as the APTES deposition step, and $5\ \mu\text{L/L}$ of APTES vapor was also present in the chamber for the whole process. Due to its positive charge, partial APTES deposition through the membrane would have rendered the surface potential of the mica surface less negative, a feature we do not observe here. Additionally, the sign of the surface potentials were verified by attempting to tag the mica surfaces after the SFA experiments with negatively charged fluorescent particles. No particle deposition was observed on the surfaces, indicating that a net negative surface potential is maintained.

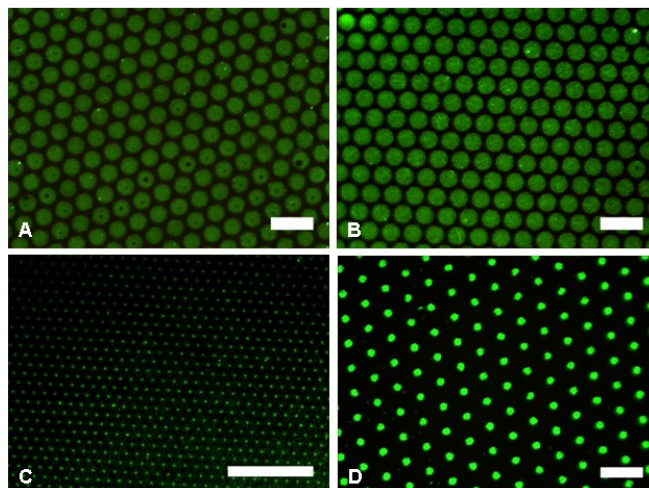


Figure 4.7 Optical micrographs of APTES patterned mica tagged with fluorescent particles. The following APTES deposition concentrations were used: A) 0.25 $\mu\text{L/L}$, B) 1.25 $\mu\text{L/L}$, C) 5 $\mu\text{L/L}$, D) 1.25 $\mu\text{L/L}$ (curved surface, $\sim 2\text{cm}$ radius). Scale bar = 100 μm . Dimensions of the patterned features are given in Table 4-1.

We investigate the effect of both APTES concentration during deposition and feature sizes on pattern fidelity by tagging the surfaces with negatively charged fluorescent particles (see Figure 4.7). These particles deposit on the positively charged (APTES) regions of the surface but not on the negative ones (bare mica) allowing us to quantify APTES pattern fidelity using image analysis. Table 4-1 compares the size of the APTES features, as determined from fluorescent images, to the ones expected based on the array dimensions on the photomask used to fabricate the membrane template. We obtain good pattern fidelity for all the APTES concentrations investigated here and find that the APTES concentration in the desiccator has no measurable effect on the overall quality of the patterns. For patterns created on flat surfaces with feature sizes that are greater than 30 microns we observe that the diameter of individual patterned circles is uniform over large areas of the surface ($>1\text{cm}^2$) and in excellent agreement with the

expected values. However, for curved surfaces and for smaller features (6.5 μm x 6.5 μm), we find that, although we retain the hexagonal array and the pattern features are very uniform over large area, the diameter of the patterned circles is consistently significantly smaller than expected. We suspect that the discrepancy is due to the large aspect ratio of the holes in the membranes when patterning smaller features which could hinder transport of APTES. For example, for the features shown in Figure 4.7C the hole diameter is 6.5 μm and the membrane thickness is 20 μm . In addition, deformation of the membranes when they are in contact with the substrates could alter the size and shape of the patterned features, especially for curved surfaces since the membranes must deform to conform to the curvature.

Table 4-1. Measured pattern dimensions from image analysis and comparison to predicted values.

APTES concentration ($\mu\text{L/L}$)	Array dimensions diameter x spacing (μm)	Measured APTES patch diameter (μm)	Expected area coverage (%)	Measured area coverage (%)
0.25 (Fig. 4.7A)	40 x 12	37.2 ± 0.3	53.7	51.5 ± 0.7
1.25 (Fig. 4.7B)	40 x 12	38.0 ± 1.1	53.7	53.4 ± 2.8
5.00 (Fig. 4.7C)	6.5 x 6.5	3.6 ± 0.1	21.7	9.5 ± 0.2
5.00 (not shown)	30 x 9	29.0 ± 1.5	53.7	47.7 ± 4.3
1.25 ^a (Fig. 4.7D)	40 x 40	24.1 ± 1.1	21.7	9.4 ± 0.9

^a curved surface

While tagging the patterned areas on the surfaces with fluorescent particles showcases pattern fidelity over large areas, it does not allow us to determine the quality of the APTES monolayers within the deposited areas. We characterize the quality of the monolayers within an individual patterned circle using AFM (Fig. 4 and Table 4-2, as well as higher resolution images in Fig. S5 of the supplemental information). AFM imaging can determine the height of the monolayers and identify the presence of aggregates or multilayers on the surfaces. For the three different APTES deposition concentrations investigated, the average height of individual features are uniform and all at least 0.8nm, in agreement with reported values for a full monolayer⁸³. Moreover we do not see evidence of large APTES aggregates inside the patterned areas. However, the APTES height observed for the 5 $\mu\text{L/L}$ concentration is nearly twice the reported value for a monolayer (Table 2), indicating nearly a bilayer coverage. Therefore this concentration should be avoided if a monolayer deposition is required.

The AFM images also indicate the presence of thicker rings around the patterned APTES features, see Figure 4.8 and a higher resolution image for the 0.25 $\mu\text{L/L}$ concentration in Figure 4.9) This is particularly noticeable in the case of the 5 $\mu\text{L/L}$ (Fig. 4C). We suspect that the rings are due to the condensation of the APTES at the triple contact line, which is where PDMS, APTES condensate (and residual water condensate), and mica meet. Similar raised edges have been observed during vapor deposition within PDMS microchannels by George et al.¹⁰⁸ Capillary condensation at the triple contact line is a barrierless nucleation process for unsaturated vapors that is described by the Kelvin equation (Eqn. 4.1)³³

$$\ln\left(\frac{P}{P_{sat}}\right) = \frac{2\gamma V_M}{rRT} \quad (4.1)$$

where $1/r$ is the meniscus curvature, which is negative for a concave meniscus. Here we approximate the height of the condensate as $-r$. P/P_{sat} is the partial pressure with $P_{sat} = 10$ Pa at 22°C ¹⁰⁹, γ is the APTES surface tension (assumed equal to 21 mN/m which is a reported value for triethoxysilane at 20°C)¹¹⁰, V_M is the molar volume of APTES, R is the ideal gas constant, and T is the temperature. Unsaturated conditions ($P < P_{sat}$) should decrease the ring height but cannot completely eliminate the rings. We estimate that a drop volume of about $1.0 \mu\text{L/L}$ or greater results in saturated conditions if we assume that the entire drop evaporates until saturation is reached. Therefore, the APTES drop volume of $0.25 \mu\text{L/L}$ corresponds to unsaturated conditions, while there is sufficient APTES in the $5 \mu\text{L/L}$ concentration to reach saturation (see Table 4-2). The $1.25 \mu\text{L/L}$ drop is estimated to generate a pressure around the saturated limit. To minimize the condensation ring height, it is important to optimize the amount of APTES used in the chamber: we need a monolayer coverage but rings that are as small as possible. Based on the AFM and fluorescent imaging, a concentration of $0.25 \mu\text{L/L}$ minimizes the ring height to that of a bilayer while maintaining a monolayer coverage on the rest of the patches and excellent patterned fidelity.

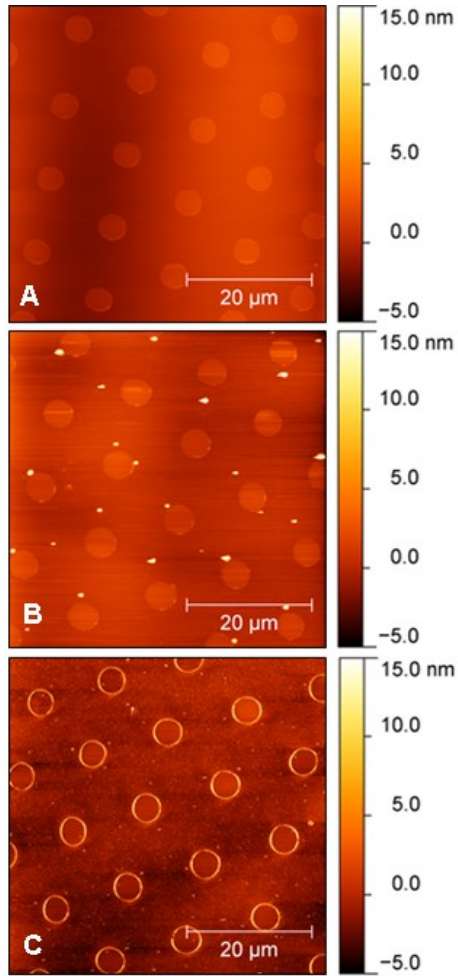


Figure 4.8 AFM height images of patterns deposited at different APTES concentrations
 A) 0.25 $\mu\text{L/L}$ B) 1.25 $\mu\text{L/L}$ C) 5 $\mu\text{L/L}$

Table 4-2 AFM height data for patterned surfaces.

APTES concentration ($\mu\text{L/L}$)	P/P_{sat}	APTES height (nm)	Condensation ring height (nm)	Predicted Kelvin radius (nm)
5	5.29 (saturated)	1.4 ± 0.4	12.8 ± 2.0	<i>N/A</i>
1.25	1.32 (saturated)	0.9 ± 0.2	3.1 ± 0.8	<i>N/A</i>
0.25	0.26	0.8 ± 0.1	1.6 ± 0.8	3.1

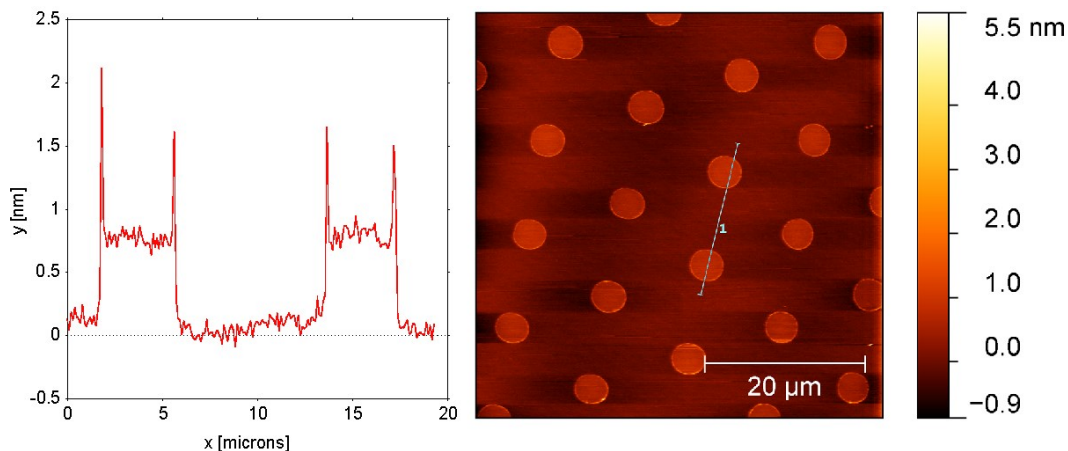


Figure 4.9 AFM height image of mica surface patterned with an array of APTES monolayer patches. The height profile on the left shows the height of the condensation rings and is taken along the line labeled as (1) on the right panel.

4.3.2 Charge density of APTES monolayers.

We measured the surface forces between two APTES monolayers in 10^{-4} HCl aqueous solution to determine how the APTES concentration during deposition influences the surface potential and robustness of the monolayers. Surface forces measured in an aqueous electrolyte solution between ideal APTES monolayers would be well-described by DLVO theory, have a positive surface potential, and be reproducible over multiple approach and retraction curves. Shown in Figure 4.10A-C are the surface forces for APTES films deposited using the three different APTES concentrations. Note that here the APTES deposition on mica is performed without a PDMS membrane (no patterns). The lines in Fig. 4.10A-C represent predictions from DLVO theory^{35, 58} that

were fitted to obtain the surface potential of APTES (ψ_{APTES}) and the Debye length. In all cases the APTES layers appear stable and robust and we see that the measured forces are reproducible over multiple approach and retraction curves, even after repeated contact and pull-out cycles. For separations greater than a Debye length, the forces between APTES monolayers are well-described by DLVO theory for the three APTES concentrations investigated here and are better described by the constant charge boundary condition (solid line). The decay length of the forces is also in good agreement with predictions for a 10^{-4}M (1-1) electrolyte concentration (31nm). Forces between APTES monolayers formed at the highest APTES concentration ($5\ \mu\text{L/L}$) during deposition display repulsion close to contact that is not accounted for by DLVO theory (Fig. 4.10A). This additional steric repulsion could be explained by the existence of multilayers on the surface, which is consistent with the AFM measurements shown in Fig. 4.8C. This additional repulsion prevents the surfaces prepared at the highest concentration ($5\ \mu\text{L/L}$) from reaching adhesive contact, which is in contrast with monolayers prepared at the two lowest concentrations (see the pull-out forces in Table 4-3).

Comparison between the measured forces and DLVO theory for two identical surfaces gives the magnitude but not the sign of the surface potential. To determine the sign of the surface potential of the APTES surfaces, we measured the double layer forces between a bare mica surface (known negative surface potential) and APTES-covered mica surfaces prepared under identical conditions as in Fig. 4.10A-C (see Fig. 4.10D-F). The surface potential of mica is well-characterized in the literature¹⁰³ and has been measured separately (see Fig. 4.5B, and Fig. 4.6). Here we use $\psi_{mica} = -120\text{mV}$. Also

shown in Fig. 4.10 D-F are DLVO predictions for the asymmetrical interactions calculated based on the value of ψ_{APTES} obtained from the corresponding APTES-APTES covered surfaces assuming that the value of ψ_{APTES} obtained in Fig. 4.10 A-C is positive. By comparing the symmetric (APTES-APTES) and asymmetric (APTES-mica) interactions, we find that we achieve charge reversal only at the two highest APTES concentrations (See Table 4-3 for fitted surface potentials and corresponding surface charge densities). The repulsive interaction for the APTES-mica forces shown in Fig. 4.10F indicates that the 0.25 $\mu\text{L/L}$ APTES surface potential is negative. The absence of charge reversal is indicative of an incomplete APTES monolayer on the mica surface, even if the height of the monolayer as measured in the AFM indicates a full monolayer. This discrepancy between the SFA force measurements and the AFM height data is surprising, but could be related to the capillary condensation observed to produce rings shown in Fig. 4.8 and Fig 4.9. Condensation at the triple contact line, as observed with the AFM, provides a nucleation site for the APTES vapor which facilitates monolayer formation. In contrast, no membranes are used to create unpatterned monolayers for the force measurements, therefore these sites for nucleation at the triple contact line are absent. This discrepancy is likely less important at higher APTES concentrations where $P_{APTES}=P_{\text{sat}}$ and condensation can occur everywhere.

The mica/APTES pull-off forces also increases with APTES concentration during deposition (Table 4-3), which is consistent with having more APTES on the surface. We also observed that the pull-off forces for the 0.25 $\mu\text{L/L}$ APTES symmetric is quite large, and similar to APTES-mica pull-out forces. This large adhesive forces was reproducible

over multiple approach and retraction cycles. We suspect that it might be due to incomplete APTES monolayers present on both surfaces where, for example, APTES domains and bare mica interact in contact leading to large adhesion forces.¹¹¹

While APTES monolayers are used extensively to reverse the charge of a negatively charged surface, the surface potential of a monolayer of APTES has not been characterized extensively through force measurements. Grabbe measured the surface forces between films of (γ -aminopropyl)-dimethylethoxysilane (APDMS) on silica surfaces using the SFA under similar conditions as in our experiments (10^{-4} M NaCl solution at pH 5.15)¹¹². Agreement with DLVO theory was found for a surface potential of +24.6mV. This surface potential is significantly lower than the value we obtain based in our surface force measurements with APTES monolayers. It is likely that the discrepancy arises because APDMS contains a single ethoxy group to bind to a surface while APTES has three. In contrast to APTES, APDMS molecules are unable to crosslink with other molecules on the surface, which can prevent the formation a dense monolayer on the surface.

More extensive information is available from electrokinetic measurements of APTES functionalized surfaces. For example, Lin et al.¹¹³ conducted streaming potential measurements of APTES deposited on glass from an acetone solution in 1mM NaCl at different pH values. For a pH value of ~ 4.0 , they obtain a streaming potential of about +92mV. Similarly, Na et al. reported a zeta potential value of +93.8mV in 1mM NaCl for a vapor deposited APTES layer on glass.⁹⁷ A similar aminosilane, 3-aminopropyltrimethoxysilane (APTMS), deposited on silicon wafers was also reported to

have a streaming potential of about +92mV at pH 4.0.¹¹⁴ These values are in agreement with our measured potentials for APTES films ($\psi_{APTES} = +110 \pm 6$ mV for the 1.25 $\mu\text{L/L}$ APTES concentration), especially when considering that streaming potential values are expected to be lower than surface potential values obtained through direct force measurement, as they are measured at the slip plane away from the surface.

Table 4-3 Fitted values for DLVO theory for the forces curves in Fig. 2 and Fig. 5. The expected Debye length at 10⁻⁴M and 23°C = 30.6 nm

APTES concentration ($\mu\text{L/L}$)	Debye length, κ^{-1} (nm)	Surface potential, Ψ_s (mV)	Surface charge density, σ (e/nm^2)	$-F_{\text{adh}}/R$ (APTES-mica) mN/m	$-F_{\text{adh}}/R$ (symmetric) mN/m
5.00	30.9 ± 2.4	117 ± 9	0.036 ± 0.006	122.4 ± 7.0	0
1.25	30.0 ± 0.8	110 ± 6	0.032 ± 0.004	77.1 ± 8.0	1.5 ± 0.9
0.25	31.5 ± 3.8	-99 ± 11	-0.025 ± 0.006	12.3 ± 0.5	134.4 ± 6.0
Extracted:mica	30.9 ± 0.8	-120 ± 5	-0.038 ± 0.004	N/A	28.9 ± 2.3
Unextrated:mica	31.5 ± 6.5	-74 ± 3	-0.015 ± 0.001	N/A	0

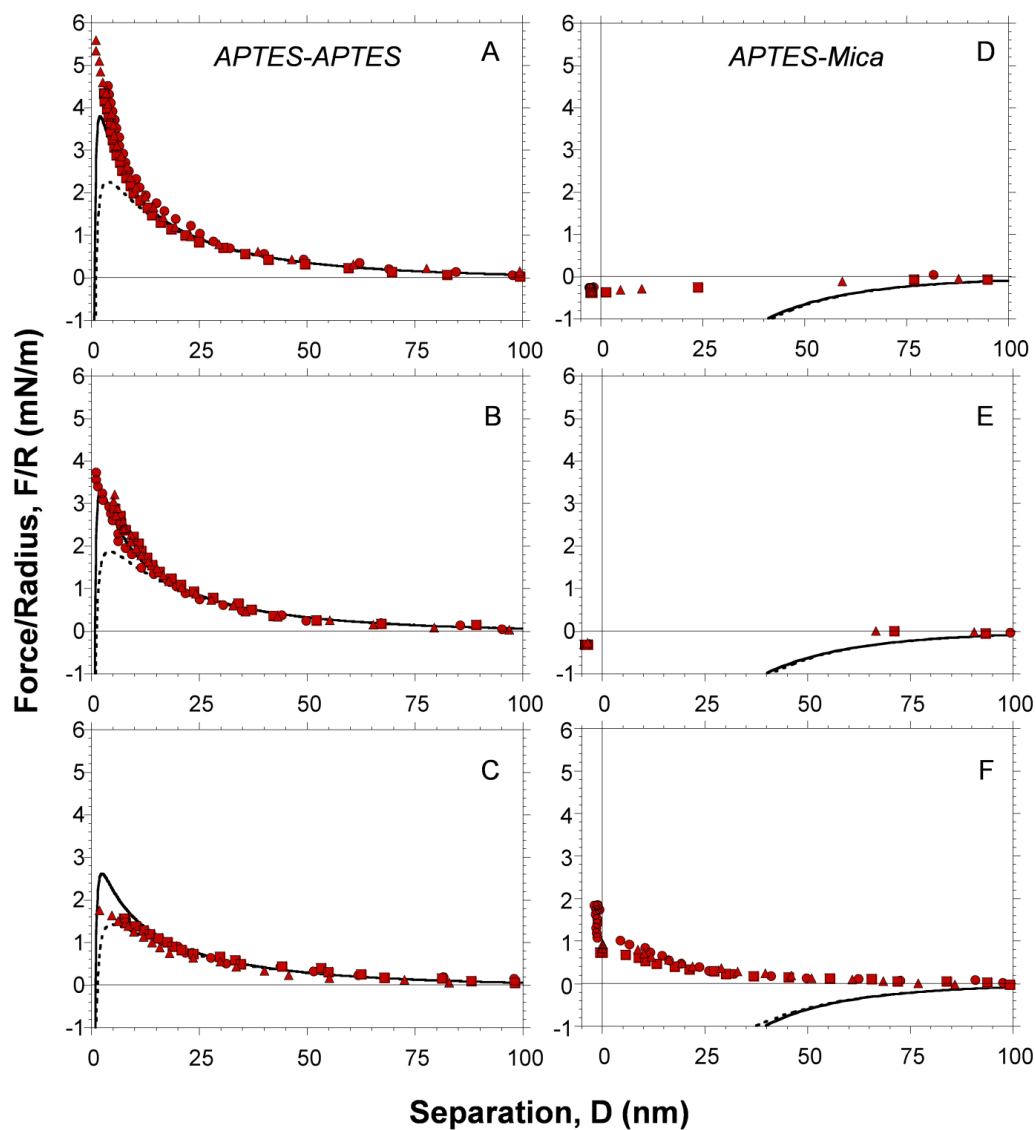


Figure 4.10 Force curves, normalized by the radius of curvature, as a function of separation measured between (A-C) APTES-APTES (symmetric), and (D-F) APTES-mica (asymmetric) surfaces in 10^{-4} M HCl. Each plot show multiple approach/retraction curves, each indicated by different symbols. The APTES concentration during the deposition are (A,D) $5 \mu\text{L/L}$, (B,E) $1.25 \mu\text{L/L}$, (C,F) $0.25 \mu\text{L/L}$. Solid lines represent DLVO fits with constant charge boundary conditions and dashed lines represent constant

potential boundary condition. The sign of ψ_{APTES} in (A-C) is determined from the force measurements in (D-F).

4.4 Conclusions

We have shown a method that relies on elastomeric membranes to spatially control the chemical vapor deposition of high quality aminosilane monolayers to create microscale charge heterogeneities on mica substrates. The advantages of the method include a dry lift-off of the elastomeric membranes that leaves the unpatterned areas free of residues, the capability to pattern on curved surfaces, a high pattern fidelity of full monolayers with minimal topographical variation at the nanoscale, and the absence of aggregates on the surface. The surface potential of both the APTES films and mica were obtained from a series of direct force measurements. These direct force measurements indicate the deposition conditions necessary for charge inversion of the underlying mica surfaces. Additionally, pattern fidelity was characterized by tagging the APTES patterns with fluorescent particles and observing the patterns under a fluorescence microscope. Finally, APTES height measurements were taken with an AFM revealed the formation of condensation rings when the APTES vapor pressure is close to saturation. Additionally, we found that a hexane extraction and plasma treatment of the PDMS membranes were necessary to prevent oligomer contamination of mica from the membranes and to block APTES diffusion in the PDMS, respectively. Ultimately, we find that 1.25 $\mu\text{L/L}$ is the optimum concentration for the reproducible deposition of APTES monolayers on mica, as it leads to charge reversal (Fig. 4.10 and Table 4-3), good pattern fidelity (Fig. 4.7), a full monolayer (Fig. 4.8), and low condensation ring height (Table 4-2).

Chapter 5 Estimating particle-patchy surface interactions for with variable boundary conditions

5.1 Introduction

Reliable predictions of particle deposition behavior at solid-liquid interfaces are necessary in a wide variety of systems of technological interest. Perhaps the single most common example is the transport of colloidal particles through porous media, such as packed bed filtration⁵ or colloidal transport through soil into underground aquifers.^{6, 8, 115} Control over particle deposition can also be exploited as a means of “bottom-up” assembly where surfaces can be precisely pattern to control the location of particle deposition.^{14, 22} Conversely, particle deposition can be an undesirable characteristic in certain systems where it leads to surface fouling.^{24, 26} One example is surface fouling in microfluidic systems.²⁸ In a microfluidic system, particle deposition on microchannel walls can easily lead to surface fouling, clogging the channel, and potentially resulting in complete device failure.

Particle deposition involves the interplay of conservative surface forces and dissipative hydrodynamic interactions. Colloid-colloid and colloid-surface interactions are typically calculated within the framework of the well-known DLVO (Derjaguin-Landau-Verwey-Overbeek) theory.^{34, 35, 58} DLVO theory treats particle surface interactions as the superposition of interactions arising from electrical double layer

overlap and van der Waals forces. Deposition is defined as unfavorable when there is a significant repulsive electrostatic energy barrier and favorable when this energy barrier is absent.

One of the fundamental assumptions of DLVO theory applied to colloidal systems is that the surfaces involved are homogeneous. In other words, the surfaces are well-described by a uniform surface charge and free of any physical asperities. Yet, all but the most ideal of systems contain heterogeneities.^{37, 116} The presence of these heterogeneities can alter particle deposition behavior dramatically over predictions based on average surface properties.¹¹⁷ Consequently, predicting particle deposition behavior in the presence of heterogeneities is of great value for real systems and a significant effort^{37, 43, 45, 118, 119} has been devoted to developing methods of calculating particle-surface interactions in the presence of surface heterogeneities. These methods^{43, 45, 119, 120, 121} are based on discretizing both the particle and surface and calculating a net interaction by summing up the individual DLVO interactions between each of the elements, such as in the grid surface integration (GSI) method.^{43, 120} However, these methods can be computationally complex⁴¹ and typically rely on analytical approximations for double-layer interactions based on linearization of the Poisson-Boltzmann (valid for low, <25mV, surface potentials) under constant surface potential boundary conditions. A more generalized method of predicting particle-surface interactions that is valid for arbitrary surface potentials and boundary conditions would allow for the estimation of particle-surface interactions for a wider range of systems arbitrary surface potentials and boundary conditions applied to the surfaces.

The following chapter outlines a simplified method of estimating interactions with patchy heterogeneously charged surfaces referred to here as the “linear mixing approximation”. This semi-analytical method is simpler than implementation of the GSI technique developed by Duffadar and Davis and relies on the “electrostatic zone of influence” (ZOI) argument originally developed by Kozlova and Santore and used throughout literature on patchy surface interactions. While this simplified formulation was previously shown to work well for surfaces containing many small patches in relation to the zone of influence ^{45, 119}, it will be demonstrated by comparisons with GSI estimates published in literature that with the proper scaling of the ZOI, it can be extended to estimate interactions under conditions of highly heterogeneous surfaces where a single heterogeneity is located within the ZOI. Finally, we will use full numerical solutions to the non-linear Poisson-Boltzmann equation to predict particle-surface interactions for arbitrary surface potentials and both constant potential and constant charge boundary conditions. It will be shown that boundary conditions can have a significant effect on interactions and can alter the critical surface coverage of heterogeneities required to generate favorable deposition conditions.

5.2 Existing methods of calculating interactions with heterogeneous surfaces

5.2.1 Idealized model of a chemically heterogeneous surface

A simplified representation of a heterogeneously charged surface is a one bearing uniform attractive heterogeneities (referred to as patches) with a constant spacing, such as shown in figure 5.1. This surface will be referred to as the “collector” in subsequent sections of this chapter as it is one onto which particle deposition can occur. These patches bear a different surface potential (Ψ_{Patch}) or surface charge density (σ_{Patch}) than the bulk surface on which they reside. (Ψ_{Bulk} , σ_{Bulk}).

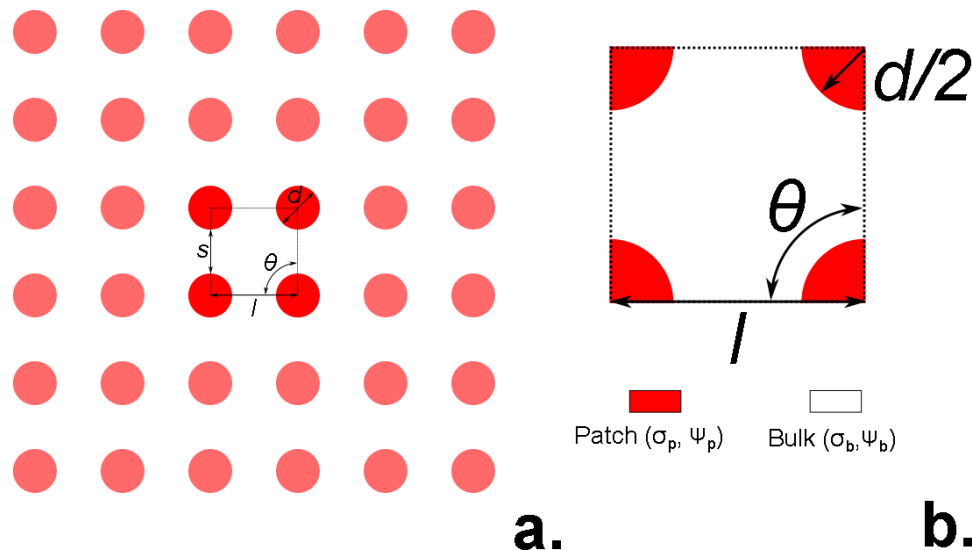


Figure 5.1: a) Diagram of patterned surface, highlighting patch diameter(d), center-to-center spacing (l), edge-to-edge spacing ($s=l-d$), and the lattice angle (θ) b) larger image showing a single unit cell of the pattern. Red circles represent patches and the white background represents the bulk surface.

The patches could come from a variety of sources, such as the adsorption of polyionic species^{19, 121} on a surface or patterned charge heterogeneities^{16, 20, 22}. In the case of a randomly adsorbed species, however, uniform spacing is an approximation of the distribution of patches based on the average patch distribution.

To specify the surface coverage of patches, the patch diameter (d) and spacing (l for center-to-center or s for edge spacing where $s = l-d$) need to be specified. Additionally, we can specify a lattice angle (θ) for the array to allow for different patch arrangements. With a known patch diameter, spacing, and lattice angle, the fractional surface coverage of the patches can be calculated. For an ordered array of patches, the fractional coverage is simple the area of a single circular patch divided by the area of a unit cell of the pattern. (1 unit cell contains the equivalent of one patch).

$$f_p = \frac{A_{\text{patch}}}{A_{\text{unit cell}}} = \frac{\pi}{4\sin(\theta)} \left(\frac{d}{l}\right)^2 \quad (5.1)$$

For the special case of a square array ($\theta=90^\circ$), $f_p = (\pi/4) * (d/l)^2$ and for a hexagonal array ($\theta=60^\circ$), $f_p = (\pi/2\sqrt{3}) * (d/l)^2$. A value of $d/l = 1$ corresponds to the maximum patch coverage where the patches can still be considered discrete (non-overlapping).

5.2.2 Review of the grid surface integration (GSI) technique

Prior studies have been conducted to calculate particle-surface interactions for heterogeneously charged surfaces.^{41, 43, 115, 117, 120, 121, 122} The technique used in many of these studies are usually based upon the surface element integration (SEI) technique.¹²³

The SEI technique was originally presented as a more accurate method of calculating particle-surface interactions for small particles where the Derjaguin approximation is invalid due to the curvature of the particle becoming similar in scale to the range of interactions.¹²³ The SEI technique can also be used for particles of arbitrary shape interacting with a flat collector surface.¹²⁴ In the SEI technique, the particle's surface is discretized, while the opposing collector surface is treated as an infinite (homogeneous) flat plate. The net DLVO interaction is calculated by summing of the interactions between each of the particle's discrete surface elements with the opposing flat plate.

While the SEI technique involves discretizing only the particle's surface, investigations with heterogeneous surfaces on particle deposition require that collector surface must also be discretized. This allows the heterogeneous nature of the surface to be incorporated into calculations by assigning different surface properties (surface potential and/or Hamaker constant) to each individual element. One method previously published treated the collector surface as an assemblage of spherical nanoscale subunits.¹²² The interaction between the particle and each spherical subunit are summed up to get the net interaction. More recently, studies that investigate heterogeneous surface use a method called the grid-surface integration (GSI) technique developed by Duffadar and Davis.^{43, 120} The GSI technique discretizes both particle and collector surfaces and calculates the net interaction from the sum of pairwise interactions between each element of the collector and particle. Figure 5.2 shows an illustration of the GSI technique.

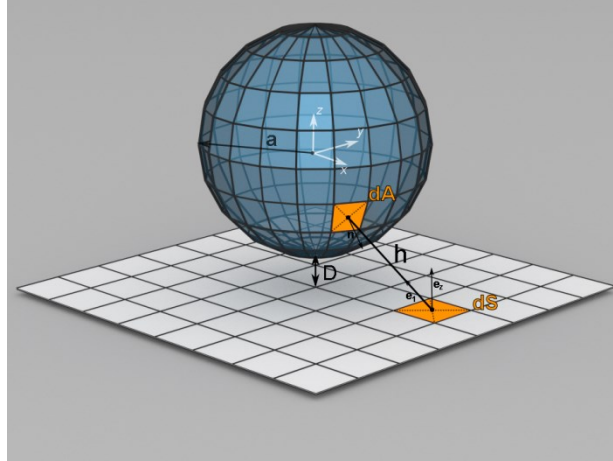


Figure 5.2: Illustration of the grid-surface integration technique showing a discrete particle element interacting with a collector surface element

The next part of this section will summarize how the GSI technique works as described by Duffadar and Davis⁴³. Consider a particle of radius a approaching a flat surface with a separation D . The particle and surface are discretized into area elements dA and dS respectively. The surface is discretized first and the size of the discrete elements of the collector surface is selected to be at least as small as the individual surface heterogeneities present.⁴³ After breaking up the collector surface, the surface of the particle is discretized, where the area of the particle surface element, dA , can be related to the collector surface element, dS , as follows⁴³:

$$dA = \frac{dS}{(\mathbf{n} \cdot \mathbf{e}_z)} \quad (5.2)$$

Where \mathbf{n} is a unit vector normal to the particle surface element and \mathbf{e}_z is a unit vector normal to the collector surface. The pairwise interaction force or energy df between the two elements dS and dA is calculated as:

$$df = P(h)(\mathbf{e}_1 \cdot \mathbf{e}_z)dS \quad (5.3)$$

Where \mathbf{e}_1 is a unit vector pointing in the direction of the two elements and $P(h)$ is the net interaction force or energy per unit area between two infinite flat plates separated by a distance, h . The entire interaction between a single element dA on the particle with the collector surface, dF is then just the sum of all of the interactions between dA and every element on the collector:

$$dF = \sum_{Collector} dF = \sum_{Collector} P(h)(\mathbf{e}_1 \cdot \mathbf{e}_z)dS \quad (5.4)$$

To calculate the entire interaction for the particle, F , every individual element on the surface must be summed up:

$$F = \sum_{Particle} \sum_{Collector} P(h)(\mathbf{e}_1 \cdot \mathbf{e}_z)dS \quad (5.5)$$

The interaction force or energy per unit area $P(h)$ comes from expressions for the DLVO interaction between infinite flat plates per unit area based on an approximate analytical expressions for the electrostatic interaction. In particular, the electrostatic double layer

expressions of Hogg-Healy-Fusternau⁵⁴ are used extensively to calculate the electrostatic force, however, other expressions have been used as well.⁴¹

The GSI technique provides a way to numerically integrating the net energy or force between a particle and a heterogeneous surface by allowing the individual collector surface elements to be different assigned properties (such as surface potential and Hamaker constant) to generate surface with arbitrary layouts of heterogeneities. Originally, the technique was used to investigate random distributions of cationic patches on anionic surfaces^{43, 120, 121} but it has also been used to investigate ordered arrays of heterogeneities¹¹⁹. Additionally, the GSI technique has been adapted to study particles interacting with spherical collectors as opposed to a flat collector surface.⁵⁹ Likewise, a slightly modified version of the technique have been used to study the interaction of a particle with a single heterogeneous patch as opposed to multiple patches.⁴⁴

While the GSI technique represents a straightforward way of calculating interactions, it can be computationally intensive.⁴¹ The interaction between each area element must be computed and summed up. The next section discusses a simplification over the GSI technique developed for estimating interactions with heterogeneous surfaces bearing many patches.

5.3.3 The electrostatic zone of influence (ZOI)

A simplification to the GSI approach was proposed by Bendersky et al. based on “mixing” the homogeneous patch-particle and bulk-particle interactions by the surface

coverage of the patches on the surface.^{41, 45, 119} Bendersky et al. found this technique provided excellent agreement to the GSI technique when there were many patches within a region called the electrostatic zone of influence (ZOI).

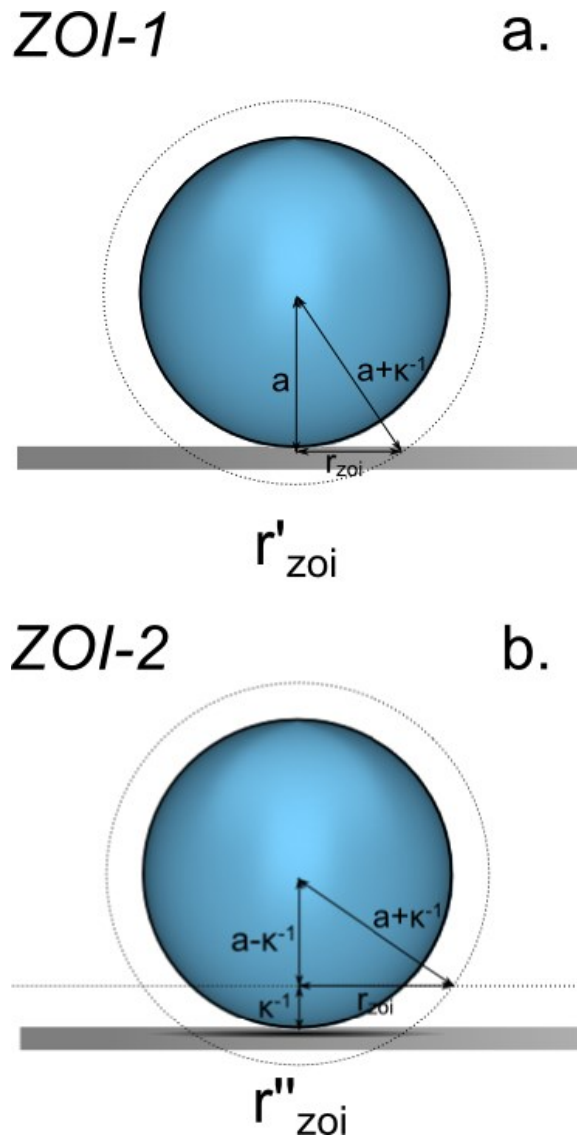


Figure 5.3: Diagram showing the derivations of the radius of the electrostatic zone of influence for a.) a single Debye length intersecting the surface (ZOI-1) b.) the intersection of the debye lengths on the particle and surface (ZOI-2). κ^{-1} is the Debye length and a is the particle radius

Electrostatic interactions outside the ZOI do not contribute significantly to the total particle-surface interaction force and energy profile due to the decay of the interaction with the Debye length and the curvature of the particle. The radius of the ZOI scales with the particle's radius and Debye length and can be estimated from a simple geometric argument when the particle is in contact with a surface, as shown in figure 5.3. Two different versions of the zone of influence have been used throughout literature, depending on whether one or two Debye lengths are used to govern the ZOI scaling.^{19, 41, 44, 45, 119} The first argument (denoted here as ZOI-1), originally defined by Kozlova and Santore, is defined as the area of intersection of a *single shell* of the thickness of one Debye length away from the particle where it intersects with a surface.¹⁹ (Fig. 5.3a) The radius of ZOI-1, r'_{zoi} , is:

$$r'_{zoi} = \sqrt{2a\kappa^{-1} + (\kappa^{-1})^2} \quad (5.6)$$

Where a is particle radius and κ^{-1} is the Debye length. However, when the particle radius, is much larger than the Debye length ($a \gg \kappa^{-1}$) this expression simplifies to:

$$r'_{zoi} \cong \sqrt{2a\kappa^{-1}} \quad (5.7)$$

A second argument (ZOI-2) is defined as the area of intersection of *two shells* on Debye length away from the particle and surface when the two are in contact.^{19, 121} (Fig. 5.3b)

The radius of ZOI-2, r''_{zoi} , is³:

$$r''_{zoi} = 2\sqrt{a\kappa^{-1}} \quad (5.8)$$

Both arguments differ by a factor of $2^{1/2}$ ($r_{zoi} = 2^{1/2} r_{zoi}$) and have been used throughout the literature.^{19, 41, 44, 121} The value of the ZOI radius is often cited as $\sim\sqrt{a\kappa^{-1}}$.^{44, 45}

The fractional patch coverage within the ZOI can be calculated as:

$$f_{p,zoi} = \frac{A_{patch,zoi}}{A_{zoi}} \quad (5.9)$$

Where A_{zoi} is the area enclosed by the zone of influence, $A_{patch,zoi}$ is the area covered with patches enclosed by the ZOI, and $f_{p,zoi}$ is the fractional coverage of the patches within the ZOI. A value of $f_{p,zoi} = 1$ corresponds to the entire ZOI being covered with the patch surface and $f_p = 0$ corresponds to all bulk surface. When the ZOI is much larger than the patch spacing, $f_{p,zoi} = f_p$. In words, the patch coverage within the zone of influence matches the net coverage for the entire surface. This is illustrated in figure 5.4a. As the ZOI decreases in size (due to decreasing Debye length or particle radius) and approaches the length scale of the patches, patch coverage in the zone of influence can deviate significantly from the average surface coverage (Fig. 5.4b)

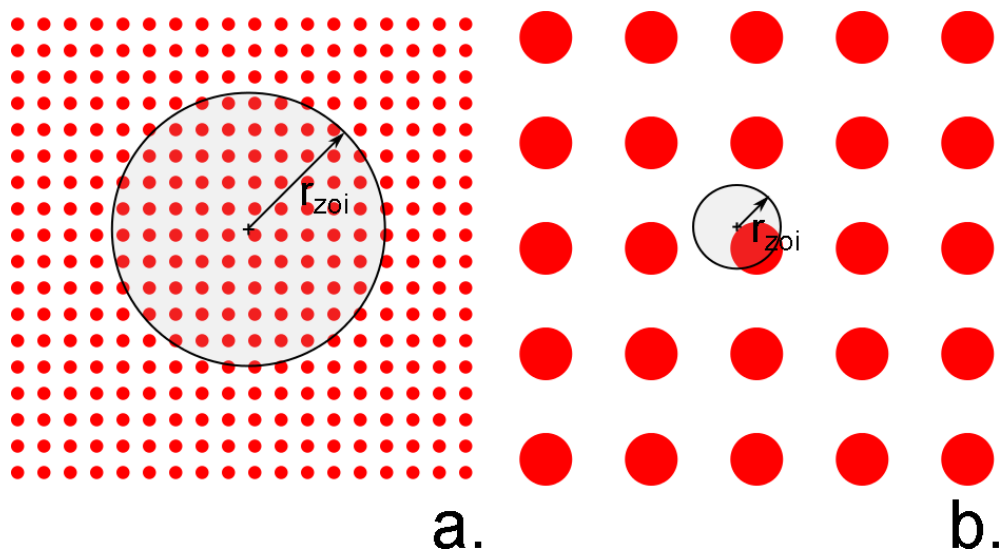


Figure 5.4: Figure showing two different zones of influence on patterned surfaces. Both surfaces have the same patch diameter to patch spacing ratio (d/l) and consequently the same patch surface coverage. a) Zone of influence much larger than patch spacing b) zone of influence of approaching same size as patch spacing

5.3.3 Simplified method of predicting colloidal interactions: linear mixing approximation (LA)

For a patchy heterogeneous surface, there are two possible “extremes” to the net particle-surface interaction. These limits come from treating the bulk and patch surfaces as homogenous surfaces. (The particle is only interacting with either the homogeneous “patch” surface or homogeneous “bulk” surface.) One would expect the net interaction to fall somewhere between the limits of these homogeneous interactions. A simplified method compared to the GSI technique for calculating electrostatic interactions with patchy surfaces weights the patch-particle and patch-bulk interactions by the fractional

patch coverage within the ZOI.^{41, 45} The net electrostatic interaction, $U_{EDL,net}(D)$, for a particle at any position on a patchy surface is:

$$U_{EDL,net}(D) = f_{p,zoi}U_{EDL,patch}(D) + (1 - f_{p,zoi})U_{EDL,Bulk}(D) \quad (5.10)$$

Where $U_{EDL,patch}(D)$ is the particle interaction energy with the patch surface (treating the patch as homogenous surface) and $U_{EDL,Bulk}(D)$ is the particle interaction energy with the bulk surface. This same expression also be applied to forces by recognizing:

$$F_{EDL,net} = -\frac{dU_{EDL,net}(D)}{dD} \quad (5.11)$$

Where $F_{EDL,net}$ is the net electrostatic interaction force of a particle with a patchy surface. While used here to describe a heterogeneously charged surface, a similar treatment was employed previously to investigate surfaces with physical asperities⁶⁰ and equation 5.10 could be extended to work with physically heterogeneous surfaces by “shifting” treating the patches as pillars and shifting the this “pillar” interaction by the height of the pillars.¹¹⁹ Using equation 5.10, the total net DLVO interaction is calculated by adding the van der Waals interaction:

$$U_{DLVO,net}(D) = U_{EDL,net}(D) + U_{VDW}(D) \quad (5.12)$$

One important point to note about the total net DLVO interaction in eqn. 5.12 is that only the electrostatic interaction depends on patch coverage within the ZOI. In reality, a patchy surface can have different van der Waals interactions for the patch and bulk materials owing to different Hamaker constants, depending on how the patch is formed. For the purposes of this chapter, the van der Waals interaction will be assumed to be identical for a patch and bulk materials (identical Hamaker constants are assumed and van der Waals interactions are the same everywhere).

This simplified method essentially acts like an ideal mixing assumption, where the particle-patch and particle-bulk interactions are simply added together by weighting the interactions based on $f_{p,zoi}$. As such, this technique will be referred to as the linear mixing approximation or linear approximation⁴¹ (LA) throughout this chapter. It's important to recognize that when the zone of influence is much larger than the patch spacing ($2r_{zoi} \gg l$), the particle's ZOI samples a surface that is representative of the entire surface coverage. ($f_{p,zoi} \sim f_p$). In this regime, subsequently referred to as the many patch regime, the particle's ZOI encompasses several patches. It is this many patch regime that was originally shown to work well with the linear mixing approximation by Bendersky and Davis previously, giving results that agreed with GSI calculations.^{45, 119} When the ZOI is small compared to the pattern dimensions, however, the value of $f_{p,zoi}$ can vary spatially on the surface. If $f_{p,zoi} = 0$ or 1 the homogeneous bulk or patch interactions are recovered, respectively. This regime will be referred to as the single patch regime.

5.3.3 Homogeneous surface interactions

Electrostatic double layer interactions with homogeneous surfaces

To use equation 5.10 to calculate net interactions with patchy surfaces, it is necessary to have the electrostatic interaction potentials for the homogeneous patch and bulk surfaces. This interaction potential can be calculated from full numerical solutions or approximate analytical expressions. One of the most common analytical expressions used to calculate electrostatic interactions for asymmetrical surfaces is the expression developed by Hogg-Healy-Fusternau (HHF).⁵⁴ The expression for the electrostatic interaction potential for a sphere-plane geometry from HHF is:

$$U_{EDL}(D) = \pi a \varepsilon_0 \varepsilon_r (\psi_1^2 + \psi_2^2) \left[\frac{2\psi_1\psi_2}{(\psi_1^2 + \psi_2^2)} \ln \left(\frac{1 + \exp(-\kappa D)}{1 - \exp(-\kappa D)} \right) + \ln(1 - \exp(-2\kappa D)) \right] \quad (5.13)$$

Where a is the particle radius, ε_0 is the permittivity of free space, ε_r is relative permittivity, ψ_1 is the particle surface potential, ψ_2 is the surface potential opposing surface (assigned the surface potential of either the patch or the bulk), κ is the inverse Debye length, and D is separation at the point of closest approach. When the patch surface potential is used, the electrostatic potential energy for the particle with the (homogenous) patch material is obtained: $U_{EDL,patch}$. When the bulk surface potential is used, the interaction potential is for the particle with the bulk surface: $U_{EDL,bulk}$.

$U_{EDL,patch}$ and $U_{EDL,bulk}$ represent the two “bounds” for a net electrostatic interaction between a particle and patchy surface.

The HHF expression relies the Debye-Hückel approximation to linearize the Poisson-Boltzmann equation and assumes constant potential boundary conditions. Consequently, it should only be valid for low surface potentials, $|\psi| < 25\text{mV}$, although it has been found to agree with full numeric solution up to about $\sim 50\text{-}60\text{mV}$.⁵⁴ Further, the Derjaguin integration method is used to obtain sphere-plate interaction potentials in equation 5.13. As a result, equation 5.13 is applicable when the particle radius is much larger than the range of interaction ($a \gg \kappa^{-1}$).

Calculation of the electrostatic interaction at high surface potentials and arbitrary boundary conditions requires numerical solutions of the Poisson-Boltzmann equation. The Poisson-Boltzmann equation can be solved numerically using a boundary value problem solver such as MATLAB’s boundary value problem solver (bvp5c). Numerical solutions provide the electrical potential in the gap between two infinite parallel plates which is used to obtain the pressure in the gap. (One plate corresponds to the particle and the other is assigned the surface potential of either the bulk or patch surface). This pressure is numerically integrated to obtain the flat plate interaction energy per unit area. Here, the Derjaguin approximation converts the interaction energy between flat surfaces to the forces normalized by the radius of curvature of the particle. As such, these results are only valid when the assumptions of the Derjaguin approximation are satisfied ($a \gg \kappa^{-1}$ and $a \gg D$). When employing the Derjaguin approximation, the particle radius must be much larger than the range of interactions.

van der Waals interactions

The van der Waals interaction between a sphere and plane from Hamaker theory is:

$$U_{VDW}(D) = -\frac{aA_H}{6D} \quad (5.14)$$

Where A_H is the non-retarded Hamaker constant and D is the separation. For the purposes of this chapter, the van der Waals interaction for the patch and bulk surfaces will be assumed to be approximately equal and assigned the same Hamaker constant. A similar assumption was made in published literature using the GSI technique.^{43, 119}

DLVO interaction

The total DLVO interaction energy, U_{DLVO} , is the superposition of the electrostatic and van der Waals interaction potentials:

$$U_{DLVO}(D) = U_{EDL}(D) + U_{VDW}(D) \quad (5.15)$$

5.4 Results and discussion

5.4.1 Zone of influence modification for out-of-contact positions

The ZOI arguments derived previously (eqn. 5.7 and 5.8) are for a particle in contact with a surface.^{19, 121} However, it is expected that the ZOI size should vary with separation.⁴³ One method to modify the size of the zone of influence with separation is to increase the size of the intersecting shell(s) as the particle moves away from the surface by the particle-surface separation, D . (D being the separation at the point of closest approach). This modifies the radius of the zone of influence for out-of-contact positions, as shown in Fig. 5.5:

For the ZOI-1 argument (Fig. 5.5a):

$$r'_{zoi}(D) = \sqrt{2\kappa^{-1}(a + D) + (\kappa^{-1})^2} \quad (5.16)$$

When the particle radius is much larger than the separation ($a \gg D$) and the Debye length ($a \gg \kappa^{-1}$), this expression simplifies back to the in-contact expression:

$$r'_{zoi}(D) = r'_{zoi} = \sqrt{2\kappa^{-1}a} \quad (5.17)$$

For large particles, the ZOI-1 argument can be approximated as constant regardless of separation. Likewise, the second zone of influence expression (ZOI-2) can be adapted to out of contact positions (Fig. 5.5b):

$$r''_{zoi}(D) = \sqrt{D^2 + 2D(a + \kappa^{-1}) + 4a\kappa^{-1}} \quad (5.18)$$

If the particle radius a is much larger than κ^{-1} and D , this expression can be simplified to:

$$r''_{zoi}(D) = \sqrt{2a(D + 2\kappa^I)} \quad (5.19)$$

Unlike the ZOI-1 argument, the modified ZOI-2 has a radius ($r''_{zoi}(D)$) that increases with separation, even for large particles. Both the modified ZOI-1 and ZOI-2 arguments recover the original in-contact expressions when $D = 0$.

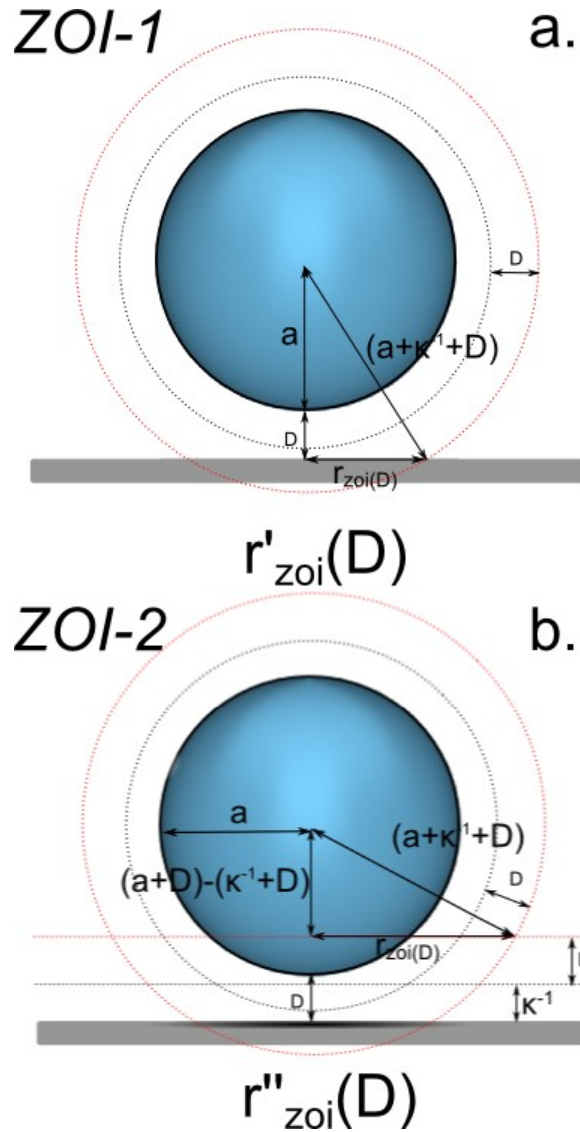


Figure 5.5: Diagram showing the modifications of the radius of the ZOI for out of contact positions a) a single Debye length shell intersecting the surface (ZOI-1) b) the intersection of the debye lengths on the particle and surface (ZOI-2). κ^{-1} is the Debye length, a is the particle radius, and D is the particle-surface separation.

5.4.2 Linear mixing approximation versus GSI technique – many patches in the ZOI

The linear mixing approximation (Eqn. 5.10) has been shown to work well for many patches in the ZOI previously by Bendersky and Davis.^{45, 119} However, the homogeneous patch and bulk surface interactions were still calculated using the GSI technique except with homogenous surfaces. One advantage to the using the linear mixing approximation would be the ability to use fully analytical solutions, such as in equation 5.12 based on the Derjaguin approximation without needing to resort to the GSI technique for the homogeneous surface solutions. This was mentioned by Bendersky and Davis but not investigated.¹¹⁹ Here we compare published calculations for particle interactions with heterogeneous surfaces obtained from the full GSI technique to the linear mixing approximation using a purely analytical approach

Figure 5.6 shows the particle- patchy surface arrangement investigated with the GSI technique in literature¹¹⁹ and a comparison to the linear mixing approximation. The inset of figure 5.6A shows the size of the ZOI (using ZOI-1, eqn. 5.17) for particle radii of 0.5 μm and 1.0 μm in an electrolyte solution with $\kappa^{-1} = 5\text{nm}$. For both particle radii, the zone of influence encompasses many patches. Because the ZOI is much larger than the pattern dimensions, it is assumed that $f_{p,zoi}$ is equal to the surface coverage obtained from the pattern dimensions. This is true regardless of whether the the ZOI-1 or ZOI-2 argument is used. The surface coverage of patches within the ZOI is further assumed to be identical for all lateral positions on the surface and will not change with separation.

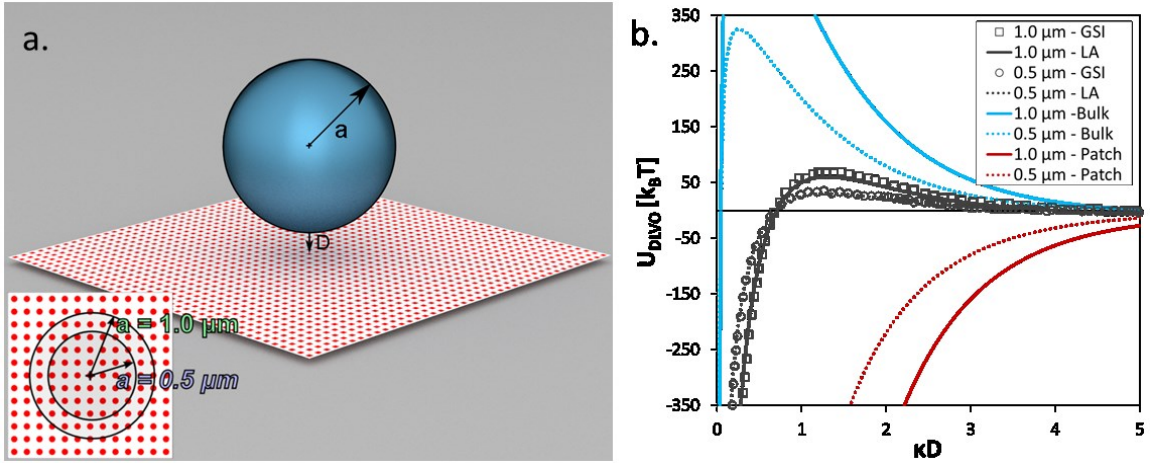


Figure 5.6: a) Particle of radius a and separation D interacting with surface containing circular heterogeneities arranged in a square array ($d=10\text{nm}$, $l=20\text{nm}$; $f_p=f_{p,zoi}=19.6\%$). Inset shows relative size of ZOI-1 for different particle radii ($a = 0.5$ and $1.0 \mu\text{m}$). b) Comparison of GSI technique results of Bendersky and Davis¹¹⁹ (points) to the linear approximation method (LA) with the Derjaguin approximation (lines). The patch (red) and bulk (blue) homogeneous interactions are also shown. Values used for calculation: $\kappa^{-1} = 5\text{nm}$, $\psi_{\text{patch}} = +50.8\text{mV}$, $\psi_{\text{bulk}} = \psi_{\text{particle}} = -25.4\text{mV}$, and $A_H = 5 \times 10^{-21}\text{J}$

Figure 5.6 B shows the comparison of the linear mixing approximation (lines) to published¹¹⁹ GSI solutions for particle radii of $a = 0.5$ and $1.0 \mu\text{m}$ with $\kappa^{-1} = 5\text{nm}$ (points). The dimensions of the patches are found in the caption of Fig. 5.6. The HHF expressions with the Derjaguin approximation (Eqn., 5.13) are used here in the linear mixing approximation to calculate electrical double layer interactions. In Fig. 5.6b, the linear mixing approximation (lines) matches the published GSI solutions (points) exactly for both particle radii. It was previously demonstrated that the linear mixing approximation works in the many patch regime^{45, 119} however in those demonstrations the particle-patch and particle-bulk homogeneous interactions came from GSI solutions for homogeneous surfaces. Here the Derjaguin approximation is used and no implementation

of the GSI technique is required to obtain the particle-homogeneous surface interactions. Thus, a fully analytical approach can provide identical results to the GSI technique.

5.4.3 Linear mixing approximation versus GSI technique – single patch in the ZOI

While the linear mixing approximation has been shown to work well with many patches in the ZOI, an alternative situation that can be encountered is a particle approaching a single, small heterogeneity. How does the linear mixing approximation work in this case of a single patch within the ZOI?

As the ZOI approaches the size of a single patch, one could reason that averaging the surface coverage becomes less accurate compared to when there are many patches in the ZOI. Further, the differences between the ZOI-1 and ZOI-2 arguments will become apparent as $f_{p,zoi}$ will differ for each argument used. This section will extend the use of the linear mixing approximation to a single patch within the ZOI and investigate the effects of the ZOI arguments (ZOI-1 or ZOI-2) on the predicted interaction profiles. The results from the linear mixing approximation will be compared to results published by Shen et al., who using a slightly modified GSI technique to calculate particle-surface interactions in the presence of a single attractive heterogeneity on a repulsive bulk surface.⁴⁴

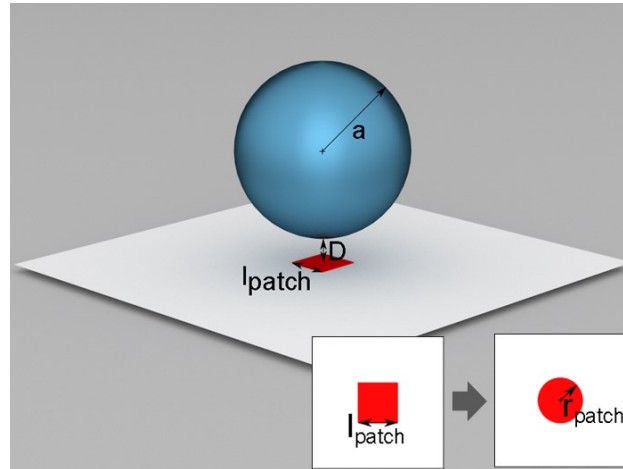


Figure 5.7: Illustration of particle of radius a interacting with surface bearing a square chemical heterogeneity of side length, l_{patch} . Particle is centered over heterogeneity at a separation, D .

In Shen et al.'s analysis, a particle is centered on a single attractive patch. The net particle-surface interaction energy is calculated from a GSI technique as the size of the patch, ionic strength, and surface potential of the patch and surrounding bulk surface are varied. This arrangement is illustrated in Figure 5.7. The surface potentials of the patch, bulk, and particle are reported in Table 5.1 for the different ionic strengths investigated in along with the Hamaker constant and particle radius.

Table 5-1: Parameters for DLVO interaction energy estimates from Shen et al.⁴⁴

Ionic Strength	1 mM	10 mM	100 mM
ψ_{patch}	36 mV	25 mV	13 mV
ψ_{bulk}	-60 mV	-48 mV	-24 mV
ψ_{particle}	-87 mV	-81 mV	-30 mV
A_H		1×10^{-20} J	
a		0.5 μm	

Shen et al. used the double layer interaction expressions of HHF coupled with a non-retarded van der Waals interaction for the DLVO interaction for infinite flats per unit area

for the discretized surfaces. They also included a Born interaction potential in their analysis. The Born interaction potential between a sphere and a plane is:

$$U_{Born}(D) = \frac{A_H\sigma}{7560} \left[\frac{8a + D}{(2a + D)^7} + \frac{6a - D}{D^7} \right] \quad (5.20)$$

Where a is the particle radius, D is the particle-surface separation, A_H , is the Hamaker constant, and σ is the collision parameter. A value of $\sigma = 0.5\text{nm}$ was used. Adding additional interaction terms beyond electrostatic and van der Waals interactions leads to what is known as extended DLVO (abbreviated as xDLVO) theory.⁶⁰ To match the published results, a Born interaction potential is added to the linear mixing approximation method:

$$U_{xDLVO,net}(D) = U_{EDL,net}(D) + U_{VDW}(D) + U_{Born}(D) \quad (5.21)$$

To compare the results of Shen et al. to the linear approximation with the added born repulsion, one further assumption is made here about the patch geometry to simplify the calculation of $f_{p,zoi}$. Shen et al. primarily investigated square heterogeneities. Here, the square heterogeneity is approximated as a circular patch with the same equivalent area. (shown in the inset to figure 5.7).

When a particle approaches a single heterogeneity, the fractional patch coverage within the ZOI will depend of the argument used (ZOI-1 or ZOI-2) to calculate the ZOI radius. This is in contrast to the case of a surface bearing many small patches much smaller than the ZOI where $f_{p,zoi}$ will be the same if either ZOI-1 or ZOI-2 is used. This is because the ZOI-2 argument creates a larger interaction area and thus samples more of

the surface surrounding the patch than ZOI-1, lowering the value of $f_{p,zoi}$. Here, we will use both ZOI-1 and ZOI-2 arguments to calculate $f_{p,zoi}$ for the linear mixing approximation and compare to the published results from Shen et al.⁴⁴

Single patch regime comparison with ZOI-1 argument

Figure 5.8 shows a comparison of the linear mixing approximation with Shen et al.'s published results at three different ionic strengths (1, 10, and 100 mM) using the ZOI-1 argument to calculate $f_{p,zoi}$. The zone of influence was assumed to be constant with separation (equation 5.17) owing to the size of the particle ($a = 0.5 \mu\text{m}$). The plots show the interaction energy with varying patch size, where the patch size is given as the side length of the original square heterogeneity in nanometers. The surface potentials and Hamaker constant used are reported in Table 5.1.

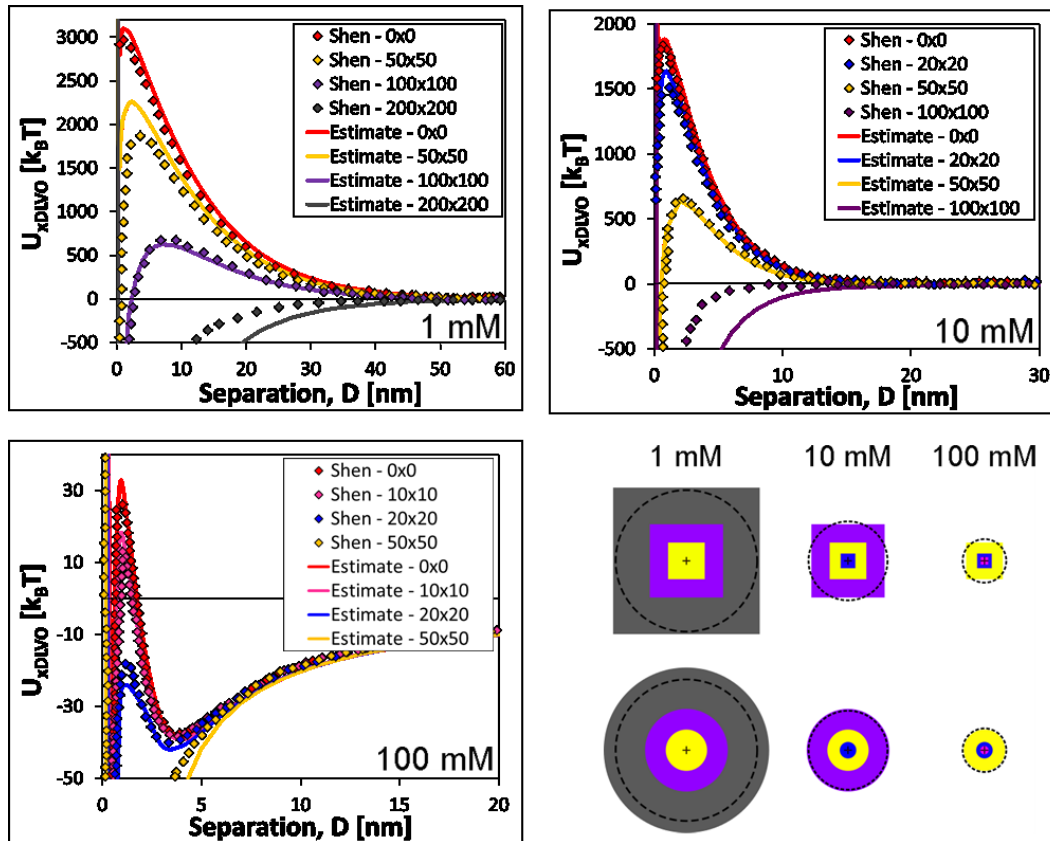


Figure 5.8: Comparison between the GSI results of Shen et al.⁴⁴ (points) with estimates from the linear mixing approximation method (lines) for a 0.5 μm radius particle at 1, 10, and 100mM (1:1) electrolyte solutions using the ZOI-1 argument. Values for the Hamaker constant and surface potentials are given in Table (5.1). The relative size of the ZOI is shown for each patch and ionic strength is shown in the bottom right. Values are plotted for the different sizes of the square patch (given as side length by side length in nm)

The linear mixing approximation generates results comparable to the published results⁴⁴ using the GSI technique. This is true for all of the ionic strengths. The approximation tends to slightly overestimate the patch attraction for large patches (compared to the ZOI) and underestimate the patch attraction for small patches. This is most likely attributable to the fact that, while the patch is centered within the ZOI, its interaction is weighted

equally to the surround surface (i.e. by the net coverage within the ZOI). One limitation of the linear mixing approximation is that the exact same interaction will be obtained regardless of where the patch is located in the ZOI. This can be demonstrated by comparing estimates from the linear mixing approximation with another geometry investigated by Shen et al. with a single circular heterogeneity and 9 smaller heterogeneities, shown in Figure 5.9

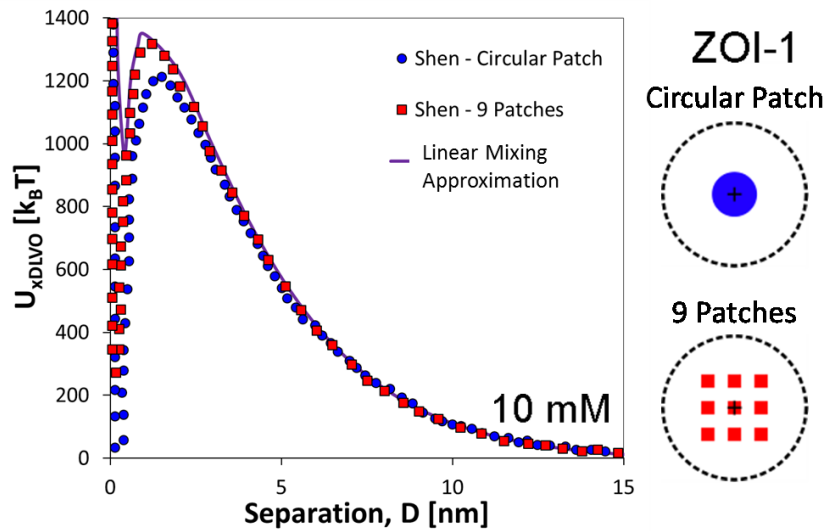


Figure 5.9: Interaction with a circular patch of radius 16.93nm and 9 square patches (from Shen et al.⁴⁴, points) each 10x10nm compared the linear approximation (line) in 10mM solution with a particle of radius 0.5 μm . The circular patch and 9 patches have the same equivalent area and should have the same interaction with the approximation method. Note how the 9 patch case match the approximation exactly due the patchy surface being distributed throughout the ZOI.

The equivalent area of the single patch and multiple patches shown in figure 5.9 is identical and both are completely enclosed by the ZOI. Therefore, the exact same $f_{p,zoi}$ is obtained and the linear mixing approximation gives the same predicted interaction for both cases. However, as evident from Figure 5.9, the approximation give results that

agree with the full GSI technique for the 9 patch case where the heterogeneities are distributed in the ZOI. This demonstrates that the linear mixing approximation provides estimates that agree much better with GSI solutions with multiple patches distributed throughout the ZOI.

Single patch in zone of influence – ZOI-2 argument

The previous section showed comparisons of the linear mixing approximation to published GSI results by Shen et al. using the smaller ZOI-1 argument. The same comparison is made here with the ZOI-2 argument, as shown in Figure 5.10.

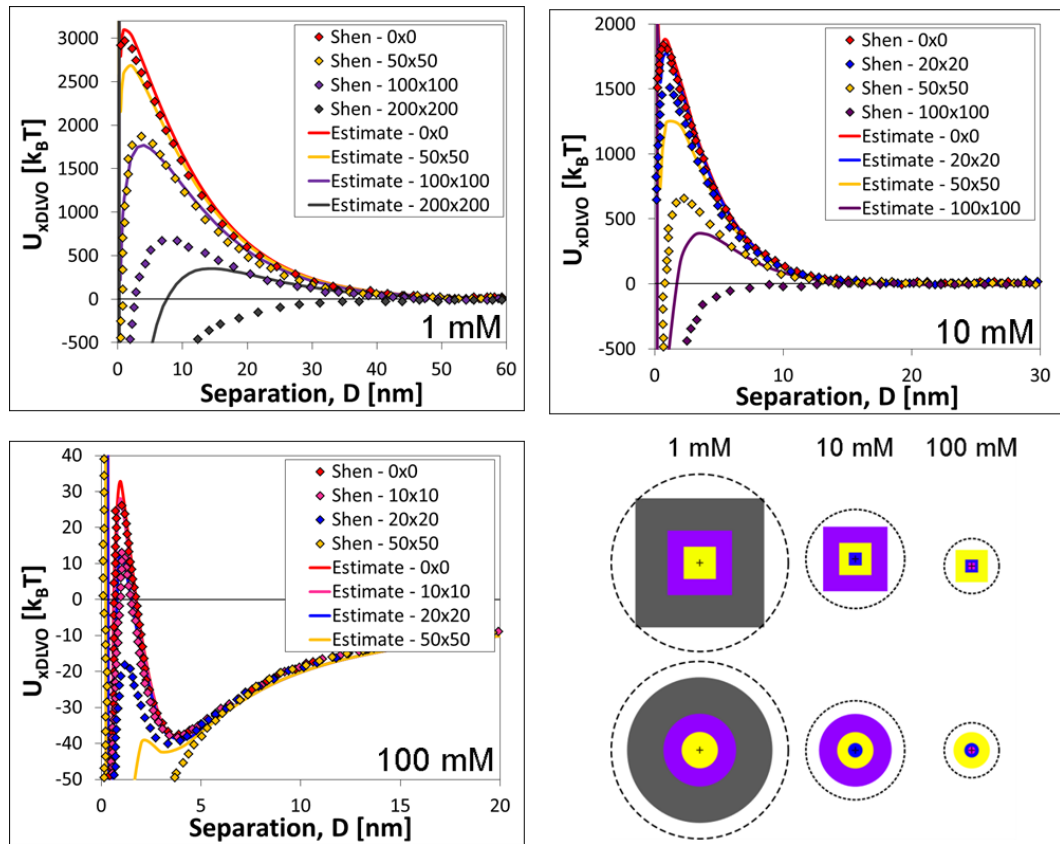


Figure 5.10: Comparison between the GSI techniques (points) from published results⁴⁴ (points) with estimates from the linear mixing approximation (lines) for a 0.5 μm radius particle at 1, 10, and 100mM (1:1) electrolyte solutions using the ZOI-2 argument.

Values for the Hamaker constant and surface potentials are given in Table (5-1). The relative size of the ZOI is shown for each patch and ionic strength.

When the ZOI-2 argument is used to calculate $f_{p,zoi}$ in Fig. 5.10, the estimates obtained from the linear mixing approximation are always much more repulsive than the GSI calculations published by Shen et al. This is in contrast to the much better agreement obtained using the ZOI-1 argument in figure 5.9. As the bulk surface is repulsive, this immediately implies that the value of $f_{p,zoi}$ is too low and the radius calculated using the ZOI-2 argument, based on the intersection of two Debye “shells” is too large to yield comparable results between the linear mixing approximation and GSI solutions.

5.4.6 Transitioning from many patches in the ZOI to a single patch – effects of ionic strength

We have treated the many patch and single patch regimes as two separate cases thus far. However, it is possible to transition between these two regimes by changing the particle radii or the ionic strength of the solution. To illustrate the effects of the ionic strength on ZOI size on particle-surface interactions, consider a particle of radius $a = 0.5 \mu\text{m}$ interacting with a surface containing circular patches arranged in a square array ($\theta=90^\circ$), similar to the previous example of Fig. 5.6. Each patch has a diameter (d) of 60nm and a center-to-center spacing (l) of 120nm. The corresponding patch coverage for this surface is $f_p = 19.6\%$. The particle is allowed to probe the patchy surface at different spatial locations, analogous to a particle translating over the surface with its ZOI (using the ZOI-1 argument) sampling different spatial locations. Two different ionic strengths

(1:1 electrolyte; 0.1mM and 10mM) illustrate how the size of the zone of influence affects the net particle-surface interactions at different locations. The surface potential of the patches is assumed to be +25.4mV, while the bulk's surface potential is assumed to be -25.4mV. For simplicity, the particle is assumed to have a surface potential that matches the bulk. The Hamaker constant is $A_H = 5 \times 10^{-21}$ J for both the patch and bulk material. Equations 5.13 will be used to calculate the electrostatic interactions for the homogeneous (patch-particle and bulk-particle) interactions.

Figure 5.11A shows 10 randomly distributed ZOI's in a 0.1mM solution ($\kappa^{-1} = 30.7\text{nm}$, $r'_{\text{zoi}} = 175.2\text{nm}$). Figure 5.11B shows 10 random ZOI's in a 10mM solution ($\kappa^{-1} = 3.0\text{nm}$, $r'_{\text{zoi}} = 54.8\text{nm}$). The net patch coverage in each of the ZOI's can be calculated along with a standard deviation for the patch coverage.

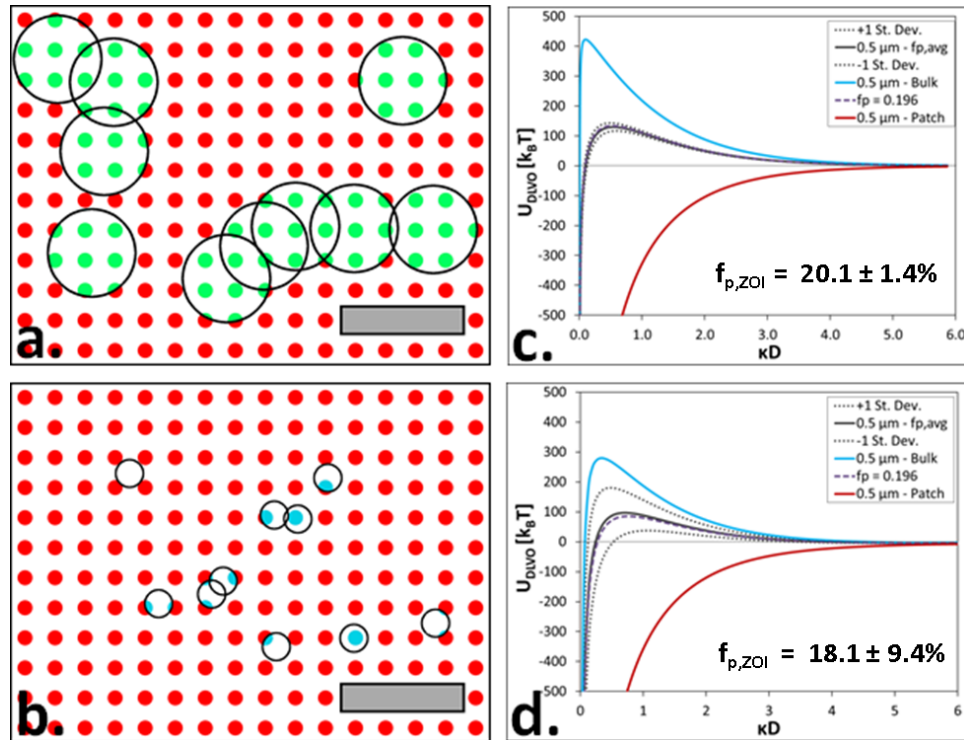


Figure 5.11: a) ZOI-1 ($a=0.5 \mu\text{m}$, $\kappa^{-1} = 30.7\text{nm}$) on square array of patches ($d=60\text{nm}$, $l=120\text{nm}$; $f_p = 19.6\%$) with $\kappa^{-1} = 30.7\text{nm}$ b) ZOI-1 ($\kappa^{-1} = 3.0 \text{nm}$) on same array (Scale

bars in A and B = 500nm) c) DLVO interaction energy profile for low ionic strength case in “5.11a” d) DLVO interaction energy for high ionic strength case in “5.11d”. Surface potentials values: $\psi_{\text{patch}} = +25.4\text{mV}$, $\psi_{\text{particle}} = \psi_{\text{bulk}} = -25.4\text{mV}$.

In the low ionic strength case (Fig. 5.11A), the net coverage of patches in the ZOI is $20.1 \pm 1.4\%$ while in the high ionic strength case (Fig. 5.11B) it is $18.1 \pm 9.4\%$. In both cases, the average $f_{p,zoi}$ is nearly agrees with the average based on the pattern dimensions of 19.6%. However, the high ionic strength case, when the zone of influence is small, the variability of the patch coverage is large compared to the low ionic strength case. These values of the patch coverage as well as the distribution can be used to calculate particle interaction potentials from the linear mixing approximation (Figure 5.11C and Figure 5.11D). Figure 5.11C shows the interaction energy for the low ionic strength case (Fig. 5.11A) and Figure 5.11D shows the interaction energy for the high ionic strength case (Fig. 5.11B). The net interaction is shown based on the average $f_{p,zoi}$ and its standard deviation. Additionally, the net interaction based on the pattern dimensions ($f_{p,zoi} = 19.6\%$) is shown for comparison, along with the particle-patch and particle-bulk (homogeneous) interactions. The interaction based on the *average* coverage in the ZOI nearly agrees with the value from the pattern dimensions both each cases. The difference between 5.11C and 5.11D is the variation in the interaction. No matter where the ZOI is located in 5.11A, the interaction is nearly constant everywhere. However, in 5.11D, there is a large variability in the interaction depending on if the ZOI is centered over a patch or the bulk surface due to the small size of the ZOI at higher ionic strength (smaller Debye length) compared to the patch sizing.

The example calculations in Fig. 5.11 provides several insights into how ionic strength can influence particle deposition behavior on patchy surfaces. First, consider the low ionic strength case of Figure 5.11A,C. At all spatial locations on the surface, the interaction is nearly identical and there is an energy barrier present of $\sim 130k_bT$. Ignoring any hydrodynamic effects, with such an energy barrier present, particle deposition is energetically unfavorable despite the presence of the attractive heterogeneous patches. (An energy barrier of less than $10k_bT$ is typically considered necessary for particle deposition to occur.)⁵⁹ The high ionic strength presents a more interesting surface. While the average energy barrier is $\sim 90k_bT$, there are large fluctuations, from ~ 30 - $180k_bT$ depending on whether the particle is over a patch or the bulk. One can imagine that if the ionic strength was a little higher, the energy barrier over the patches would be reduced enough to allow deposition on the patches. This situation is analogous to “salting out” of colloidal dispersions by increasing ionic strength to reduce the energy barrier between particles leading to aggregation and settling. In this case however, the decreasing energy barrier comes from a combination of the lower energy barriers from increased ionic strength (increased double layer screening) and the smaller ZOI size forcing the particle to see more of a single attractive patch. When $f_{p,zoi}$ become large enough, the energy barrier will be reduced sufficiently to facilitate particle deposition.

5.4.7 The effects of boundary conditions and variable surface potentials

The previous calculations for the DLVO interaction with patchy surfaces have calculated electrostatic interactions with an analytical approximation for the electrostatic double layer interaction that assumes constant potential boundary conditions. However, the linear mixing approximation allows numerical solutions for the Poisson-Boltzmann equation to be used together with constant potential (CP) or constant charge (CC) boundary conditions easily. Benefits of using the numeric solutions based on the full Poisson-Boltzmann equation as opposed to approximate analytical expressions are two-fold: 1) the effects of the boundary conditions can be incorporated into calculations, and 2) numerical solutions provide greater accuracy for surfaces at high surface potentials (or surface charge densities) when solutions based on the linearized Poisson-Boltzmann equation are not as accurate (surface potentials greater in magnitude than $\sim 25\text{mV}$). Furthermore, more complex boundary conditions, such as charge regulation could be included in the analysis to model real systems better.¹²⁵

Like with analytical expressions, implementation of full numerical solutions to the Poisson-Boltzmann equation is used with the linear mixing approximation for patchy surface by performing two calculations: one for the particle-bulk homogeneous interaction energy and one for the particle-patch homogeneous interaction energy. Until now, we have looked at DLVO interaction energies but surface forces can be calculated as well.

Figure 5.12 provides an example of DLVO interaction energy and force normalized by the radius of curvature for a particle of radius $0.5 \mu\text{m}$ using full numerical solutions of the Poisson-Boltzmann equation under constant potential and constant charge boundary conditions. The interaction of the particle with the (homogeneous) patch surface is denoted as $f_{p,zoi} = 100\%$ and bulk surface is denoted as $f_{p,zoi} = 0\%$. The electrolyte is a 1mM 1:1 electrolyte solution with $\kappa^{-1} = 9.6 \text{ nm}$. The surface potentials (at large separation for the constant charge case) are $\psi_{\text{patch}} = +50\text{mV}$ and $\psi_{\text{bulk}} = \psi_{\text{particle}} = -50\text{mV}$. The Hamaker constant is $A_H = 0.5 \times 10^{-20} \text{ J}$.

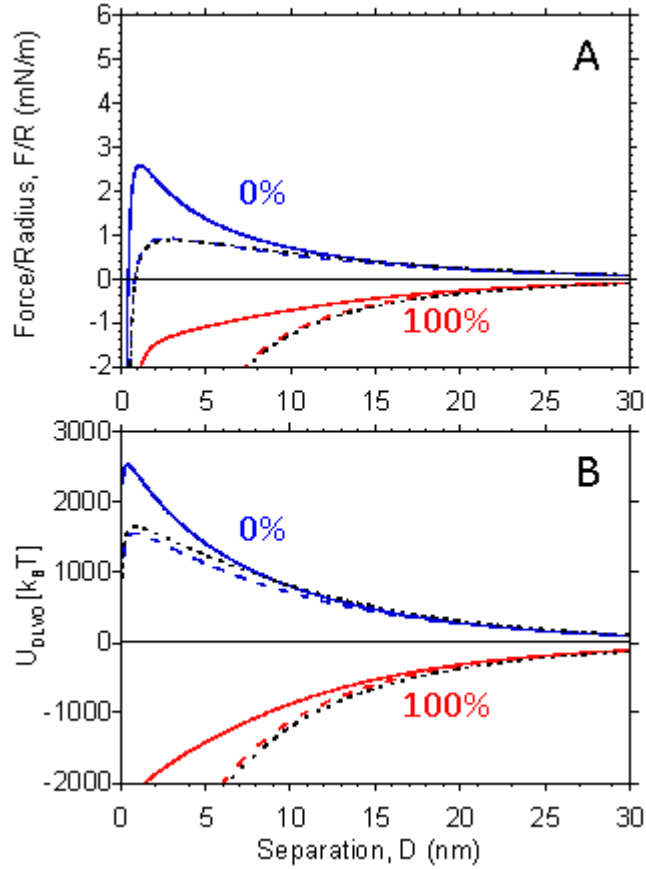


Figure 5.12: a) DLVO interaction force normalized by particle radius ($a=0.5 \mu\text{m}$) and b) DLVO interaction potential for constant charge (solid lines) and constant potential (dashed line) boundary conditions for homogeneous surfaces given as percent patch. 0% (blue) corresponds to only bulk surface and 100% (red) corresponds to only patch surface. The HHF expressions are also shown as dotted black lines for comparison. $\Psi_{\text{bulk}} = \Psi_{\text{particle}} = -50\text{mV}$, $\Psi_{\text{patch}} = +50\text{mV}$, $\kappa^{-1} = 9.6 \text{ nm}$, $A_H = 0.5 \times 10^{-20}\text{J}$

The interaction energies and forces for the homogeneous surfaces shown in figure 5.12 can be used to calculate interactions with patchy surfaces vs. $f_{p,zoi}$ by employing the linear mixing approximation. Figure 5.13 shows the calculated interaction potentials for $f_{p,zoi} = 25\%$, 50% , and 75% .

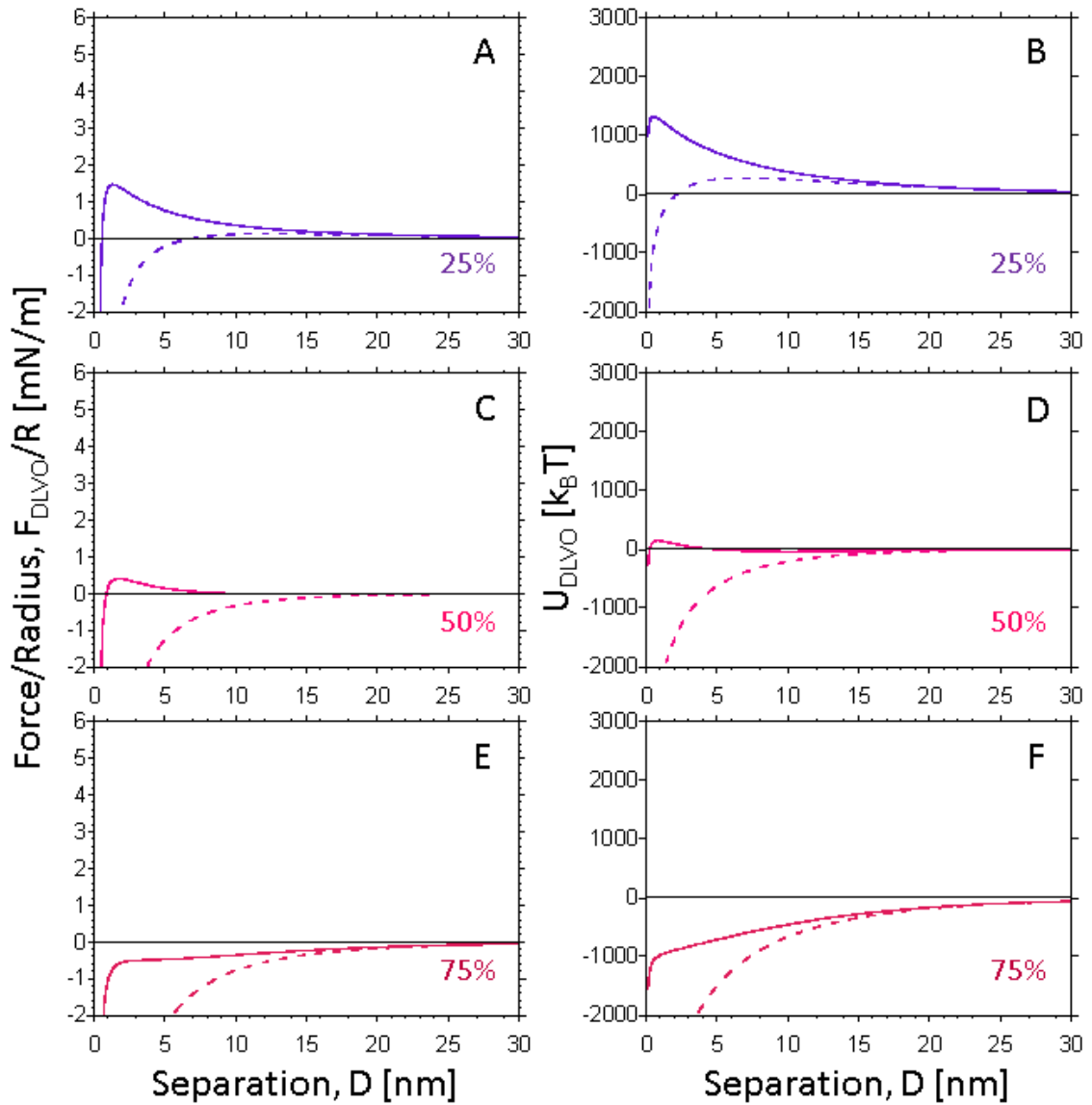


Figure 5.13: a) DLVO Interaction potential and b) force normalized by particle radius of curvature for constant charge (solid lines) and constant potential (dashed line) boundary conditions. A,B) 25% coverage, C,D) 50% coverage, E,F) 75% coverage $\psi_{\text{bulk}} = \psi_{\text{particle}} = -50\text{mV}$, $\psi_{\text{patch}} = +50\text{mV}$, $\kappa^{-1} = 9.6 \text{ nm}$ $A_H = 0.5 \times 10^{-20} \text{ J}$

In Fig. 5.13, a few general trends can be observed. First, the repulsive force (A,C,D) and energy of interaction (B,D,F) for the constant charge case are always higher

at all coverages. In the case of 50% patch coverage (Fig. 5.13C and 5.13D), repulsion is observed in the constant charge case but not the constant potential case. If the surface obeys the constant charge boundary condition, particles will still experience a repulsive force while they will experience purely attractive interactions for the constant potential case. This indicates that the boundary conditions can have a dramatic effect on particle–surface interactions. Repulsion may be predicted for a given patch coverage with constant charge conditions and attraction may be predicted under constant potential boundary conditions. Further, it is important to remember that real surfaces generally do not obey either the constant charge or constant potential boundary conditions.¹²⁶ Instead, charge regulation occurs during particle approach and net interaction will fall somewhere between the calculated constant charge and potential boundary conditions.¹²⁵ This implies minor deviations from either boundary condition could cause particle interactions to switch from being either attractive or repulsive.

5.4.8 Estimating critical patch coverage for arbitrary surface potential and boundary conditions

Using the linear mixing approximation with known solutions for the DLVO interactions, it is possible to estimate a critical patch surface coverage for patches in the zone of influence for a given particle radius and set of boundary conditions. The critical patch coverage is the coverage when the predicted repulsive energy barrier becomes less than a critical value (typically taken as $\sim 10k_B T$ when considering the stability of colloidal suspensions). Therefore, the critical patch coverage, $f_{p,\text{critical}}$ is defined as:

$$U_{DLVO,net,max}(f_{p,critical}) \leq \sim 10k_B T \quad (5.22)$$

The value of the critical patch coverage, $f_{p,critical}$, will depend on particle size, ionic strength, and the surface potentials and boundary conditions applied to the particle, bulk, and patch surfaces.

Figure 5.14A shows the critical patch coverage for a 0.5 μm radius particle versus boundary condition and surface potential (reported at large separation for constant charge case) for the using the same Debye length and Hamaker constant as Fig. 5.12 and Fig. 5.13. The surface potential for the particle and bulk are identical and equal in magnitude but opposite in sign to the patch surface potential (patch surface potential is set to the positive surface potential reported on the horizontal axis).

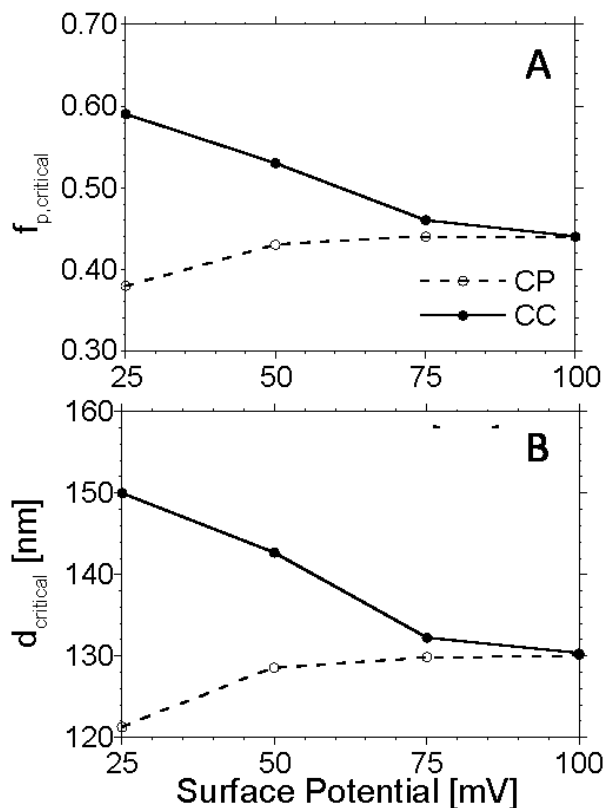


Figure 5.14 A) critical patch coverage versus the magnitude of the surface potential (at infinite separation) for the constant charge and constant potential boundary conditions ($\Psi_{bulk} = \Psi_{particle} = -\Psi_{patch}$) ($a=0.5$, $\kappa^{-1} = 9.6$ nm $A_H = 0.5 \times 10^{-20}$ J) B) Critical single patch diameter versus the magnitude of the surface potentials

In Fig. 5.14A, the critical patch coverage is always higher for the constant charge case but the two approach each other as the magnitude of the surface potential increase. The critical patch coverage for both constant charge and constant potential cases approach the same value as the magnitude of the surface potential increases, with the constant charge critical patch coverage decreasing with increasing magnitude of the surface potential and the constant potential case increasing with increasing magnitude of

the surface potential. One would expect that using charge regulation conditions would result in a coverage falling between the bounds set by the CC and CP cases.

The critical patch coverage can be used to estimate a minimum diameter, $d_{critical}$, for a single patch to capture a particle of a given size:

$$d_{critical} = \sqrt{8a\kappa^{-1}f_{p,critical}} \quad (5.23)$$

Equation 5.23 solves for the area of a single patch necessary to achieve the critical patch coverage in the ZOI (using the ZOI-1 argument of eqn. 5.17). The results of this analysis are shown in shown in figure 5.14B and follow the same trends as 5.14A. Once again, a charge regulation model will fall between the CP and CC limits. This analysis can be extended to other particle radii as well, as shown in Table 5.2 for 0.25 μm and 1.00 μm radii particles. The same general trends occur at other particle radii with the critical patch coverage being nearly identical regardless of particle radius for both CC and CP boundary conditions. However, the critical single patch size increases with particle radius, as should be expected with the increasing size of the ZOI.

Table 5-2: Critical patch coverage and single patch size estimates for particles of different radii and surface potentials ($\kappa^{-1} = 9.6$ nm, $\psi_{\text{Particle}} = \psi_{\text{Bulk}} = -|\psi|$, $\psi_{\text{Patch}} = |\psi|$) with CP and CC boundary conditions

a (μm)	r'zoi (nm)	ψ (mV)	f_{p,critical} (CP)	f_{p,critical} (CC)	d_{critical} (CP) (nm)	d_{critical} (CC) (nm)
0.25	138.6	25	0.35	0.58	82.0	105.3
		50	0.41	0.53	88.9	100.7
		75	0.42	0.45	90.1	93.4
		100	0.43	0.43	90.4	90.6
0.50	196.0	25	0.38	0.59	121.3	150.0
		50	0.43	0.53	128.6	142.7
		75	0.44	0.46	129.9	132.3
		100	0.44	0.44	130.2	130.3
1.00	277.1	25	0.40	0.59	176.3	212.9
		50	0.44	0.53	184.5	202.0
		75	0.45	0.46	186.0	187.1
		100	0.45	0.45	186.4	186.5

5.5 Conclusions

This chapter has outlined a simple linear mixing approximation to estimate particle-surface interaction forces and energies for surfaces containing discrete surface charge heterogeneities. This method is based on the work of Bendersky and Davis^{45, 119} and the zone of influence argument described throughout the literature^{19, 41, 43, 44, 120, 121}. It allows for relatively simple calculation of net heterogeneous surface interactions from the independent homogenous interactions of the patch and bulk surfaces. These homogeneous interactions can come from approximate analytical solutions for electrostatic interactions, allowing for a fully analytical approach to calculating patchy surface interactions or solutions based on numerically solving the Poisson-Boltzmann

equation, which allows calculation at high surface potentials and arbitrary boundary conditions. The linear mixing approximation outlined in this chapter and its comparison to published results from the GSI technique carry several implications for patchy surface interactions that can be summarized as follows:

- 1) The ZOI argument based on a single Debye (ZOI-1: $r'_{zoi} \cong \sqrt{2a\kappa^{-1}}$) allows the linear mixing approximation to provide comparable interaction predictions to GSI solutions. This observation is based on comparing predictions from linear mixing approximation to full GSI solutions published in literature for the case of a particle interacting with a single patch.
- 2) The ZOI size does not change significantly with separation for large particles. This means that $f_{p,zoi}$ will be a fixed value for all separations and depend only on a particle's lateral position on a surface.
- 3) Results from the linear mixing approximation match solutions from the full GSI technique when many small patches are distributed within the ZOI. If the homogeneous patch and bulk surface interaction energies, $U_{Bulk}(D)$ and $U_{Patch}(D)$, are calculated, the net interaction energy for a particle approaching a patchy surface can be easily calculated based on the patch surface coverage, as was observed by Bendersky and Davis.¹¹⁹ If approximate analytical expressions are used to calculate the patch and bulk interaction energies, the linear mixing approximation provides a fully analytical approach to calculating patchy surface interaction forces or energies.

4) When applied to a single patch within the ZOI (using ZOI-1), the linear mixing approximation provides interaction potentials that are comparable to GSI solutions. This allows the linear mixing approximation to be used as a simple method of quickly estimating critical patch sizes. Further, the transition between the many patch regime and single patch regime can occur by increasing ionic strength of the system. (Fig. 5.11) and the same approximation can be used to provide estimates for a fixed patch layout at different ionic strengths.

5) Full numeric solutions to the Poisson-Boltzmann equations with arbitrary boundary conditions applied to the surfaces can be easily incorporated in linear mixing approximation. It was shown that the boundary conditions can have significant influence on the interaction forces and energies for a particle approaching a patchy surface, with attractive behavior under constant potential boundary conditions and repulsive behavior under constant charge boundary conditions (Fig. 5.14) Critical patch coverages can be calculated for the different boundary conditions as well (Table 5-2). Interactions with surfaces obeying charge regulation boundary conditions are expected to fall between the constant potential and constant charge boundary conditions.¹²⁶

It is important to remember that the predictions made in this chapter have ignored the effects of hydrodynamic interactions on particle deposition behavior. Further, the analysis was limited here to ordered arrays of charge heterogeneities. Such ordered arrays of heterogeneities only serve as an approximation of randomly distributed heterogeneities. Finally, the Hamaker constant was assumed to be uniform for the

surface, which may not be true for heterogeneous surfaces. However, the linear mixing approximation provides a facile method of estimating DLVO interaction from homogeneous particle-patch and particle-bulk interaction forces and energies. By employing more complex solutions for the homogeneous surface interactions based on full numeric solution of the Poisson-Boltzmann equation, the effects of different boundary conditions can be incorporated into estimates particle interaction energies and forces for patchy surfaces. For surfaces with many small heterogeneous patches compared to the size of the ZOI, we would expect excellent agreement with full GSI solutions and the ability to incorporate arbitrary boundary conditions allows for better predictions for interaction forces and energies for real colloidal systems.

Chapter 6 Direct force measurement with patterned surface charge heterogeneities

6.1 Introduction

Artificially patterning surfaces allows for precise control of interfacial properties through both surface chemistry and pattern geometry. Surface patterns can be used to modulate wetting properties^{127, 128}, direct biological processes and cell morphology on surfaces^{129, 130}, or allow for spatially controlled particle deposition^{131, 132}. Control over particle deposition in particular has numerous implications for designing high-specificity surfaces for sensors^{133, 134} and “bottom-up” assembly processes^{13, 14, 15}. Patterned surface charge heterogeneities are one method of controlling particle deposition behavior.^{14, 16, 19, 20, 21, 22, 23} Surface charge heterogeneities can modify electrostatic interactions and produce attractive regions for particle deposition to occur on an otherwise repulsive surface.

Numerous studies have investigated the effects of surface charge heterogeneities on particle-surface interactions.^{4, 16, 20, 38, 41, 43, 44, 45, 46, 119, 121, 122, 135} These studies are largely based on computational methods and experimental studies measuring particle deposition rates on surfaces bearing heterogeneities. However, the direct force measurement of interaction forces with heterogeneously charge heterogeneities has

remained a largely unexplored method of studying the effects of charge heterogeneity on colloidal interactions.^{41, 50}

There are primarily two techniques available for directly measuring surface forces. These techniques are the colloidal probe technique and the surface forces apparatus (SFA). The colloidal probe technique uses an atomic force microscope (AFM) to measure the interaction forces between a spherical probe with a radius of approximately 1-10 μm ¹³⁶ attached to the end of a AFM cantilever. The force-separation profiles are measured between this probe and a flat surface. In contrast, the SFA technique consist of two mica surfaces arranged in a crossed cylinder geometry. This geometry is geometrically equivalent to a sphere interacting with a flat plate.⁶⁹ The radius of curvature of these surfaces is 1-2cm and the surface separation is obtained from multiple beam interferometry (MBI)⁶⁸ by analyzing the wavelength of fringes of equal chromic order (FECO).^{62, 63, 72} This provides the data on the absolute surface separation with sub-nanometer resolution.

The SFA and colloidal probe technique have both been applied in studies of chemically heterogeneous surfaces. For example, the SFA has been used to measure the interactions between two surfaces covered in disordered charge heterogeneities formed from the rearrangement of cationic surfactant layers on mica.^{137, 138} A long-range attraction was observed between the surfaces that the authors ascribed to correlation between positive and negatively charged domains on each surface.¹³⁷ However, such a system provides little control over the size of the charge heterogeneities present and the interaction is between two heterogeneous surfaces, instead of a single heterogeneous

surface. Likewise, the colloidal probe technique has been used by Kokkoli and Zukoski to study the interaction of silica probes with patterned hydrophobic and hydrophilic stripes.⁵⁰ The results of Kokkoli and Zukoski suggested that hydrophobic-hydrophilic interactions were non-additive.⁵⁰ Finally, the AFM has been used to map the surface charge variation on surfaces in a process referred to as surface charge mapping.^{139, 140, 141, 142} In surface charge mapping, the AFM tip is typically the same size or smaller than the charge heterogeneities and does not measure a net interaction of the heterogeneities and surrounding surface, as can occur when a particle approaches a heterogeneously charged surface.

A thorough study of the effects of charge heterogeneities on surface forces requires precise control of the size and surface coverage of the heterogeneities. In order to fully investigate interactions with heterogeneously charged surfaces it is necessary to pattern several heterogeneities within the effective electrostatic interaction area. Prior work based on computational methods and particle deposition experiments have determined the scaling of this interaction zone, referred to as the electrostatic zone of influence or ZOI^{19, 44, 45, 121, 143}. The radius of the electrostatic zone of influence, r_{zoi} , is approximately $\sqrt{2a\kappa^{-1}}$, where a is the radius of curvature of the surface and κ^{-1} is the Debye length.¹⁹ Systematic investigation of surface forces with charge heterogeneities requires the fabrication of well-defined charge heterogeneities much smaller than the electrostatic zone of influence. If charge heterogeneities are larger than the ZOI, a homogeneous interaction based on the surface potential of the heterogeneity will be obtained (i.e. only the heterogeneous surface and not a combination of the heterogeneity and surrounding

surface will contribute the measured interaction force). Therefore, the electrostatic zone of influence provides a maximum size for patterned charge heterogeneities and it is necessary to fabricate surface patterns much smaller than this interaction area.

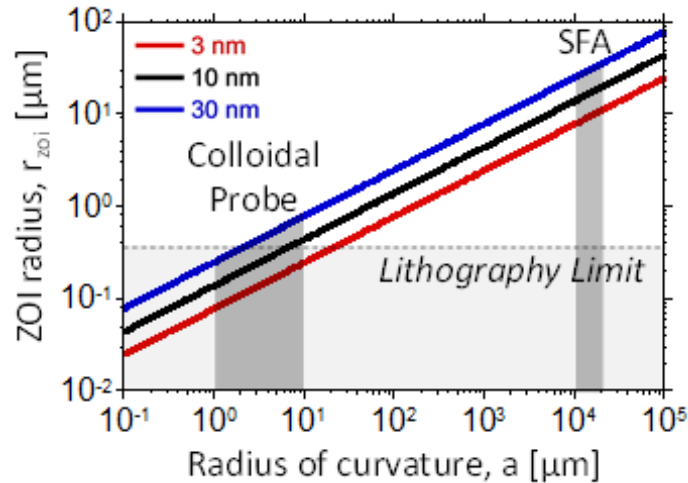


Figure 6.1 Comparison of zone of influence radius (r_{zoi}) to the radius of curvature of the surface/probes used in the SFA and colloidal probe techniques for three different Debye lengths ($\kappa^{-1} = 3\text{nm}$, 10nm , and 30nm). The dark highlighted regions show the corresponding radii of curvature for the SFA (1-2cm) and colloidal probe (1-10 μm) techniques. The resolution limit of i-line lithography (365nm) is highlighted showing the regions accessible to microfabrication of heterogeneously charged features.

Figure 6.1 shows the radius of the zone of influence versus the interacting surface's radius of curvature for three different Debye lengths ($\kappa^{-1} = 30\text{ nm}$, 10 nm , 3 nm corresponding to $\sim 10^{-4}$, 10^{-3} , and 10^{-2} M 1:1 electrolyte solutions). The relevant radii of curvature for both the colloidal probe technique (1-10 μm) and the SFA (1-2 cm) are highlighted. The radius of curvature changes the size of the ZOI and as a result, the necessary pattern dimensions required for fabricating charge heterogeneities. For the colloidal probe technique, the radius of the ZOI is approximately 0.1-1.0 μm , while for

the SFA it is on the order of approximately 10-100 μm . To fully investigate heterogeneous surface interactions, several heterogeneous “patches” must be patterned within the interaction area. However, there are practical limits to the resolution (minimum resolvable feature size) of optical lithographic techniques.^{144, 145} In optical lithography, the resolution is generally limited to the same size as the exposure wavelength used.¹⁴⁵ The dashed line in figure 6.1 shows the minimum resolution possible using the i-line exposure wavelength (365nm).¹⁴⁵ The i-line is a spectral line from a mercury arc lamp and is commonly used in photolithographic systems. While other lithographic techniques are available utilizing shorter exposure wavelengths¹⁴⁶ or switching to electron beam (e-beam) lithography^{145, 147} these techniques add additional cost and complexity to surface fabrication processes. The surface forces apparatus, because of its large radius of curvature drastically increases the size of the interaction area and allows for interrogation of heterogeneities over a much larger range of length scales that are essentially inaccessible to the colloidal probe measurements. The SFA also has the added benefit of providing absolute surface separations and in situ imaging of the interaction area from the FECO. This allows the radius of curvature of the interacting surfaces to be measured during the experiment.

This chapter presents results from the direct measurement of interaction forces between micropatterned heterogeneously charged surfaces and plain mica in the surface forces apparatus. The patterns are fabricated from the chemical vapor deposition of 3-aminopropyltriethoxysilane (APTES) through elastomeric masks and consist of an array of well-defined positively charged patches over a negatively charged mica surface.⁵¹ Two

different scaling regimes of the patches compared to the electrostatic zone of influence are investigated: a single small heterogeneity within the zone of influence and multiple heterogeneities in the zone of influence. The force profiles were found to be intermediate between a mica-mica and mica-APTES. The measured force profiles are compared to the linear mixing approximation of chapter 5 and also fitted for an effective surface potential of the patterned surface. The fitting procedure is shown to be dependent upon the boundary conditions applied to the surfaces when numerically solving the Poisson-Boltzmann equation. It is shown that the effective surface potential cannot be predicted from the patch coverage and surface charge densities of the patch and mica surfaces, in agreement with observations published in literature from computational studies and electrokinetic measurements. General agreement with the linear mixing approximation is shown and spatially-independent behavior in the many patch regime is found where multiple locations on the surface generate the same net interaction force profile.

6.2 Materials and Methods

6.2.1 Materials

Elastomer (Dow Corning Sylgard® 184) is purchased from Robert McKeown Inc. (Branchburg, NJ). SU-8 2025 photoresist and developer are purchased from Microchem Corp. (Newton, MA). 3-aminopropyltriethoxysilane (APTES) 98%, tridecafluoro-1,1,2,2-tetrahydrooctyl trichlorosilane, semiconductor grade isopropyl alcohol, and potassium hydroxide (99.99%) are purchased from Sigma-Aldrich (St. Louis, MO). Mica (Ruby,

ASTM V-1/2) is purchased from S&J Trading (Glenn Oaks, NY), and hydrochloric acid (Fisher Chemical, OPTIMA grade) is diluted with deionized water to a concentration of 10^{-4} M. Fluorescent carboxylic acid-functionalized particles (diameter = 110nm) are purchased from Bang's Laboratories (Fishers, IN). Unless mentioned otherwise, all chemicals are used as received.

Membrane Preparation

The elastomeric membranes used to generate the APTES patterns for SFA experiments are fabricated by a spin-coating procedure onto a micropillar array template in a process adapted from Jackman et al.⁹⁸ The template is fabricated from SU-8 2025 on a silicon wafer following standard photolithography procedures (more details located in Appendix). Following fabrication, the template is treated with an anti-adhesion layer of tridecafluoro-1,1,2,2-tetrahydrooctyl trichlorosilane in a vacuum desiccator for 1 hour at room temperature. This fluorosilane layer was found to help facilitate lift-off of the PDMS elastomer in subsequent steps.⁹⁸

After fabrication of the micropillar array templates, Sylgard® 184 elastomer, mixed in a ratio of 10:1 base to curing agent, is spin-coated onto the template, ensuring a sufficient spin-speed for through-holes to be formed in the membrane. After spin-coating, the elastomer is cured in an oven for 48 hours at 70°C. Once cured, the membranes are removed from the template by cutting the periphery of the membranes with a razor and carefully peeling the membrane off the template with tweezers. An extraction procedure is performed to remove any unreacted PDMS oligomers from the membrane material.¹⁰⁰ The extraction consists of a 48 hour immersion of the membranes in hexanes with gentle

agitation via a magnetic stir bar. After extraction is completed, the membranes are dried overnight in a vacuum oven at a temperature of 70 °C to remove the hexane from the membranes. Once dried, the membranes are removed from the vacuum oven and cleaned via ultrasonication in semiconductor grade isopropyl alcohol for 3 times at 5 minutes each. After this final cleaning step, the membranes are dried again overnight in a vacuum oven at 70°C. It was found that freshly cleaved mica serves as an excellent substrate to support the membranes during this final drying step and subsequent storage until use.

Just before the membranes are used for the vapor deposition process, they are treated on their top side with an oxygen plasma treatment for 1 minute at a pressure of 0.3 Torr and 50W of power. This treatment is conducted within 30 minutes of preparation of the SFA substrates and forms a barrier layer to block APTES diffusion into the elastomer material. Additionally, it was found that plasma treating the membranes on a curved substrate with a radius of curvature matching the final SFA surfaces (~2cm) helped improve the integrity of the plasma-generated barrier layer for patterning curved substrates.

Surface preparation. For the patterned surfaces used in in the SFA, 3-5 μm thick mica pieces are cleaved in a laminar hood and placed on a larger backing sheet. The cleaved mica pieces are coated with 50 nm of silver (99.999% purity, Alfa Aesar) via thermal evaporation (Kurt J. Lesker Nano 38) at a rate of 2-3 Å/s. The mica pieces are then glued (on the silvered side) onto a silica support disk for the SFA. For patterning, the extracted and plasma-treated membranes are applied directly to glued mica surfaces. The membranes are applied plasma-treated side up. Further, the orientation of the plasma

treated membrane's curvature is matched to the mica substrates. It was also found that pre-applying the membranes to sheets of freshly cleaved mica ~3-5 times prior to applying to the SFA substrates helped remove any particulate that may be present on the membranes from the fabrication and extraction steps. This "blotting" of the membranes helps prevent the transfer of any possible particulate contaminants from the membrane to the underlying mica surface.

In order to verify successful APTES patterning, two substrates are prepared simultaneously. One surface is used for force measurements in the SFA. The other surface, referred to as a "twin surface", is tagged with negatively charged fluorescent nanoparticles after APTES deposition to verify successful APTES deposition and characterize the pattern dimensions prior to performing force measurements. Following application of the elastomeric membranes to the mica surfaces, the SFA and twin surfaces are both placed in a vacuum desiccator (Scienceware® vacuum desiccator, internal volume 2L) and moved to a glove bag (Aldrich® Atmosbag). The desiccator is evacuated for 30 minutes with a mechanical vacuum pump then sealed under vacuum. The glove bag is purged with high purity nitrogen 3-5 times to remove any traces of moisture from the setup. Then, the vacuum is broken on the desiccator in the dry nitrogen atmosphere and a dish of APTES (1.25 μ L APTES per liter internal desiccator volume) is placed in the desiccator. The desiccator is then pumped down for 1 minute with the vacuum pump and sealed for the APTES vapor deposition. A total deposition time of 4 hours was used here. After deposition, the desiccator is purged with nitrogen and the dish of APTES is removed. The desiccator is taken out of the glove bag and the membranes are carefully

lifted off the mica substrates with tweezers. Then, the substrates are rinsed with 200 proof ethanol and dried with filtered nitrogen. At this point, the substrates are ready to be used. The SFA substrate is placed inside the instrument while the twin surface is tagged with fluorescent negatively charge carboxyl-functionalized nanoparticles to verify successful patterning via fluorescence imaging.

Fluorescence Imaging. Surfaces are tagged by soaking them for 30-45 minutes in a 10^{-5} volume fraction solution of carboxyl-functionalized fluorescent particles dispersed in deionized water (18.2 M Ω -cm). Following soaking, the surfaces are rinsed with deionized water and dried with nitrogen. Fluorescence images of the tagged surfaces are taken with an Olympus BH-2 microscope equipped with a Tucsen 3.3MP CCD camera. TSview version 6 is used for image capture. Pattern dimensions and area coverage are measured using ImageJ 1.46r. Coverage is determined by converting the fluorescent images to binary format in ImageJ and measuring the area coverage using the built-in particle analyzer.

Surface Forces Apparatus (SFA) experiments. The MK II SFA⁶⁹ equipped with microstepping motors is employed to measure the interaction forces between the APTES patterned surfaces and a sheet of freshly cleaved mica (of the same thickness as the patterned mica sheet) in aqueous electrolyte solutions. In the SFA, the surface separation is estimated from the position of the fringes of equal chromatic order (FECO)⁷¹ resulting from multiple beam interferometry (MBI).⁶⁸ The wavelengths at the vertex of the parabolic fringes are used to estimate the surface separation at the point of closet approach for a sphere-plane configuration. To determine surface separation we use the

multilayer matrix method¹⁰¹ combined with the fast spectral correlation algorithm.^{72, 102} The interaction between the two crossed-cylinders is calculated from the deflection of a soft cantilever spring ($k = 118.3\text{N/m}$). The radius of curvature, $R = \sqrt{R_1 R_2}$ is determined from the geometric mean of two spatially resolved FECO profiles coming from perpendicular cross-sections.

Cleaning. All stainless steel parts that come into contact with electrolyte (spring, upper, and lower disk holder) are cleaned in an RBS 35 (Pierce, Rockford, IL) detergent solution, passivated in 50% nitric acid, rinsed thoroughly with ethanol, and dried immediately before use. All of the Teflon parts (bath, tubing assembly) are cleaned in a detergent solution, rinsed thoroughly with water, and dried with nitrogen immediately before use. All glassware is cleaned with detergent, and rinsed with water.

Procedure. A Teflon bath is employed inside the SFA chamber and 25 mL of the electrolyte solution is injected while the surfaces are separated using a syringe equipped with all Teflon tubing and valves. The solution is left in the apparatus for 1-2 h for equilibration prior to force measurements. Each force profile (approach and retraction) is repeated at least 5 times. All experiments were performed at 23 °C.

Double layer interactions. When fitting for an effective surface potential for the patterned surfaces, measurement of double layer forces and their comparison with DLVO (Derjaguin-Landau-Verwey-Overbeek) theory is used to interpret the force data for the patterned surfaces. DLVO theory^{32, 35, 58} describes the interaction between two flat surfaces in an electrolyte solution as the superposition of the van der Waals and

electrostatic interaction energies. We calculate the electrostatic interaction energy from the excess pressure in the gap, calculated by solving numerically the full Poisson-Boltzmann equation for both constant potential and constant charge boundary conditions using MATLAB's boundary value problem solver (bvp5c), and the electrostatic interaction energy is obtained from a numerical integration of the pressure. (Additional details in chapter 2.2.3) Hamaker theory is used for the non-retarded van der Waals interactions with a Hamaker constant of $2.2 \times 10^{-20} \text{J}^{103}$ for the interactions between mica surfaces in aqueous solutions. Finally, we employ the Derjaguin approximation to convert the interaction energy between flat surfaces to the forces normalized by the radius of curvature between crossed-cylinders. In comparing to DLVO theory, the measured forces were fitted for a surface potential. The Debye length is calculated for a 1-1 electrolyte using: $\kappa^{-1} = \sqrt{\epsilon_0 \epsilon_r kT / 2e^2 n_b}$, where n_b is the bulk ion concentration, k is Boltzmann constant, T is temperature, ϵ_0 is the permittivity of free space, ϵ_r is the relative permittivity of the solution. Unless otherwise noted, the Debye length used is the expected value based on the ionic strength of the prepared aqueous solutions.

6.3 Results and Discussion

6.3.1 Homogeneous surface interactions

The micropatterned surfaces used in the SFA are fabricated by performing a chemical vapor deposition of an aminosilane (3-aminopropyltriethoxysilane, APTES) directly onto prepared mica substrates.⁵¹ This process creates well-defined

micropatterned patches of APTES monolayers with minimal topographical variation. Minimizing topographical variation helps ensure that only the effects of charge heterogeneities and not topography are being investigated. APTES monolayers create positively charged heterodomains on a negatively charged bulk surface (mica) when immersed in aqueous electrolyte solutions. When the opposing surface is mica, this means that the interaction is repulsive for mica-mica and attractive for the APTES patches (APTES-mica).

Characterization of homogeneous mica and APTES surfaces provides values for the surface potentials and surface charge densities of the mica and APTES surfaces at the electrolyte conditions employed. Figure 6.2 shows the mica-mica, APTES-mica, and APTES-APTES interactions for the homogeneous (unpatterned) surfaces and Table 6.1 lists the fitted surface potentials and surface charge densities.⁵¹ Figure 6.2 includes fits of the data from numerical solutions of the Poisson-Boltzmann equation for constant charge and constant potential boundary conditions. The homogeneous mica-mica surfaces more closely follow constant potential (CP) boundary conditions and APTES surfaces tend to obey constant charge (CC) boundary conditions. Additionally, adhesion forces for measured for mica-mica, APTES-mica, and APTES-APTES surfaces and presented in Table 6-1. In contact, mica-mica and APTES-APTES (denoted as symmetric) are both adhesive. The mica-APTES surfaces are strongly adhesive due to the oppositely charged surfaces.

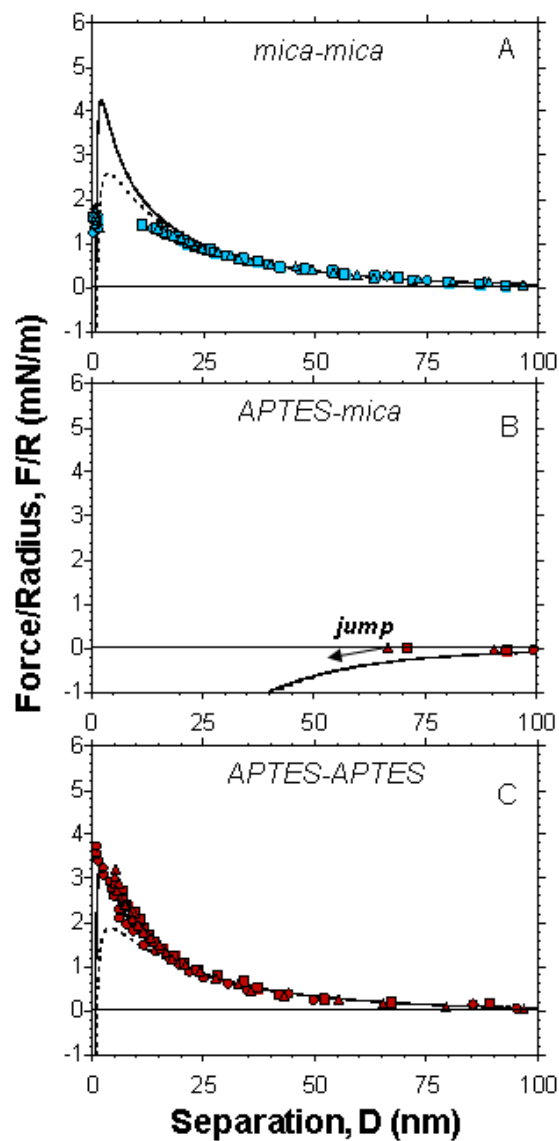


Figure 6.2 Force normalized by radius of curvature for A) mica-mica surfaces B) APTES-mica C) APTES-APTES surfaces in a 10^{-4} M HCl solution. Solid lines show fit with constant charge boundary conditions and dashed lines shows fit with constant potential boundary conditions applied to both surfaces.

Table 6-1 Fitted APTES and mica surface potentials, surface charge densities, and measured adhesive forces obtained from homogeneous surface interactions.

	Debye length, κ^{-1} (nm)	Surface potential, Ψ_s (mV)	Surface charge density, σ (e/nm^2)	$-F_{adh}/R$ (APTES-mica) mN/m	$-F_{adh}/R$ (symmetric) mN/m
Mica-Mica	30.9 ± 0.8	-120 ± 5	-0.038 ± 0.004	N/A	28.9 ± 2.3
APTES-APTES	30.0 ± 0.8	110 ± 6	0.032 ± 0.004	77.1 ± 8.0	1.5 ± 0.9

6.3.2 Single patch in the zone of influence

There are three possible regimes for the size of heterogeneous APTES patches compared to the electrostatic zone of influence: 1) patches much larger than the ZOI, 2) patch of approximately the same order as ZOI such that only one domain is present in the ZOI at a time, or 3) patches much smaller than the ZOI. In the case of a patch much larger than the ZOI, it would be expected that a homogeneous interaction would be obtained. However, when the patches are smaller than the ZOI, the approaching mica surface interacts with both the APTES patch(es) and the mica surrounding them, generating a net force that is a combination of APTES-mica and mica-mica interactions.

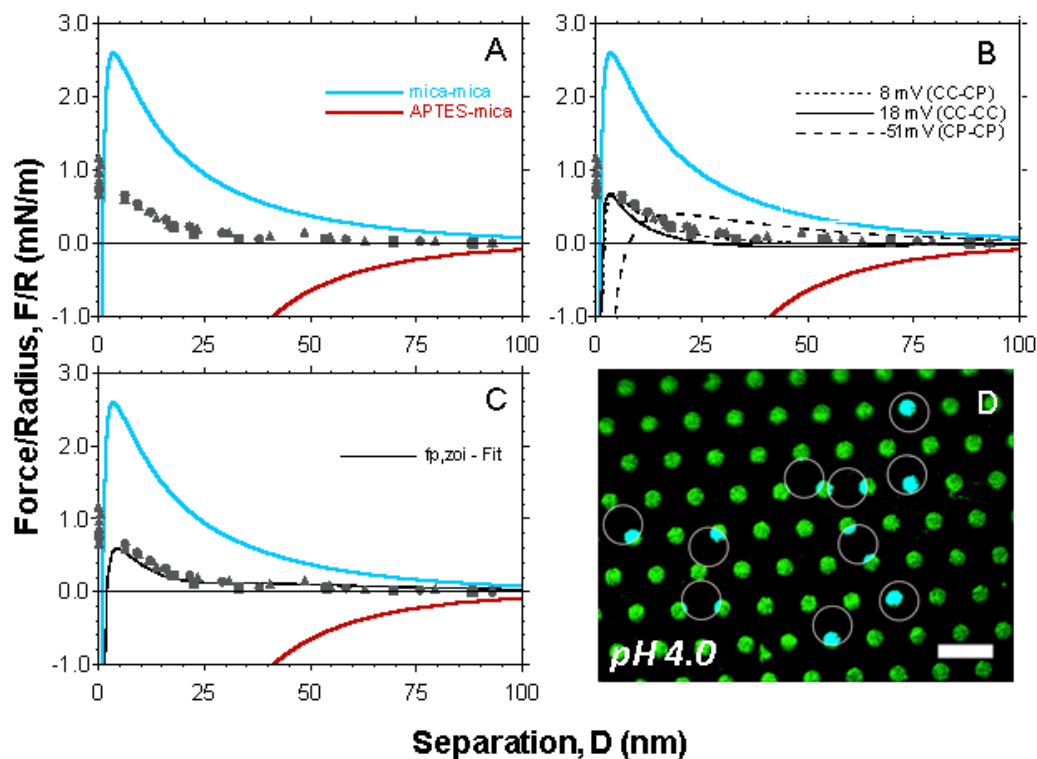


Figure 6.3 A) Force normalized by radius of curvature of between a APTES patterned mica surface (APTES patches $26.9 \pm 1.1 \mu\text{m}$ diameter, $48.6 \pm 2.6 \mu\text{m}$ edge-to-edge spacing) and mica in 10^{-4} hydrochloric acid ($\kappa^{-1} = 31 \text{ nm}$) over multiple approaches, indicated by different symbols. Blue shows expected mica-mica interaction and red APTES-mica interaction B) Fit through points for a nominal surface potential of patterned surface with CC-CP, CC-CC, and CP-CP boundary conditions for the patterned and mica surface respectively, C) fit for effective patch coverage based on linear mixing approximation, $f_{p,zoi} = 26\%$) Fluorescence image of twin surface showing expected ZOI ($r_{zoi} = 35.2 \mu\text{m}$) randomly distributed over surface. The patch surface coverage is $f_p = 11.5 \pm 0.8\%$ for the entire surface from image analysis. Scale bar = $100 \mu\text{m}$.

By properly scaling the heterogeneities to the ZOI based on the radius of curvature of the SFA surfaces and Debye length, it is possible to investigate both the case of a single patch and many patches in the zone of influence. Figure 6.3A shows the measured interaction force vs. separation between a micropatterned surface and a plain

sheet of mica in 10^{-4} M hydrochloric acid. The APTES patches dimensions are: diameter = $26.9 \pm 1.1 \mu\text{m}$, edge-to-edge spacing = $48.6 \pm 2.6 \mu\text{m}$, patch surface coverage, $f_p = 11.5 \pm 0.8\%$. Figure 6.3A also shows the expected homogeneous (mica-mica and APTES-mica) interactions. The surface potentials and boundary conditions applied to the mica and APTES surfaces are: $\Psi_{\text{mica}} = -120\text{mV}$, constant potential (CP) boundary condition and $\Psi_{\text{APTES}} = +110\text{mV}$, constant charge (CC) boundary condition.

Fig. 6.3A shows that the measured force profile between the micropatterned surface and mica is intermediate between the mica-mica and APTES-mica interactions. This suggests the net interaction arises from the contribution of both the patch (APTES-mica) and the surrounding mica (mica-mica). The force profile is reproducible over multiple approach/pull-off cycles and the patterned surfaces jump into adhesive contact on each approach. Upon separation from contact, an adhesive force can be measured for the patterned surface that is reproducible over multiple force runs. The adhesive force is - $F_{\text{adh}}/R = 7.6 \pm 3.0 \text{ mN/m}$. This adhesive force is lower than both the measured mica-mica and APTES-mica adhesion values of Table 6.1.

Assigning an effective surface potential to the patterned surfaces

One way to treat a heterogeneously charged surface for calculating particle-surface interaction forces is to assign an effective surface potential to the surface, treating it as if it behaved like a homogeneous surface.¹¹⁷ This is essentially a mean-field treatment of heterogeneous surface. We are interested in obtaining an effective surface potential for the patterned surface in Fig. 6.2 and comparing this value to a net surface potential calculated from the patch coverage and surface charge densities of the

homogeneous APTES and mica surfaces. An effective surface potential is fitted to the patterned surface by performing a least squares fit for the patterned surface's effective potential (as if it were a homogeneous surface described by one potential). To perform this fit, the surface potential of the opposing mica surface fixed to the value reported for mica in Table 6.1 and the expected Debye length for the electrolyte ($\kappa^{-1} = 31\text{nm}$ for 10^{-4} HCl) is used. The fits for an effective surface potential are shown in Figure 6.2B. The corresponding effective surface potentials are reported in Table 6.2 for a three different pairs of boundary conditions: 1) Patterned surface constant charge (CC) or 2) constant potential (CP) with a constant potential opposing mica surface (CC-CP or CP-CP) and 3) both patterned surface and mica surface set to constant charge boundary condition (CC-CC).

Table 6-2 Fits for an effective potential for the patterned surface for different boundary conditions ($\psi_{\text{mica}} = -120 \text{ mV}$, $\kappa^{-1} = 31 \text{ nm}$) Plots of fitted values shown in Fig. 6.2B.

<i>Boundary conditions (Patterns:Mica)</i>	<i>CC:CP</i>	<i>CP:CP</i>	<i>CC:CC</i>
<i>Effective surface potential, Ψ_{patterns}</i>	$8 \pm 4 \text{ mV}$	$-51 \pm 13 \text{ mV}$	$18 \pm 4 \text{ mV}$

As shown in Figure 6.3B, using constant potential boundary conditions for both surfaces leads to a fit that does not describe the measured force profiles well. While constant charge boundary conditions for both surfaces are an improvement, the best fit comes from setting the patterned surface to a constant charge surface and the mica surface to a constant potential surface and fixing the patterned surface to a potential of $8 \pm 4 \text{ mV}$.

The fitted effective surface potential can be compared to a value predicted based on the patch coverage and the surface charge densities of the APTES and mica surfaces. In this treatment, the surface charge of the APTES patches and mica are treated as if it was “smeared out” over the entire surface uniformly. The surface charge densities for the homogeneous surfaces are related to the surface potentials by the Grahame equation:

$$\sigma_{\text{APTES,mica}} = \sqrt{8n_0 \epsilon \epsilon_0 kT} \sinh\left(\frac{e\Psi_{\text{APTES,mica}}}{2kT}\right) \quad (6.1)$$

Using the surface charge densities for the APTES and mica surfaces reported in Table 6.1, a net surface charge density, σ_{net} , for the patterned surface is calculated from the fractional patch surface coverage as follows:

$$\sigma_{\text{net}} = \sigma_{\text{APTES}} f_p + (1-f_p) \sigma_m \quad (6.2)$$

Where f_p is the fraction of the surface covered by APTES patches. Using the net surface charge density, a net surface potential is obtained by substitution back into the Grahame equation:

$$\Psi_{\text{net}} = \frac{2kT}{e} \sinh^{-1}\left(\frac{\sigma_{\text{net}}}{\sqrt{8n_0 \epsilon \epsilon_0 kT}}\right) \quad (6.3)$$

When applied to the surface shown in Fig. 6.2 with the patch coverage of 11.5%, $\Psi_{\text{net}} = -107.9$ mV. This is a significantly more negative value than the fitted effective potentials in Table 6.2. One possible explanation for this disagreement could be that the

fractional coverage of the entire surface may not agree with the coverage inside the electrostatic zone of influence and instead, the surface charge density within the ZOI should be smeared out instead of the entire surface. If the maximum and minimum possible patch coverages within the ZOI (obtained from image analysis) are used, we can recalculate the net surface potential and compare it to the fitted effective surface potentials. Table 6.3 summarizes the average, maximum and minimum patch coverages measured in the ZOI from image analysis and the corresponding net surface potentials calculated.

Table 6-3 Measured average, maximum, and minimum patch coverage within ZOI from image analysis of figure 6.3D and corresponding calculated net surface potentials

$f_{p,zoi}$	13.1±3.8%	$\Psi_{net,zoi}$	-106±4 mV
$f_{p,zoi,max}$	18.4%	$\Psi_{net,zoi,max}$	-100mV
$f_{p,zoi,min}$	4.9%	$\Psi_{net,zoi,min}$	-115mV

The average coverage within the zone of influence differs slightly from the coverage based on the entire surface. Using the average coverage in the zone of influence, $\Psi_{net} = -106 \pm 4$ mV. Likewise, the maximum and minimum patch coverage in the zone of influence measured from image analysis still produce very negative surface potentials (-100 and -115 mV respectively). Neither of these values obtained agree with the fitted effective surface potentials from table 6.2. This suggests that the effective surface potential cannot be calculated from patch surface coverage and the surface charge densities of APTES and mica. This result agrees with previous studies that have attempted to predict an effective surface potential for a heterogeneously charged surface and shown that this effective potential does not agree with an average potential assigned

based on surface coverage.^{117, 119} This observation has also been made from electrokinetic studies of heterogeneously charged surfaces.⁴⁰

Linear mixing of interaction forces for APTES-mica and mica-mica

An alternative fitting procedure to the effective surface potential method would be to invoke the linear mixing approximation outlined in detail in chapter 5. In this case, the measured force profiles are fitted for the patch coverage.

$$\frac{F_{net}}{R}(D) = f_{p,zoi} \frac{F_{APTES-mica}}{R}(D) + (1 - f_{p,zoi}) \frac{F_{mica-mica}}{R} \quad (6.4)$$

Where F_{net}/R is the net DLVO interaction force normalized by the radius of curvature, $F_{APTES-mica}/R$ is the homogeneous APTES-mica DLVO interaction force, $F_{mica-mica}/R$ is the homogeneous mica-mica DLVO interaction force, and $f_{p,zoi}$ is the APTES patch coverage within the zone of influence. It is assumed here that the van der Waals force for APTES-mica and mica-mica are approximately equal and the Hamaker constant for mica-mica in aqueous solutions is assigned to both. (Hamaker constant, $A_H = 2.2 \times 10^{-20} \text{J}$)¹⁰³

Using the known homogeneous mica-mica and mica-APTES interactions, the fractional coverage within the ZOI can be fitted from a least squares fit. When applied to the force data in Fig 6.3, we obtain $f_{p,zoi} = 26.0 \pm 1.6\%$. The solid black line in figure 6.2C shows the fitted interaction with this patch coverage. This is a higher patch coverage than the maximum patch coverage within the ZOI measured from image analysis ($f_{p,zoi,max} =$

18.4%). This could be attributed to the linear mixing approximation causing an overestimation of the patch coverage within the zone of influence. As detailed in chapter 5, the linear mixing approximation is better applied to multiple patches in the ZOI versus single patches. However, despite this discrepancy, general agreement with linear mixing approximation supports a simple additivity to surface forces with heterogeneously charged surfaces. This is in contrast to the non-additive nature of hydrophobic-hydrophilic interactions observed by Kokkoli and Zukoski.⁵⁰

Recovering mica-mica interaction with removal of APTES patterns

The observed results in Fig. 6.2 support an additive interaction between APTES-mica and mica-mica. To further support this, the APTES patches can be removed from the surface in-situ to see if a mica-mica interaction is recovered. APTES monolayers are susceptible to removal in highly alkaline pH conditions,^{76, 148} which we exploit here to remove the APTES patterns from the patterned surface during an experiment. Figure 6.4 shows the measured force profiles between the patterned surface of Figure 6.2 at a pH of 9.1 (The pH of the bath solution is measured after the SFA experiment). This pH change was accomplished by added a small amount of concentrated potassium hydroxide solution to the electrolyte bath in the SFA. After adding potassium hydroxide the surfaces separation is cycled several times to facilitate mixing of the electrolyte solution and the bath is equilibrated for 4 hours under alkaline conditions prior to subsequent force measurements. Figure 6.3B shows the surface tagged with negatively charged fluorescent nanoparticles after the experiment. Although a few particles deposit, much of the APTES

is removed from the surface (as compared to its “twin” in Fig. 6.2D) as a result of the alkaline conditions in the bath.

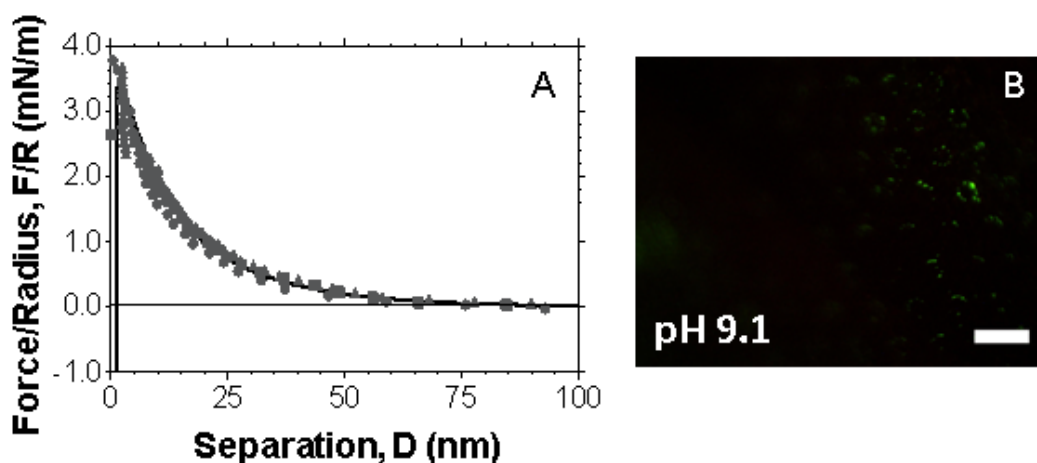


Figure 6.4 A) Force normalized by radius of curvature between a mica surface and patterned surface of Fig. 6.2 at pH 9.1. Black line is fitted force profile with $\kappa^{-1} = 18.6$ nm and $\Psi_{\text{patterns}} = -103$ mV with constant potential boundary conditions. B) Fluorescent image of tagged surface verifying APTES patch removal under alkaline conditions, Scale bar = 100 μm .

The black line in figure 6.3A is a fit for the surface potential of the patterned surface with APTES removed. The opposing mica surface potential was set to -120mV. The surface (with patterns removed) was fitted to a surface potential of -103 ± 10 mV and a Debye length of 18.6 ± 2.2 nm by performing a least squares fit of the data under constant potential boundary conditions. This indicates a recovery of a mica-mica interaction when patches are removed and supports the argument that the measured forces in Fig. 6.2 are the result of both mica-mica and APTES-mica interactions.

Finally, an adhesive force can be measured upon pull-out after the surfaces are brought into contact. The measured adhesion forces, $-F_{adh}/R$, is 4.3 ± 0.6 mN/m and is reproducible over multiple force measurements. It is similar, though slightly lower, value to that reported with the patterns present at low pH.

6.3.3 Many patches in the zone of influence

The previous force measurement in Fig 6.2 involved the case where the ZOI is nearly the same size as the patch spacing and contains a single APTES patch. However, an alternative scaling regime is when many small patches are within the zone of influence. In this case (when there is also an ordered distribution of patches on the entire surface) the fractional coverage of patches within the ZOI should be identical regardless of the location of the point-of-closest approach between the surfaces. As a consequence, similar force profiles should be measured on different locations of the surface. This can be demonstrated by reducing pattern dimensions and measuring interaction forces on multiple locations in the SFA, as is shown in Figure 6.4.

Figure 6.4A shows the interaction of a mica surface with an APTES-patterned surface containing patches 9.3 ± 2.6 μm in diameter and 9.4 ± 2.6 μm edge-to-edge spacing ($f_p = 23.0 \pm 8.7$ % from image analysis) in 10^{-4} M hydrochloric acid solution. The interaction at two different locations is shown for multiple approaches runs (solid symbols for the first location and empty symbols for the second). Both of these locations show similar force profiles and are attractive with a jump in to contact. The homogeneous mica-mica (blue line) and APTES-mica (red line) force profiles are included. As with the

larger patterns in Fig 6.2, the measured forces fall between these two homogeneous limits. Fig. 6.4B shows the surface tagged with fluorescent carboxylic acid functionalized nanoparticles following force measurement.

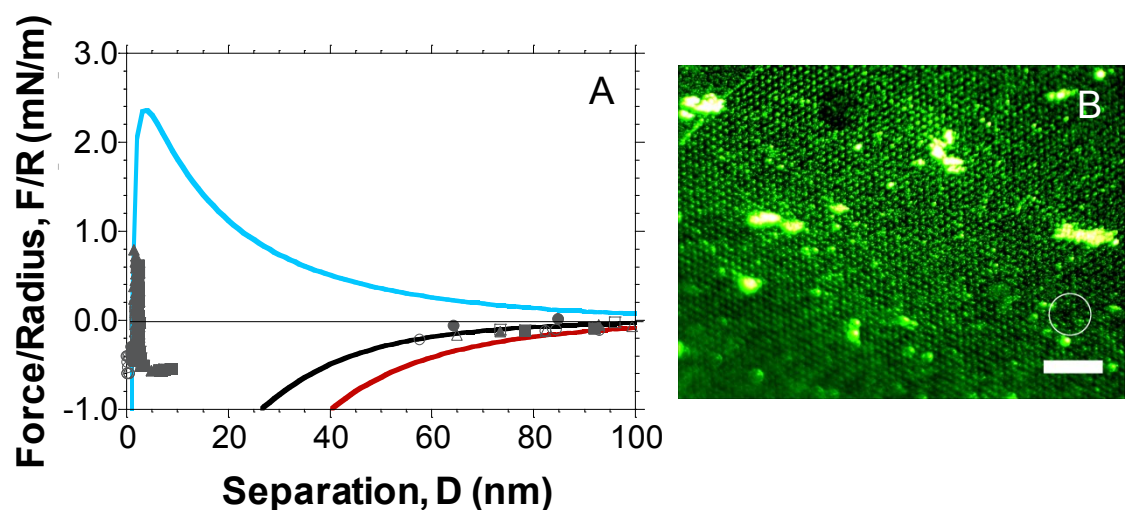


Figure 6.5 A) Force normalized by radius of curvature for a mica surface interacting with small patterns in 10^{-4} M hydrochloric acid solution at two different locations (solid and empty symbols). Blue line shows mica-mica interaction, red shows APTES-mica, and black shows fit based on linear mixing approximation with $f_{p,zoi} = 66\%$ (based on fit for both locations) B) Surface tagged with fluorescent particles after SFA experiment ($f_p = 23.0 \pm 8.7\%$ from image analysis), Scale bar = 100 microns, ZOI ($r_{zoi} = 35.2 \mu\text{m}$) shown as a circle above the scale bar.

In Fig. 6.4A, the fit of the data for the fractional coverage in the zone of influence is shown. For location 1 (solid symbols), $f_{p,zoi} = 64.9 \pm 25.7\%$. For location 2, $f_{p,zoi} = 67.2 \pm 22.6\%$. Both spots combined give an average coverage of $f_{p,zoi} = 66.1 \pm 23.1\%$, the fitted value shown by the black line in Fig. 6.4A. Additionally, after the jump into contact

shown in Fig. 6.4A, an adhesive force can be measured upon separation of the surfaces. For the first location (solid symbols), $-F_{\text{adh}}/R = 23.6 \pm 3.9$ mN/m. For the second location (empty symbols), $-F_{\text{adh}}/R = 24.1 \pm 1.2$ mN/m. The adhesion force between both locations agree and are reproducible over multiple approach/retraction cycles.

While the fitted fractional coverage for the two locations in figure 6.4A agree, this fitted coverage is significantly higher than that obtained from image analysis. There could be a few causes for this discrepancy. First, the pattern fidelity in figure 6.4B isn't as high as in Figure 6.3D, as indicated by some extraneous particle deposition outside of the larger patches. This would lead to a higher effective patch coverage than expected. Further, the attractive nature of the forces measured means that fewer data points are available for fitting, as indicated by the large deviation in the fitted patch coverages reported. Still, the fact that two different spatial locations on the surface agree supports the hypothesis that when there is little variation in patch coverage within the ZOI between different spatial locations, the net interaction should be similar for different locations on the surface.

6.4 Conclusions

Direct force measurement has remained a relatively unexplored avenue for studying the effects of charge heterogeneities on surface forces. The benefits of employing the SFA come from the ability to scale up the electrostatic zone of influence and fabricate surfaces with well-defined charge heterogeneities within this zone to directly measure the effects charge heterogeneities have on surface forces. The results

presented in this chapter are the first time surfaces bearing micropatterned charge heterogeneities have been employed in the surface forces apparatus to directly probe the effects of charge heterogeneities on surface forces in electrolyte solutions. The force measurements in this chapter were between a negatively charge mica surface and a mica surface bearing positively charge APTES monolayer patches. The measured net interaction forces were found to be reproducible over multiple force runs and intermediate between the homogeneous mica-mica and APTES-mica interactions. The measured force profiles could be fitted for a patch coverage based on the linear mixing approximation presented in chapter 5. The results of this chapter suggests that interactions between a particle and a patchy surface are additive, in contrast to hydrophobic-hydrophilic interactions measured by Kokkoli⁵⁰.

For the case of a single patch located within the ZOI, the interactions were fitted for both an effective surface potential for and an effective patch coverage. The fitted effective surface potential could not be predicted from the homogeneous mica and APTES surface potentials and patch coverage. Alternatively, it was found that fitting for patch coverage gave a very good fit to the data although there was a discrepancy with a higher fitted patch coverage compared to that expected from image analysis. Removing the APTES patches under highly alkaline conditions results in recovery of a mica-mica interaction. This result further supports that measured force profiles with the patches present are due to contributions from both the patch and surround mica surfaces.

For smaller patterns, in which several patches are located in the ZOI, the measured interaction for two locations agrees and was measured as attractive. The fitted

patch coverage does not agree with that obtained from image analysis of the tagged surface. However, this could be the result of poorer pattern fidelity than expected leading to a higher coverage of APTES within the zone of influence.

Chapter 7 Conclusions

7.1 Concluding remarks

Colloidal interactions at solid-liquid interfaces play a critical role in governing particle deposition phenomena by determine whether particle deposition onto a surface is energetically favorable or not. Colloidal interactions at surfaces are classically described within the framework of DLVO theory where the net particle-surface interaction is a superposition of an electrostatic force arising from double layer overlap and van der Waals forces. For all its success, DLVO theory alone falls short in predicting particle-surface interaction energies in systems that violate the assumption of uniform surface charge densities by containing surface charge heterogeneities. These surface charge heterogeneities alter electrostatic interaction forces and can provide local energetically favorable locations for particle deposition onto surfaces. Patterned charge heterogeneities also present a means of controlling particle deposition for applications in involving self-assembly and the fabrication of high-specificity surfaces for sensing and separations applications. While several studies has investigated the effects of charge heterogeneities through computational methods and the measurement of particle deposition rates in flow systems, the direct measurement of surface forces with charge heterogeneities remains an unexplored method for studying the effects of charge heterogeneities on particle deposition behavior. One of the primary difficulties involved with direct force measurement experiments is the small size of the effective electrostatic interaction area, referred to as the electrostatic zone of influence in literature. The size of this zone of

influence scales with the square root of the particle radius of curvature and Debye length of the system.

In this thesis, the surface forces apparatus (SFA) was employed to directly measure forces profiles with surfaces containing well-defined charge heterogeneities. The SFA simultaneously provides a means of performing direct force measurements and scaling up the interaction area due to the large radius of curvature (1-2cm) of the interacting surfaces. This allows conventional photolithographic techniques to be used to fabricate surfaces with well-defined micropatterned charge heterogeneities smaller than the electrostatic zone of influence. A vapor deposition process was developed here to create monolayers of aminosilane on mica surfaces. This process was optimized to ensure that the aminosilane patches present minimal topographical variations while leaving the surrounding mica surface free of any contamination from the patterning process. Creating a surface with minimal topographical variations is necessary to ensure that only the effects of charge heterogeneities and not physical asperities is investigated. Additionally, such patterns are required due to the sub-nanometer resolution in surface separation afforded by the SFA. The measured force profiles for heterogeneously charged surfaces show an intermediate profile between the expected interactions for homogeneous aminosilane-mica and mica-mica surface pairs. The measured forces are also analyzed with a simple linear mixing approximation previously reported in literature and expanded here to predict surface forces for arbitrary surface potentials and boundary conditions.

7.2 Impact and Contributions

Chapter 4 presents a method of generating surfaces with micropatterned charge heterogeneities on flat and curved mica surfaces using a vapor deposition procedure through elastomeric PDMS membranes. This chapter discusses several steps necessary to successfully generate high quality micropatterned monolayers of 3-aminopropyltriethoxysilane (APTES) with minimal topographical variations and minimizing the transfer of contaminants to the surrounding mica surfaces. Such steps include extracting oligomers from the membranes to prevent the transfer of oligomers from the membranes to the underlying mica surfaces and forming a barrier layer on generated on the top side of the membrane surfaces to minimize diffusion of APTES through the elastomeric material. Further, the amount of APTES used in the vapor deposition process is optimized to generate complete monolayers while minimizing capillary condensation at the membrane-mica-vapor triple contact line. The surface potentials of both the mica and APTES surfaces are characterized through a series of direct force measurements indicated that the process yields highly charged micropatterns while leaving the surrounding mica free of any residues from the patterning process.

Chapter 5 discusses a simple method, referred to here as the linear mixing approximation, for estimating forces and interaction energies between particles and heterogeneously charged surfaces. This method expands upon previous work found in literature^{41, 45, 119} and outlines the necessary scaling of the electrostatic zone of influence to provide agreement with full solutions published in literature from grid-surface

integration (GSI) solutions. Additionally, the linear mixing approximation is used here with numerical solutions to the Poisson-Boltzmann equation to predict interaction forces and energies for particles interaction with patchy surfaces at arbitrary surface potentials and boundary conditions. The results of this chapter illustrate the importance of boundary conditions in particle-surface interaction forces and energies.

Chapter 6 presents direct force measurements with micropatterned charged heterogeneities in the surface forces apparatus (SFA). The heterogeneities consist of APTES patches on mica and the opposing surface is mica. The SFA is ideally suited for performing direct force measurements with charge heterogeneities due particularly to the large radius of curvature of the interacting surfaces. This large radius of curvature drastically scales the size of the electrostatic zone of influence up so that several charge heterogeneities can be patterned within this area. The force measurement results presented in this chapter reveal that the net interaction force with a patchy heterogeneous surface falls between the surrounding surface and the heterogeneities, indicating an additive contribution from the bulk and patch surfaces. The measured data can be fitted for an effective potential of the heterogeneous surfaces. It is shown that this fitting is highly dependent on the boundary conditions used and does not agree with a predicted potential based on the surface charge densities of the patch and surround bulk surfaces and the surface coverage of the patches. Instead, it is shown that the data can be fitted for a patch coverage based on the homogeneous interactions between the patch-mica and mica-mica interactions by invoking the linear mixing approximation. When the patches are removed from the surface, a mica-mica interaction is recovered, supporting the

reasoning that the measured interaction is from the contribution of the patches. Further, it is shown that when several patches are present in the ZOI, the interaction obtained is approximately constant on different locations of the surface, in agreement with the scaling of the electrostatic zone of influence.

7.3 Future Directions

The work presented in this thesis centers on the fabrication of surfaces with well-defined micropatterned charge heterogeneities and the use of these substrates in the surface forces apparatus (SFA) to explore the effects of charge heterogeneities on surface forces. The patterning method developed here, together with their use in the SFA, opens the doors to a wide range of future experiments further exploring interactions with heterogeneously charged surfaces. The results presented in this thesis show that the measured interaction of a heterogeneously patchy surface is intermediate between the patch-mica and mica-mica interaction and general agreement with the linear mixing approximation is observed. Future work would be best focused on performing additional force measurements for surfaces with many patches within the zone of influence and comparing the results to estimates from the linear mixing approximation to determine whether or not exact agreement can be obtained with the true fractional surface coverage of patches. Accomplishing this will require further experiments with surfaces containing well-defined charge heterogeneities and measuring interactions on several locations on the surfaces. Different ionic strengths could also be investigated but will require the further characterization of the APTES surface potential for different electrolyte

conditions. Of particular interest in future studies would be capturing a transition between the many patches in the ZOI to a single patch in the ZOI by decreasing the size of the zone of influence during an experiment through an increase in the solution ionic strength leading to a reduction in the Debye lengths.

One interesting avenue of research arising from the work presented in this thesis would be the possibility for measuring the interaction between two micropatterned patchy surfaces. Previous work with the SFA measured forces between random charge mosaic surfaces that revealed a long-range attraction which has been attributed to correlation between randomly distributed positively and negatively charged surface domains.^{137, 138} With the micropatterned surfaces developed in this thesis, interactions between two micropatterned surfaces could be explored. Patterning could provide an exact correlation between positively and negatively domains and measured interactions could be highly dependent on the alignment between the two SFA surfaces. A maximum repulsive force obtained when positively charged patches are aligned while misalignment could lead to attractive interactions. Such an investigation has implications in surface pattern recognition.

There are, potentially, other directions possible that build from the work presented in this thesis. While only APTES patterned surfaces were explored in this thesis, the vapor deposition procedure developed here could be adapted to other silane species to generate surfaces with different chemical functionality. Likewise, the primary amine group on APTES could be used as a reactive site for incorporating different chemical functionality onto the surface.⁸¹ This could allow for a host of experiments with

patterned chemical functionality to be explored in the surface forces apparatus (SFA). For example, hydrophobic surfaces could be fabricated through the vapor deposition of fluorosilanes on mica, opening up the door to studying hydrophobic–hydrophilic interactions with well-defined surface patterns in the SFA. In contrast to the colloidal probe technique used previously by Kokkoli and Zukoski⁵⁰, both surfaces could be patterned with hydrophobic domains to study pattern recognition with hydrophobic interactions.

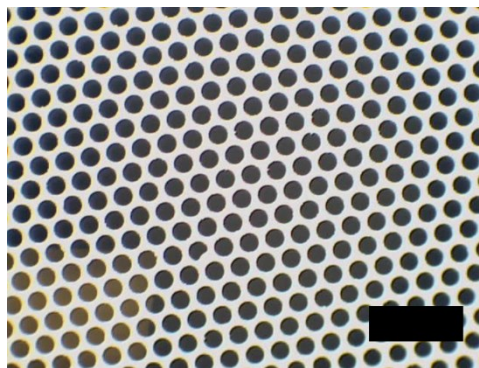


Figure 7.1 40x12 μm array of 50nm high silver pillars on a curved mica surface (radius of curvature $\sim 2\text{cm}$) formed via thermal evaporation through an elastomeric membrane. Scale bar = 200 μm .

Finally, an alternative method for studying heterogeneous interactions is available using elastomeric membranes as shadow masks for the thermal evaporation of silver on mica surfaces. Use of the elastomeric membranes for patterning metallic layers was demonstrated in the work of Jackman et al. during their work developing elastomeric membranes.⁹⁸ For surface force measurements, the silver pillars can be evaporated directly on curved mica substrates, as shown in Fig. 7.1. These silver pillars can be functionalized with a self-assembled monolayer of a mercaptoalkanoic acids¹⁴⁹

generating negatively charged micropatterned surfaces. These surfaces could be used to study the effects of surface topography on electrostatic interactions in the surface forces apparatus in an analogous fashion to the charge heterogeneities explored in this thesis.

References

1. Yao, K.-M.; Habibian, M. T.; O'Melia, C. R. Water and waste water filtration. Concepts and applications. *Environ. Sci. Technol.* **1971**, *5*, 1105-1112.
2. Tiraferri, A.; Tosco, T.; Sethi, R. Transport and retention of microparticles in packed sand columns at low and intermediate ionic strengths: experiments and mathematical modeling. *Environ Earth Sci* **2011**, *63*, 847-859.
3. Adamczyk, Z.; Weroński, P. Application of the DLVO theory for particle deposition problems. *Adv. Colloid Interface Sci.* **1999**, *83*, 137-226.
4. Tufenkji, N.; Elimelech, M. Breakdown of Colloid Filtration Theory: Role of the Secondary Energy Minimum and Surface Charge Heterogeneities. *Langmuir* **2005**, *21*, 841-852.
5. Tobiasson, J. E.; O'Melia, C. R. Physicochemical Aspects of Particle Removal in Depth Filtration. *Journal (American Water Works Association)* **1988**, *80*, 54-64.
6. Swanton, S. W. Modelling colloid transport in groundwater; the prediction of colloid stability and retention behaviour. *Adv. Colloid Interface Sci.* **1995**, *54*, 129-208.
7. McCarthy, J. F.; Zachara, J. M. Subsurface transport of contaminants. *Environ. Sci. Technol.* **1989**, *23*, 496-502.
8. Ryan, J. N.; Elimelech, M. Colloid mobilization and transport in groundwater. *Colloids Surf., A* **1996**, *107*, 1-56.
9. Grier, D. G. Colloids: A surprisingly attractive couple. *Nature* **1998**, *393*, 621-623.
10. Dabroś, T.; van de Ven, T. G. M. A direct method for studying particle deposition onto solid surfaces. *Colloid Polym Sci* **1983**, *261*, 694-707.
11. Prevo, B. G.; Kuncicky, D. M.; Velev, O. D. Engineered deposition of coatings from nano- and micro-particles: A brief review of convective assembly at high volume fraction. *Colloids Surf., A* **2007**, *311*, 2-10.
12. Canpean, V.; Astilean, S.; Petrisor, T.; Gabor, M.; Ciascai, I. Convective assembly of two-dimensional nanosphere lithographic masks. *Mater. Lett.* **2009**, *63*, 1834-1836.

13. Li, F.; Josephson, D. P.; Stein, A. Colloidal Assembly: The Road from Particles to Colloidal Molecules and Crystals. *Angew. Chem. Int. Ed.* **2011**, *50*, 360-388.
14. Ma, L.-C.; Subramanian, R.; Huang, H.-W.; Ray, V.; Kim, C.-U.; Koh, S. J. Electrostatic Funneling for Precise Nanoparticle Placement: A Route to Wafer-Scale Integration. *Nano Lett.* **2007**, *7*, 439-445.
15. Wang, D.; Mohwald, H. Template-directed colloidal self-assembly - the route to 'top-down' nanochemical engineering. *J. Mater. Chem.* **2004**, *14*, 459-468.
16. Chen, J. Y.; Klemic, J. F.; Elimelech, M. Micropatterning Microscopic Charge Heterogeneity on Flat Surfaces for Studying the Interaction between Colloidal Particles and Heterogeneously Charged Surfaces. *Nano Lett.* **2002**, *2*, 393-396.
17. Zhang, J.; Li, Y.; Zhang, X.; Yang, B. Colloidal Self-Assembly Meets Nanofabrication: From Two-Dimensional Colloidal Crystals to Nanostructure Arrays. *Adv. Mater.* **2010**, *22*, 4249-4269.
18. Liu, S.; Maoz, R.; Schmid, G.; Sagiv, J. Template Guided Self-Assembly of [Au55] Clusters on Nanolithographically Defined Monolayer Patterns. *Nano Lett.* **2002**, *2*, 1055-1060.
19. Kozlova, N.; Santore, M. M. Manipulation of Micrometer-Scale Adhesion by Tuning Nanometer-Scale Surface Features. *Langmuir* **2002**, *22*, 1135-1142.
20. Rizwan, T.; Bhattacharjee, S. Particle Deposition onto Charge-Heterogeneous Substrates. *Langmuir* **2009**, *25*, 4907-4918.
21. Aizenberg, J.; Braun, P. V.; Wiltzius, P. Patterned Colloidal Deposition Controlled by Electrostatic and Capillary Forces. *Phys. Rev. Lett.* **2000**, *84*, 2997-3000.
22. Zheng, H.; Rubner, M. F.; Hammond, P. T. Particle Assembly on Patterned "Plus/Minus" Polyelectrolyte Surfaces via Polymer-on-Polymer Stamping. *Langmuir* **2002**, *18*, 4505-4510.
23. Lee, I.; Zheng, H.; Rubner, M. F.; Hammond, P. T. Controlled Cluster Size in Patterned Particle Arrays via Directed Adsorption on Confined Surfaces. *Adv. Mater.* **2002**, *14*, 572-577.
24. Bohnet, M. Fouling of heat transfer surfaces. *Chem. Eng. Technol.* **1987**, *10*, 113-125.
25. Schultz, M. P.; Bendick, J. A.; Holm, E. R.; Hertel, W. M. Economic impact of biofouling on a naval surface ship. *Biofouling* **2010**, *27*, 87-98.

26. Zhu, X.; Elimelech, M. Colloidal Fouling of Reverse Osmosis Membranes: Measurements and Fouling Mechanisms. *Environ. Sci. Technol.* **1997**, *31*, 3654-3662.
27. Chen, K. L.; Song, L.; Ong, S. L.; Ng, W. J. The development of membrane fouling in full-scale RO processes. *J. Membrane Sci.* **2004**, *232*, 63-72.
28. Mukhopadhyay, R. When microfluidic devices go bad. *Anal. Chim. Acta* **2005**, *77*, 429 A-432 A.
29. Shawgo, R. S.; Richards Grayson, A. C.; Li, Y.; Cima, M. J. BioMEMS for drug delivery. *Curr. Opin. Solid State Mater. Sci.* **2002**, *6*, 329-334.
30. Torkzaban, S.; Bradford, S. A.; Walker, S. L. Resolving the Coupled Effects of Hydrodynamics and DLVO Forces on Colloid Attachment in Porous Media. *Langmuir* **2007**, *23*, 9652-9660.
31. Spielman, L. A.; Friedlander, S. K. Role of the electrical double layer in particle deposition by convective diffusion. *J. Colloid Interface Sci.* **1974**, *46*, 22-31.
32. Russel, W. B.; Saville, D. A.; Schowalter, W. R. *Colloidal Dispersions*; Cambridge University Press: New York, 1989.
33. Israelachvili, J. N. *Intermolecular and Surface Forces*; 3rd ed.; Academic Press: Waltham, MA, 2011.
34. Elimelech, M.; Gregory, J.; Jia, X.; Williams, R. A. *Particle Deposition and Aggregation: Measurement, Modeling, and Simulation*; Butterworth-Heinemann: Woburn, MA, 1995.
35. Verwey, E. J. W.; Overbeek, J. T. *Theory of Stability of Lyophobic Colloids*; Elsevier: New York, 1948.
36. Ninham, B. W. On progress in forces since the DLVO theory. *Adv. Colloid Interface Sci.* **1999**, *83*, 1-17.
37. Walz, J. Y. The effect of surface heterogeneities on colloidal forces. *Adv. Colloid Interface Sci.* **1998**, *74*, 119-168.
38. Litton, G. M.; Olson, T. M. Colloid Deposition Kinetics with Surface-Active Agents: Evidence for Discrete Surface Charge Effects. *J. Colloid Interface Sci.* **1994**, *165*, 522-525.

39. Richmond, P. Electrical forces between particles with discrete periodic surface charge distributions in ionic solution. *J. Chem. Soc., Faraday Trans. 2* **1975**, *71*, 1154-1163.
40. Elimelech, M.; Nagai, M.; Ko, C.-H.; Ryan, J. N. Relative Insignificance of Mineral Grain Zeta Potential to Colloid Transport in Geochemically Heterogeneous Porous Media. *Environ. Sci. Technol.* **2000**, *34*, 2143-2148.
41. Pazmino, E.; Trauscht, J.; Dame, B.; Johnson, W. P. Power law size-distributed heterogeneity explains colloid retention on soda lime glass in the presence of energy barriers. *Langmuir* **2014**, *30*, 5412-5421.
42. Miklavic, S. J.; Chan, D. Y. C.; White, L. R.; Healy, T. W. Double Layer Forces between Heterogeneous Charged Surfaces. *J. Phys. Chem.* **1994**, *98*, 9022-9032.
43. Duffadar, R. D.; Davis, J. M. Interaction of micrometer-scale particles with nanotextured surfaces in shear flow. *J. Colloid Interface Sci.* **2007**, *308*, 20-29.
44. Shen, C.; Lazouskaya, V.; Zhang, H.; Li, B.; Jin, Y.; Huang, Y. Influence of surface chemical heterogeneity on attachment and detachment of microparticles. *Colloids Surf., A* **2013**, *433*, 14-29.
45. Bendersky, M.; Santore, M. M.; Davis, J. M. Statistically-based DLVO approach to the dynamic interaction of colloidal microparticles with topographically and chemically heterogeneous collectors. *J. Colloid Interface Sci.* **2015**, *449*, 443-451.
46. Kline, T. R.; Chen, G.; Walker, S. L. Colloidal deposition on remotely controlled charged micropatterned surfaces in a parallel-plate flow chamber. *Langmuir* **2008**, *24*, 9381-9385.
47. Elimelech, M.; Chen, J. Y.; Kuznar, Z. A. Particle Deposition onto Solid Surfaces with Micropatterned Charge Heterogeneity: The “Hydrodynamic Bump” Effect. *Langmuir* **2003**, *19*, 6594-6597.
48. Boluk, M. Y.; van de Ven, T. G. M. Effects of polyelectrolytes on flow-induced deposition of titanium dioxide particles onto a cellophane surface. *Colloid Surface* **1990**, *46*, 157-176.
49. Böhmer, M. R. Effects of Polymers on Particle Adsorption on Macroscopic Surfaces Studied by Optical Reflectometry. *J. Colloid Interface Sci.* **1998**, *197*, 251-256.
50. Kokkoli, E.; Zukoski, C. F. Surface Pattern Recognition by a Colloidal Particle. *Langmuir* **2001**, *17*, 369-376.

51. Pick, C.; Argento, C.; Drazer, G.; Frechette, J. Micropatterned Charge Heterogeneities via Vapor Deposition of Aminosilanes. *Langmuir* **2015**, *31*, 10725-10733.
52. Goodwin, J. W. *Colloids and Interfaces with Surfactants and Polymers - An Introduction*; John Wiley and Sons, Ltd: West Sussex, England, 2004.
53. Gur, Y.; Ravina, I.; Babchin, A. J. On the electrical double layer theory. I. A numerical method for solving a generalized Poisson—Boltzmann equation. *J. Colloid Interface Sci.* **1978**, *64*, 326-332.
54. Hogg, R.; Healy, T. W.; Fuerstenau, D. W. Mutual coagulation of colloidal dispersions. *Trans. Faraday Soc.* **1966**, *62*, 1638-1651.
55. Autumn, K.; Sitti, M.; Liang, Y. A.; Peattie, A. M.; Hansen, W. R.; Sponberg, S.; Kenny, T. W.; Fearing, R.; Israelachvili, J. N.; Full, R. J. Evidence for van der Waals adhesion in gecko setae. *Proc. Natl. Acad. Sci. U.S.A.* **2002**, *99*, 12252-12256.
56. Hamaker, H. C. The London—van der Waals attraction between spherical particles. *Physica* **1937**, *4*, 1058-1072.
57. Lifshitz, E. M. The Theory of Molecular Attractive Forces between Solids. *Soviet Physics* **1956**, *2*, 73-83.
58. Derjaguin, B. V.; Landau, L. Theory of the stability of strongly charged lyophobic sols and of the adhesion of strongly charged particles in solutions of electrolytes. *Acta Physicochim URSS* **1941**, *14*, 633-662.
59. Ma, H.; Pazmino, E.; Johnson, W. P. Surface Heterogeneity on Hemispheres-in-Cell Model Yields All Experimentally-Observed Non-Straining Colloid Retention Mechanisms in Porous Media in the Presence of Energy Barriers. *Langmuir* **2011**, *27*, 14982-14994.
60. Hoek, E. M. V.; Agarwal, G. K. Extended DLVO interactions between spherical particles and rough surfaces. *J. Colloid Interface Sci.* **2006**, *298*, 50-58.
61. Tabor, D.; Winterton, R. H. S. The Direct Measurement of Normal and Retarded van der Waals Forces. *Proc. R. Soc. London, Ser. A* **1969**, *312*, 435-450.
62. Israelachvili, J. N.; Tabor, D. The Measurement of van der Waals Dispersion Forces in the Range 1.5 to 130 nm. *Proc. R. Soc. Lond. A* **1972**, *331*, 19-38.

63. Israelachvili, J. N.; Adams, G. E. Measurements of forces between two mica surfaces in aqueous electrolyte solutions in the range 0-100nm. *J. Chem. Soc. Faraday Trans. I* **1978**, *74*, 975-1001.
64. Pashley, R.; McGuiggan, P.; Ninham, B.; Evans, D. Attractive forces between uncharged hydrophobic surfaces: direct measurements in aqueous solution. *Science* **1985**, *229*, 1088-1089.
65. Helm, C. A.; Israelachvili, J. N.; McGuiggan, P. M. Role of hydrophobic forces in bilayer adhesion and fusion. *Biochemistry* **1992**, *31*, 1794-1805.
66. Chan, D. Y. C.; Horn, R. G. The drainage of thin liquid films between solid surfaces. *J. Chem. Phys.* **1985**, *83*, 5311-5324.
67. Gupta, R.; Fréchet, J. Measurement and Scaling of Hydrodynamic Interactions in the Presence of Draining Channels. *Langmuir* **2012**, *28*, 14703-14712.
68. Tolansky, S. *Multiple-Beam Interferometry of Surfaces and Films*; Oxford University Press: London, 1948.
69. Israelachvili, J.; Min, Y.; Akbulut, M.; Alig, A.; Carver, G.; Greene, W.; Kristiansen, K.; Meyer, E.; Pesika, N.; Rosenberg, K. Recent advances in the surface forces apparatus (SFA) technique. *Rep. Prog. Phys.* **2010**, *73*, 036601.
70. Horn, R. G.; Smith, D. T. Analytic solution for the three-layer multiple beam interferometer. *Appl. Opt.* **1991**, *30*, 59-65.
71. Israelachvili, J. N. Thin Film Studies using Multiple-beam Interferometry. *J. Colloid Interface Sci.* **1973**, *44*, 259-272.
72. Heuberger, M. The Extended Surface Forces Apparatus. Part I. Fast Spectral Correlation Interferometry. *Rev. Sci. Instrum.* **2001**, *72*, 1700-1707.
73. Vinogradova, O. I.; Horn, R. G. Attractive Forces between Surfaces: What Can and Cannot Be Learned from a Jump-In Study with the Surface Forces Apparatus? *Langmuir* **2001**, *17*, 1604-1607.
74. Jalili, N.; Laxminarayana, K. A review of atomic force microscopy imaging systems: application to molecular metrology and biological sciences. *Mechatronics* **2004**, *14*, 907-945.
75. Lichtman, J. W.; Conchello, J.-A. Fluorescence microscopy. *Nat Meth* **2005**, *2*, 910-919.

76. Zhang, F.; Sautter, K.; Larsen, A. M.; Findley, D. A.; David, R. C.; Samha, H.; Linford, M. R. Chemical Vapor Deposition of Three Aminosilanes on Silicon Dioxide: Surface Characterization, Stability, Effects of Silane Concentration, and Cyanine Dye Adsorption. *Langmuir* **2010**, *26*, 14648-14654.
77. Li, H.; Zhang, J.; Zhou, X.; Lu, G.; Yin, Z.; Li, G.; Wu, T.; Boey, F.; Venkatraman, S. S.; Zhang, H. Aminosilane Micropatterns on Hydroxyl-Terminated Substrates: Fabrication and Applications. *Langmuir* **2010**, *26*, 5603-5609
78. Lyubchenko, Y.; Shlyakhtenko, L.; Harrington, R.; Oden, P.; Lindsay, S. Atomic force microscopy of long DNA: Imaging in air and under water. *Proc. Natl. Acad. Sci. U.S.A.* **1993**, *90*, 2137-2140.
79. Crampton, N.; Bonass, W. A.; Kirkham, J.; Thomson, N. H. Formation of Aminosilane-Functionalized Mica for Atomic Force Microscopy Imaging of DNA. *Langmuir* **2005**, *21*, 7884-7891.
80. Valtiner, M.; Banquy, X.; Kristiansen, K.; Greene, G. W.; Israelachvili, J. N. The Electrochemical Surface Forces Apparatus: The Effect of Surface Roughness, Electrostatic Surface Potentials, and Anodic Oxide Growth on Interaction Forces, and Friction between Dissimilar Surfaces in Aqueous Solutions. *Langmuir* **2012**, *28*, 13080–13093.
81. Bañuls, M.-J.; Puchades, R.; Maquieira, Á. Chemical surface modifications for the development of silicon-based label-free integrated optical (IO) biosensors: A review. *Anal. Chim. Acta* **2013**, *777*, 1-16.
82. Dorvel, B.; Jr., B. R.; Block, I.; Mathias, P.; Clare, S. E.; Cunningham, B.; Bergstrom, D. E.; Bashir, R. Vapor-Phase Deposition of Monofunctional Alkoxysilanes for Sub-Nanometer-Level Biointerfacing on Silicon Oxide Surfaces. *Adv. Funct. Mater.* **2010**, *20*, 87-95.
83. Ouyang, H.; Striemer, C. C.; Fauchet, P. M. Quantitative analysis of the sensitivity of porous silicon optical biosensors. *Appl. Phys. Lett.* **2006**, *88*, 163108-1-163108-3.
84. Engel, Y.; Elnathan, R.; Pevzner, A.; Davidi, G.; Flaxer, E.; Patolsky, F. Supersensitive Detection of Explosives by Silicon Nanowire Arrays. *Angew. Chem.* **2010**, *49*, 6830–6835.
85. Ingebrandt, S.; Offenhäusser, A. Label-free detection of DNA using field-effect transistors. *Phys. Stat. Sol.* **2006**, *203*, 3399–3411.

86. Howarter, J. A.; Youngblood, J. P. Optimization of Silica Silanization by 3-Aminopropyltriethoxysilane. *Langmuir* **2006**, *22*, 11142-11147.
87. Fiorilli, S.; Rivolo, P.; Descrovi, E.; Ricciardi, C.; Pasquardini, L.; Lunelli, L.; Vanzetti, L.; Pederzoli, C.; Onida, B.; Garrone, E. Vapor-phase self-assembled monolayers of aminosilane on plasma-activated silicon substrates. *J. Colloid Interface Sci.* **2008**, *321*, 235-241.
88. Kessel, C. R.; Granick, S. Formation and characterization of a highly ordered and well-anchored alkylsilane monolayer on mica by self-assembly. *Langmuir* **1991**, *7*, 532-538.
89. Zhu, M.; Lerum, M. Z.; Chen, W. How To Prepare Reproducible, Homogeneous, and Hydrolytically Stable Aminosilane-Derived Layers on Silica. *Langmuir* **2012**, *28*, 416-423.
90. Kanan, S. M.; Tze, W. T. Y.; Tripp, C. P. Method to Double the Surface Concentration and Control the Orientation of Adsorbed (3-Aminopropyl)dimethylethoxysilane on Silica Powders and Glass Slides. *Langmuir* **2002**, *18*, 6623-6627.
91. Basarir, F.; Yoon, T.-H. Preparation of γ -APS monolayer with complete coverage via contact printing. *J. Colloid Interface Sci.* **2009**, *336*, 393-397.
92. Fujita, M.; Mizutani, W.; Gad, M.; Shigekaw, H.; Tokumoto, H. Patterning DNA on mm scale on mica. *Ultramicroscopy* **2002**, *91*, 281-285.
93. Kumar, A.; Whitesides, G. M. Patterned Condensation Figures as Optical Diffraction Grating. *Science* **1994**, *263*, 60-62.
94. Gad, M.; Sugiyama, S.; Ohtani, T. Method for Patterning Stretched DNA Molecules on Mica Surfaces by Soft Lithography. *J. Biomol. Struct. Dyn.* **2003**, *21*, 387-393.
95. de la Rica, R.; Baldi, A.; Mendoza, E.; San Paulo, Á.; Llobera, A.; Fernández-Sánchez, C. Silane Nanopatterns via Gas-Phase Soft Lithography. *Small* **2008**, *4*, 1076-1079.
96. Pallandre, A.; Glinel, K.; Jonas, A. M.; Nysten, B. Binary Nanopatterned Surfaces Prepared from Silane Monolayers. *Nano Lett.* **2004**, *4*, 365-371.
97. Na, Y. J.; Park, S. J.; Lee, S. W.; Kim, J. S. Photolithographic Process for the Patterning of Quantum Dots. *Ultramicroscopy* **2008**, *108*, 1297-1301.

98. Jackman, R. J.; Duffy, D. C.; Cherniavskaya, O.; Whitesides, G. M. Using Elastomeric Membranes as Dry Resists and for Dry Lift-Off. *Langmuir* **1999**, *15*, 2973-2984.
99. Hale, P. S.; Kappen, P.; Prissanaroon, W.; Brack, N.; Pigram, P. J.; Liesegang, J. Minimizing silicone transfer during micro-contact printing. *Appl. Surf. Sci.* **2007**, *253*, 3746-3750.
100. Graham, D. J.; Price, D. D.; Ratner, B. D. Solution Assembled and Microcontact Printed Monolayers of Dodecanethiol on Gold: A Multivariate Exploration of Chemistry and Contamination. *Langmuir* **2002**, *18*, 1518-1527.
101. Clarkson, M. T. Multiple-Beam Interferometry with Thin Metal Films and Unsymmetrical Systems. *J. Phys. D* **1989**, *22*, 475-482.
102. Gupta, R.; Fréchet, J. Interferometry of surfaces with well-defined topography in the surface force apparatus. *J. Colloid Interface Sci.* **2013**, *412*, 82-88.
103. Shubin, V. E.; Kékicheff, P. Electrical Double Layer Structure Revisited via a Surface Force Apparatus: Mica Interfaces in Lithium Nitrate Solutions. *J. Colloid Interface Sci.* **1993**, *155*, 108-123.
104. Lee, J. N.; Park, C.; Whitesides, G. M. Solvent Compatibility of Poly(dimethylsiloxane)-Based Microfluidic Devices. *Anal. Chim. Acta* **2003**, *75*, 6544-6554.
105. Owen, M. J.; Smith, P. J. Plasma treatment of polydimethylsiloxane. *J. Adhes. Sci. Technol.* **1994**, *8*, 1063-1075.
106. Kim, J.; Chaudhury, M. K.; Owen, M. J. Hydrophobic Recovery of Polydimethylsiloxane Elastomer Exposed to Partial Electrical Discharge. *J. Colloid Interface Sci.* **2000**, *226*, 231-236.
107. Markov, D. A.; Lu, J. Q.; Samson, P. C.; Wikswo, J. P.; McCawley, L. J. Thick-tissue bioreactor as a platform for long-term organotypic culture and drug delivery. *Lab Chip* **2012**, *12*, 4560-4568.
108. George, A.; Blank, D. H. A.; ten Elshof, J. E. Nanopatterning from the Gas Phase: High Resolution Soft Lithographic Patterning of Organosilane Thin Films. *Langmuir* **2009**, *25*, 13298-13301.
109. Ditsent, V. E.; Skorokhodov, I. I.; Terent'eva, N. A.; Zolotareva, M. N.; Belyakova, Z. V.; Belikova, Z. V. Saturated vapor pressure of gamma aminopropyltriethoxysilane. *Zh. Fiz. Khim.* **1976**, *50*, 1905-1906.

110. Jasper, J. J. The Surface Tension of Pure Liquid Compounds. *J. Phys. Chem. Ref. Data* **1972**, *1*, 841-1010.
111. Perkin, S.; Kampf, N.; Klein, J. Stability of Self-Assembled Hydrophobic Surfactant Layers in Water. *J. Phys. Chem. B* **2005**, *109*, 3832-3837.
112. Grabbe, A. Double Layer Interactions between Silylated Silica Surfaces. *Langmuir* **1993**, *9*, 797-801.
113. Lin, Y.-C.; Yu, B.-Y.; Lin, W.-C.; Chen, Y.-Y.; Shyue, J.-J. Site-Selective Deposition of Gold on Photo-Patterned Self-Assembled Monolayers. *Chem. Mater.* **2008**, *20*, 6606–6610.
114. Kuo, C.-H.; Chang, H.-Y.; Liu, C.-P.; Lee, S.-H.; You, Y.-W.; Shyue, J.-J. Effect of Surface Chemical Composition on the Surface Potential and Iso-electric Point of Silicon Substrates Modified with Self-assembled Monolayers. *PCCP* **2011**, *13*, 3649-3653.
115. Shen, C.; Huang, Y.; Li, B.; Jin, Y. Predicting attachment efficiency of colloid deposition under unfavorable attachment conditions. *Water Resour. Res.* **2010**, *46*, W11526.
116. Duval, J. F. L.; Leermakers, F. A. M.; van Leeuwen, H. P. Electrostatic Interactions between Double Layers: Influence of Surface Roughness, Regulation, and Chemical Heterogeneities. *Langmuir* **2004**, *20*, 5052-5065.
117. Song, L.; Johnson, P. R.; Elimelech, M. Kinetics of Colloid Deposition onto Heterogeneously Charged Surfaces in Porous Media. *Environ. Sci. Technol.* **1994**, *28*, 1164- 1171.
118. Sun, N.; Walz, J. Y. A Model for Calculating Electrostatic Interactions between Colloidal Particles of Arbitrary Surface Topology. *J. Colloid Interface Sci.* **2001**, *234*, 90-105.
119. Bendersky, M.; Davis, J. M. DLVO interaction of colloidal particles with topographically and chemically heterogeneous surfaces. *J. Colloid Interface Sci.* **2011**, *353*, 87-97.
120. Duffadar, R. D.; Davis, J. M. Dynamic adhesion behavior of micrometer-scale particles flowing over patchy surfaces with nanoscale electrostatic heterogeneity. *J. Colloid Interface Sci.* **2008**, *326*, 18-27.
121. Duffadar, R.; Kalasin, S.; Davis, J. M.; Santore, M. M. The impact of nanoscale chemical features on micron-scale adhesion: Crossover from heterogeneity-dominated to mean-field behavior. *J. Colloid Interface Sci.* **2009**, *337*, 396-407.

122. Kemps, J. A. L.; Bhattacharjee, S. Interactions between a Solid Spherical Particle and a Chemically Heterogeneous Planar Substrate. *Langmuir* **2005**, *21*, 11710-11721.
123. Bhattacharjee, S.; Elimelech, M. Surface Element Integration: A Novel Technique for Evaluation of DLVO Interaction between a Particle and a Flat Plate. *J. Colloid Interface Sci.* **1997**, *193*, 273-285.
124. Shen, C.; Wu, L.; Zhang, S.; Ye, H.; Li, B.; Huang, Y. Heteroaggregation of microparticles with nanoparticles changes the chemical reversibility of the microparticles' attachment to planar surfaces. *J. Colloid Interface Sci.* **2014**, *421*, 103-113.
125. Pericet-Camara, R.; Papastavrou, G.; Behrens, S. H.; Borkovec, M. Interaction between Charged Surfaces on the Poisson–Boltzmann Level: The Constant Regulation Approximation. *J. Phys. Chem. B* **2004**, *108*, 19467-19475.
126. Behrens, S. H.; Borkovec, M. Electric double layer interaction of ionizable surfaces: Charge regulation for arbitrary potentials. *J. Chem. Phys.* **1999**, *111*, 382-385.
127. Lenz, P.; Lipowsky, R. Morphological Transitions of Wetting Layers on Structured Surfaces. *Phys. Rev. Lett.* **1998**, *80*, 1920-1923.
128. Benor, A.; Hoppe, A.; Wagner, V.; Knipp, D. Microcontact printing and selective surface dewetting for large area electronic applications. *Thin Solid Films* **2007**, *515*, 7679-7682.
129. Zhang, S.; Yan, L.; Altman, M.; Lässle, M.; Nugent, H.; Frankel, F.; Lauffenburger, D. A.; Whitesides, G. M.; Rich, A. Biological surface engineering: a simple system for cell pattern formation. *Biomaterials* **1999**, *20*, 1213-1220.
130. Ruiz, S. A.; Chen, C. S. Microcontact printing: A tool to pattern. *Soft Matter* **2007**, *3*, 1-11.
131. Jonas, U.; Campo, A. d.; Krüger, C.; Glasser, G.; Boos, D. Colloidal assemblies on patterned silane layers. *Proc. Natl. Acad. Sci. U.S.A.* **2002**, *99*, 5034–5039.
132. Fan, F.; Stebe, K. J. Assembly of Colloidal Particles by Evaporation on Surfaces with Patterned Hydrophobicity. *Langmuir* **2004**, *20*, 3062-3067.
133. Shipway, A. N.; Katz, E.; Willner, I. Nanoparticle arrays on surfaces for electronic, optical, and sensor applications. *ChemPhysChem* **2000**, *1*, 18-52.
134. Velev, O. D.; Kaler, E. W. In Situ Assembly of Colloidal Particles into Miniaturized Biosensors. *Langmuir* **1999**, *15*, 3693-3698.

135. Nazemifard, N.; Masliyah, J. H.; Bhattacharjee, S. Particle Deposition onto Charge Heterogeneous Surfaces: Convection–Diffusion–Migration Model. *Langmuir* **2006**, *22*, 9879-9893.
136. Butt, H.-J.; Cappella, B.; Kappl, M. Force measurements with the atomic force microscope: Technique, interpretation and applications. *Surf. Sci. Rep.* **2005**, *59*, 1-152.
137. Silbert, G.; Ben-Yaakov, D.; Dror, Y.; Perkin, S.; Kampf, N.; Klein, J. Long-Ranged Attraction between Disordered Heterogeneous Surfaces. *Phys. Rev. Lett.* **2012**, *109*, 168305.
138. Perkin, S.; Kampf, N.; Klein, J. Long-Range Attraction between Charge-Mosaic Surfaces across Water. *Phys. Rev. Lett.* **2006**, *96*, 038301.
139. Drelich, J.; Wang, Y. U. Charge heterogeneity of surfaces: Mapping and effects on surface forces. *Adv. Colloid Interface Sci.* **2011**, *165*, 91-101.
140. Drelich, J.; Yin, X. Mapping charge-mosaic surfaces in electrolyte solutions using surface charge microscopy. *Appl. Surf. Sci.* **2010**, *256*, 5381-5387.
141. Heinz, W. F.; Hoh, J. H. Relative Surface Charge Density Mapping with the Atomic Force Microscope. *Biophys. J.* **1999**, *76*, 528-538.
142. Taboada-Serrano, P.; Vithayaveroj, V.; Yiacoumi, S.; Tsouris, C. Surface Charge Heterogeneities Measured by Atomic Force Microscopy. *Environ. Sci. Technol.* **2005**, *39*, 6352-6360.
143. Kalasin, S.; Santore, M. M. Engineering Nanoscale Surface Features to Sustain Microparticle Rolling in Flow. *ACS Nano* **2015**, *9*, 4706-4716.
144. Harriott, L. R. Limits of lithography. *Proc. IEEE.* **2001**, *89*, 366-374.
145. Ito, T.; Okazaki, S. Pushing the limits of lithography. *Nature* **2000**, *406*, 1027-1031.
146. Gwyn, C. W.; Stulen, R.; Sweeney, D.; Attwood, D. Extreme ultraviolet lithography. *Journal of Vacuum Science & Technology B* **1998**, *16*, 3142-3149.
147. Groves, T. R.; Pickard, D.; Rafferty, B.; Crosland, N.; Adam, D.; Schubert, G. Maskless electron beam lithography: prospects, progress, and challenges. *Microelectron. Eng.* **2002**, *61–62*, 285-293.

148. Smith, E. A.; Chen, W. How To Prevent the Loss of Surface Functionality Derived from Aminosilanes. *Langmuir* **2008**, *24*, 12405-12409.
149. Wang, H.; Chen, S.; Li, L.; Jiang, S. Improved Method for the Preparation of Carboxylic Acid and Amine Terminated Self-Assembled Monolayers of Alkanethiolates. *Langmuir* **2005**, *21*, 2633-2636.
150. Koschwanez, J.; Carlson, R.; Meldrum, D. Thin PDMS Films Using Long Spin Times or Tert-Butyl Alcohol as a Solvent. *PLoS ONE* **2009**, *4*.

Appendix: Fabrication of elastomeric membranes

The following section provides a detailed explanation of how to fabricate the elastomeric membranes used in the chemical vapor deposition process of Chapter 4. The fabrication procedure is based on the work of Jackman et al⁹⁸ and includes additional steps to extract the PDMS oligomers from the membranes to yield contaminant-free patterned surfaces. Figure A.1 is an image of a fabricated elastomeric membrane containing 10 μ m diameter through holes.

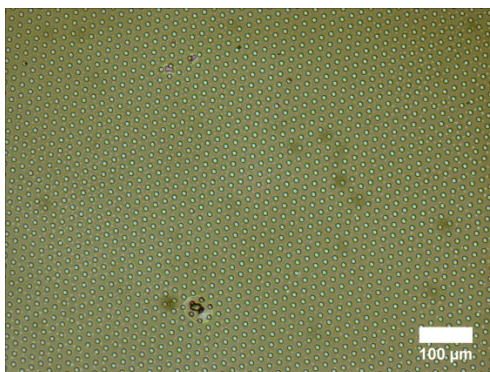


Figure A.1 Elastomeric membrane with 10 μ m through holes separated by 10 μ m

A.1 Overview of membrane fabrication

The fabrication of the elastomeric membranes has the following steps: 1) fabrication of micropillar template, 2) spin-coating of template with Sylgard 184, 3) Removal of membranes from the template, and 4) extraction and cleaning of membranes. Figure A.2 shows steps 1-3 of this process.



Figure A.2 Overview of membrane fabrication procedure A) Micropillar template for membrane fabrication. Pillars are fabricated from SU-8 on a silicon wafer. B) Template coated with Sylgard 184 via spin-coating to form membranes. Sylgard 184 layer thinner than SU-8 pillar height C) Cured Sylgard 184 peeled from template forming elastomeric membrane with through-holes.

The template for the membrane holes is fabricated by photolithography and consists of an array of SU-8 pillars on a silicon wafer. The actual membrane is fabricated on the template by spin-coating a layer of Sylgard® 184 on the template. The spin-coating speed and pillar height must be sufficient to allow this elastomer layer to be thinner than the actual pillars otherwise the membrane will not contain through holes. Once the Sylgard® 184 is thermally cured, the membrane can be peeled off of the template. This produces a free-standing membrane. The membranes are further extracted to remove any remaining oligomers that could be transferred when the membranes are used for surface patterning.

A.2 Template fabrication

Conventional photolithography is used to fabricate a template for the elastomer membranes. The templates are made by patterning the negative tone photoresist SU-8 (Microchem Corp., Newton, MA) on a silicon wafer. The key parameter that needs to be determined prior to fabrication is the height of the SU-8 structures as this will dictate the maximum membrane thickness that can be fabricated on a given template. Ensuring the

formation of through holes is accomplished by having sufficiently tall pillars on the template and using a high enough spin-speed. Spin-speed can be optimized after template fabrication if necessary. Taller pillars help ensure through-holes can be formed at lower spin-speeds and allow for thicker membranes. However, if the pillars are too tall, problems can occur during mold fabrication, particularly after the pillars are developed. With very tall pillars, capillary forces from drying the template after SU-8 development can cause pillars to delaminate of the pillars from the silicon wafer surface.

A.2.1 Wafer preparation

Obtaining a high-quality, reusable template for membrane fabrication starts with ensuring a clean silicon wafer surface. Fresh silicon wafers from the wafer supplier are first rinsed with acetone and isopropyl alcohol then dried with filtered air or nitrogen. Following this solvent rinse, a dehydration bake is performed at 200°C for 20-30 minutes. After the dehydration bake, an additional oxygen plasma cleaning can be performed immediately using a plasma etcher (Technics PEII-A Plasma System). The recommended plasma cleaning parameters are as follows: 0.3-0.4 Torr O₂, 100W, and 5 minutes. The wafer should be used immediately after cleaning.

A.2.2 SU-8 Spin-coating

Following wafer cleaning, the SU-8 photoresist is coated onto the substrate via spin-coating. The exact spin speed parameters depend on the desired final film thickness. The spin-speeds can be obtained from the SU-8 2000 series data sheets supplied by

Microchem, Corp. For a 22 μm thick film using SU-8 2025, the recommended spin procedure is summarized in the following table:

Table A-1 Recommended SU-8 2025 spin-coating parameters for a final film thickness of 22 μm

Step	Rate (RPM)	Time (s)	Acceleration (RPM/s)
1	500	10	100
2	4000	30	300

A.2.3 Soft Bake

Following spin-coating, a soft bake step is performed to drive off excess solvent from the SU-8 film and prevent the photoresist from sticking to the photomask. For a 22 μm thick film, a soft bake time of 4min and 40s at 95°C is recommended.

A.2.4 Exposure

After soft baking is completed, the SU-8 film is exposed. Because SU-8 is a negative photoresist, the film that is exposed will remain following development while the unexposed film will dissolve away. Good patterning requires a sufficient exposure energy and conformal contact between the photomask and SU-8 film. The recommended exposure energy for a 22 μm thick SU-8 film on a silicon surface is 150 mJ/cm^2 .

A.2.5 Post-exposure Bake

Following exposure, a post-exposure bake (PEB) is used to ensure complete cross-linking of the exposed SU-8. For a 22 μ m thick film, the recommended baking parameters are 1 min at 65°C followed by 4min 40s at 95°C. If the correct exposure energy was used, the exposed patterns should become visible within 1 minute of the wafer being placed on the 95°C hotplate.

A.2.6 Development

The final step in generating the SU-8 structures is a development step in which the unexposed SU-8 is removed from the wafer leaving only the exposed SU-8. The wafer is developed by immersing it in a bath of SU-8 developer for about 5 minutes (For a 22 μ m micropillar array). To help facilitate development, the bath can be gently agitated by hand. Following immersion, the entire wafer is rinsed once with fresh developer and then isopropyl alcohol and dried with filtered air or nitrogen. If a white residue is formed after rinsing the wafer with isopropyl alcohol, the wafer needs to be developed longer. Development time is highly dependent on the SU-8 film thickness and the pitch of the features. Thicker films and structures closer together will generally require longer development times.

A.2.7 Hard bake

A final, optional, step following development is a hard bake at elevated temperatures. This hard baking step can help anneal surface cracks in the SU-8 layer and ensure stable properties of the structures in future thermal cycling steps during membrane curing. A 10 min hard bake at 200°C was used for the templates in this work.

A.2.8 Mold Characterization

The key parameter to check following mold fabrication is the height of the fabricated SU-8 pillars. A 3D laser scanning microscope (Keyence VK-X100) can be used to image the pillar structures and determine their height. Figure A.3 shows an example of a mold characterized using a 3D laser scanning microscope.

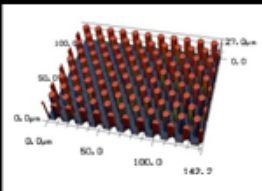
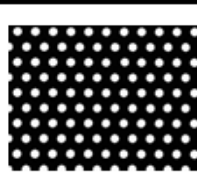
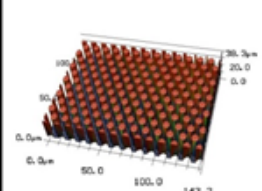
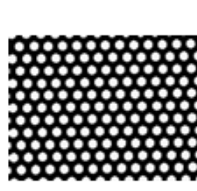
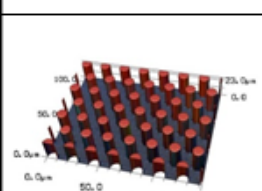
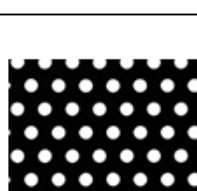
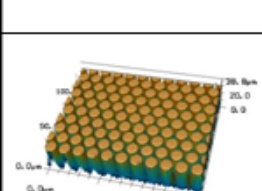
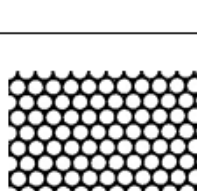
	3D Profile	Binary Image	Height	Pillar surface coverage
6.5 x 6.5			22.4±0.1μm	21.8%
6.5 x 4			22.4±0.1μm	37.2%
10 x 10			22.0±0.0μm	22.3%
10 x 3			23.4±0.6μm	60.2%

Figure A.3 Example micropillar arrays characterized by laser scanning microscope showing a 3D profile, binary image of the pillar dimensions, average pillar height, and pillar surface coverage.

The pillar dimensions used in figure A.3 are given as the pillar diameter (d) by the pillar to pillar edge spacing (s) in microns. For example 6.5 x 4 corresponds to 6.5 μm diameter pillars separated by 4 μm. The estimated fractional coverage of the pillars arranged in a hexagonal array can be calculated by the following equation:

$$f_p = \frac{\pi}{2\sqrt{3}} \left(\frac{d}{l}\right)^2 \quad (\text{A.1})$$

A.2.9 Mold release agent

After the template is fabricated, it can be coated with a mold release agent to facilitate easier removal of the cured elastomeric membranes. This is accomplished by performing a chemical vapor deposition of the fluorosilane trichloro(1H,1H,2H,2H-perfluorooctyl)silane (Sigma-Aldrich, St. Louis, MO) on the fabricated template. For the templates used in this work, 20 μL of fluorosilane was used per silicon wafer in a vacuum desiccator (Scienceware® vacuum desiccator). After adding the fluorosilane species, the desiccator was pumped down for 1 min under vacuum and sealed to allow the silanization to occur for 2 hours. Following silanization, the surfaces were rinsed with isopropyl alcohol and annealed in an oven at 100°C for 1 hour and then rinsed one more time with isopropyl alcohol and dried with filtered nitrogen.

A.3 Elastomeric membrane fabrication

A.3.1 Spin-coating PDMS elastomer

The elastomeric membranes are fabricated by spin-coating Dow Corning Sylgard® 184 (Purchased from Robert McKeown Inc., Branchburg, NJ) onto the membrane template. The primary concern with membrane fabrication is ensuring that the membranes have through-holes. If insufficient spin-coating parameters (low RPM or short time), the membrane can form with a film over the holes (Figure 8.4)

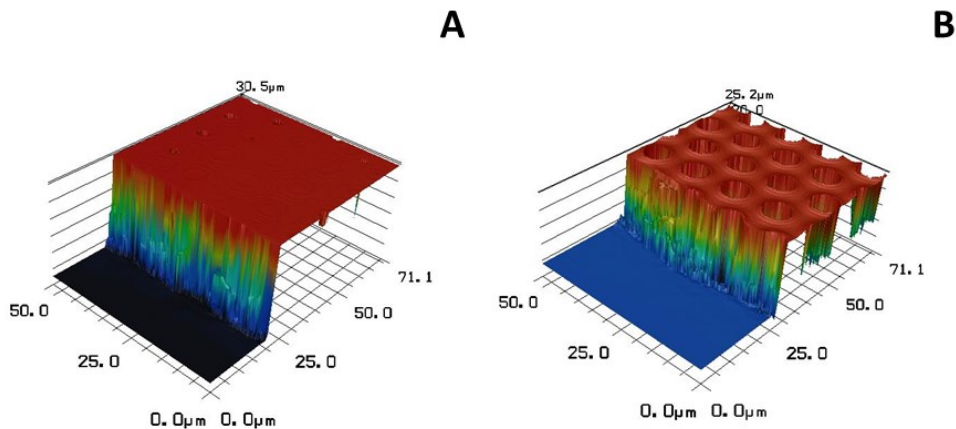


Figure A.4 Laser microscope 3D profile images of the top-side of cured elastomeric membranes ($6.5 \times 6.5 \mu\text{m}$) removed from mold A) Insufficient spin-coating parameters lead to film over holes. B) Sufficient spin-coating parameters showing though holes in membrane.

The elastomeric membranes are fabricated by mixing Sylgard 184 in a 10:1 ratio of base to curing agent. After thoroughly mixing the base with the curing agent, the mixture is degassed under vacuum for ~ 20 min to remove entrained air bubbles. Then, ~ 4 mL of mixed elastomer is poured onto the template and spin-coated. The required spin speed is highly dependent on the height of the micropillars on the template and their spacing. In general, the shorter the pillars and the closer they are together, the higher the rotation rate needed for spin-coating. For membranes with dimensions $6.5 \times 6.5 \mu\text{m}$, with a micropillars $22 \mu\text{m}$ tall, the spin parameters cited in Table 8-2 were found sufficient.

Table A-2 Spin-coating parameters for a final elastomer film thickness of 20 μm with a membrane template dimensions 6.5x6.5 μm and micropillar height 22 μm

Step	Rate (RPM)	Time (s)	Acceleration (RPM/s)
1	200	10	100
2	8000	80	100
3	8000	300	100

The 300s (5min) spin-coating time in step 3 of Table 8-2 was adapted from literature for fabricating uniform thin films of PDMS elastomer.¹⁵⁰ After spin-coating, a ring of uncured PDMS elastomer can be carefully painted around the periphery of the micropillar arrays. This ring creates a support structure that helps with handling after the membranes are cured and removed from the template.

A.3.1 Curing membranes

Following spin-coating, the membranes are cured in an oven at a temperature of 70°C for 48 hours. This extended curing allows for full cross-linking of the PDMS elastomer to help prevent transfer of oligomers when the membranes are used for surface patterning.⁹⁹ When curing is completed, the membranes can be removed from the template by cutting around their edges and carefully peeling them off with tweezers. The template can be cleaned for reuse once the membranes are removed by pouring a large amount of PDMS on it and curing. This cured PDMS can be peeled off the template and any residue from the membrane fabrication will be removed leaving a behind a clean, reusable template.

A.3.2 Membranes extraction

Even with the extended curing of the last step, the membranes will still contain some unreacted PDMS oligomers that can be transferred to surfaces they are used for patterning. A solvent extraction step in hexanes is used to remove these unreacted oligomers.¹⁰⁰ The membranes are extracted by immersing them in a dish of hexanes for 48 hours. The hexane can be stirred with a magnetic stirrer to help improve the extraction efficiency. Additionally, the hexanes should be replaced at least 3 times during the process to remove extracted oligomers dissolved in the hexanes. When extraction is completed, the membranes are removed from the hexane and placed on a surface for drying. Fresh-cleaved mica is an ideal substrate for drying the membranes but cleaned glass slides can be used as well. The hexane-swelled membranes are dried overnight at 70°C in a vacuum oven. After drying to remove the hexane, the membranes are cleaned by sonicating them in isopropyl alcohol 3 times for 5 minutes. Then, they are placed on a fresh substrate for another drying step to remove the isopropyl alcohol. The membranes are once again dried overnight 70°C in a vacuum oven. Following this drying step, the membranes can be stored until ready for use.

Curriculum Vitæ

Christian Pick was born April 17th 1986 in North Kansas City, Missouri and grew up in Liberty, Missouri. He received his bachelors of science in chemical engineering in 2008 from the Missouri University of Science and Technology. While at Missouri S&T, Christian conducted research in the Intelligent Microsystem Laboratory (IML) on evanescent waveguide sensors and hydrogel composites for optical glucose and hydrogen peroxide sensing. After graduating from Missouri S&T, Christian became a graduate research assistant in the Department of Chemical and Biomolecular Engineering at the Johns Hopkins University under the guidance of Dr. Joelle Frechette and Dr. German Drazer. He was also an IGERT fellow in the Institute for Nanobiotechnology (INBT). His research at Johns Hopkins focused on studying the effects of charge heterogeneities on electrical double layer interactions. His research interests include surface force measurement, chemical surface patterning, and thin films.